UNIVERSIDADE FEDERAL DO CEARÁ
CENTRO DE CIÊNCIAS
DEPARTAMENTO DE FÍSICA
PROGRAMA DE PÓS-GRADUAÇÃO EM FÍSICA

VICTOR NOCRATO MOURA

INTERPLAY BETWEEN CHARGE DENSITY WAVE AND SUPERCONDUCTING PHASES IN TRANSITION METAL DICHALCOGENIDES AND INTERFACES

FORTALEZA
2023

VICTOR NOCRATO MOURA

INTERPLAY BETWEEN CHARGE DENSITY WAVE AND SUPERCONDUCTING PHASES IN TRANSITION METAL DICHALCOGENIDES AND INTERFACES

Tese de Doutorado apresentada ao Programa de Pós-Graduação em Física da Universidade Federal do Ceará, como requisito parcial para a obtenção do Título de Doutor em Física. Área de Concentração: Física da Matéria Condensada.

Orientador: Prof. Dr. Andrey Chaves.

Coorientador: Prof. Dr. Milorad V. Milosevic.

FORTALEZA
2023

Dados Internacionais de Catalogação na Publicação
Universidade Federal do Ceará
Sistema de Bibliotecas
Gerada automaticamente pelo módulo Catalog, mediante os dados fornecidos pelo(a) autor(a)

M889i Moura, Victor Nocrato.
Interplay between charge density wave and superconducting phases in transition metal dichalcogenides and interfaces / Victor Nocrato Moura. – 2023.
88 f. : il. color.

Tese (doutorado) – Universidade Federal do Ceará, Centro de Ciências, Programa de Pós-Graduação em Física , Fortaleza, 2023.
Orientação: Prof. Dr. Andrey Chaves.
Coorientação: Prof. Dr. Milorad V. Milosevic.

1. Supercondutividade. 2. Teoria de Ginzburg-Landau. 3. Competição. 4. Ondas de densidade de cargas. 5. Materia Condensada. I. Título.

CDD 530

VICTOR NOCRATO MOURA

INTERPLAY BETWEEN CHARGE DENSITY WAVE AND SUPERCONDUCTING PHASES IN TRANSITION METAL DICHALCOGENIDES AND INTERFACES

Tese de Doutorado apresentada ao Programa de Pós-Graduação em Física da Universidade Federal do Ceará, como requisito parcial para a obtenção do Título de Doutor em Física. Área de Concentração: Física da Matéria Condensada.

Aprovada em 27/02/2023.

BANCA EXAMINADORA

Prof. Dr. Andrey Chaves (Orientador)
Universidade Federal do Ceará (UFC)

Prof. Dr. Diego Rabelo da Costa
Universidade Federal do Ceará (UFC)

Prof. Dr. João Milton Pereira Jr.
Universidade Federal do Ceará (UFC)

Prof. Dr. Aristeu Rosendo Pontes Lima
Universidade da Integração Internacional da Lusofonia Afro-Brasileira (UNILAB)

Prof. François M. Peeters
University of Antwerp, Belgium (UA)

Aos Meus Pais, Amigos e Esposa

AGRADECIMENTOS

Obrigado ao Prof. Dr. Andrey Chaves pela orientação durante essa longa jornada de conhecimento. Obrigado a todos do GTMC, que me deram suporte. Obrigado Aline por estar sempre ao meu lado!!

O presente trabalho foi realizado com apoio da Coordenação de Aperfeiçoamento de Pessoal de Nível Superior - Brasil (CAPES) - Código de Financiamento 001.

ABSTRACT

The competition between two different collective states and their interplay are standing questions in solid-state physics. The discovery of high-temperature superconductivity in materials brought a new spectrum of compounds that exhibit competition between superconductivity and another collective state, such as density waves (charge/spin density waves). In recent studies, transition-metal dichalcogenides (TMDs) show emergent superconductivity when doped. It was suggested the fluctuations of their charge density wave (CDW) order, in the form of discommensurations, are closely related to enhancing the superconductor's critical temperature. With a novel technique based on scanning tunneling microscopy, it became possible to measure distinct amplitude and phase images of CDW with high spatial resolution. Such analysis in TMDs provides evidence that their charge density wave consists of three individual charge modulations. Phase images revealed topological defects and discommensurations in a nearly-commensurate state that was predicted by the McMillan theory. Recently, a Ginzburg-Landau-McMillan model was used to describe the CDW in TMDs, specifically in $TiSe_2$. In this thesis, first, we theoretically examine the behavior of superconductivity at parallel interfaces with other dominant collective excitation, such as charge density waves or spin density waves. Due to their competitive coupling in a two-component Ginzburg-Landau model, suppression of the prevailing order parameter at the interfacial planes allows for nucleation of the (hidden) superconducting order parameter at those planes. Then, we investigate the role of the different parameters within the Ginzburg-Landau-McMillan theory on the phase distribution, discommensurations, and critical temperatures of CDW in 2D materials and how these parameters influence the superconductivity. We employ an imaginary time evolution method on the Ginzburg-Landau-McMillan equations to obtain first the CDW discommensuration distributions and then the superconductivity.

Keywords: superconductivity; charge density waves; Ginzburg-Landau theory; competition; condensed matter.

RESUMO

A competição entre dois estados coletivos diferentes e sua interação são questões recorrentes na física do estado sólido. A descoberta da supercondutividade em materiais de alta temperatura trouxe um novo espectro de compostos que apresentam competição entre a supercondutividade e outro estado coletivo, como ondas de densidade (de carga ou spin). Em estudos recentes, em dichalcogenetos de metais de transição (TMDs) apresentam um estado supercondutor emergente quando dopados. Foi sugerido que as flutuações de sua ordem de onda de densidade de carga (CDW), na forma de descomensurações, estão relacionadas ao aumento da temperatura crítica do supercondutor. Utilizando uma nova técnica de microscopia de varredura por tunelamento, experimentos recentes conseguiram obter imagens distintas de amplitude e fases de CDW com alta resolução espacial, e esta análise em TMDs fornece evidências de que sua onda de densidade de carga consiste de três modulações de carga individuais. As imagens de fases revelaram defeitos topológicos e descomensurações em um estado quase-comensurável que foi previsto pela teoria de McMillan. Recentemente, um modelo Ginzburg-Landau-McMillan foi usado para descrever a CDW em TMDs, especificamente em $TiSe_2$. Nesta tese, primeiramente, examinamos teoricamente o comportamento da supercondutividade em interfaces paralelas que separam os domínios de outra excitação coletiva dominante, como ondas de densidade de carga ou ondas de densidade de spin. Devido ao seu acoplamento competitivo em um modelo Ginzburg-Landau de duas componentes, a supressão do parâmetro de ordem dominante nas planos interfaciais permite a nucleação do parâmetro de ordem supercondutor (oculto) nesses planos. Em seguida, investigamos o papel dos diferentes parâmetros dentro da teoria Ginzburg-Landau-McMillan na distribuição de fases, descomensurações e temperaturas críticas da CDW em materiais 2D e como esses parâmetros influenciam a supercondutividade. Empregamos um método de evolução no tempo imaginário nas equações Ginzburg-Landau-McMillan para obter primeiro as distribuições de descomensurações da CDW e depois da supercondutividade.

Palavras-chave: supercondutividade; ondas de densidade de cargas; teoria de Ginzburg-Landau; competição; matéria condensada.

LISTA DE FIGURAS

LISTA DE SIGLAS

ABNT	Associação Brasileira de Normas Técnicas
CNPq	Conselho Nacional de Desenvolvimento Científico e Tecnológico
CDW	Charge density wave
OP	Order Parameter
SC	Superconductor
BCS	Bardeen-Cooper-Schrieffer
TMD	Transition metal dichalcogenides
MGL	McMillan-Ginzburg-Landau

CONTENTS

1 INTRODUCTION

The Ginzburg-Landau (GL) theory for superconductors is one of the most influential and powerful theories of the mid-20th century. Since the discovery of superconductivity at the beginning of the 20th century[1–4], multiple theories tried to fully explain the phenomenon and culminating in the phenomenological theory of Ginzburg-Landau [5] that uses previous works of Landau and London [1, 6] to describe one of the most interesting and complex problems in physics.

The discovery in 1911 by Heike K. Onnes in Leiden, Netherlands[7], was the start of the study of superconductivity. By cooling a sample of mercury below 4.2 K, he found the perfect conductivity which is one of the main characteristics of the superconductor. Multiple milestones in the research of superconductivity have been achieved since its discovery. In 1933, the second main characteristic was discovered by W. Meissner and R. Ochsenfeld[8], which the superconductor has perfect diamagnetism and expels external magnetic fields. To create a theory to explain the superconductor one needed to contemplate those two features, and the first theory to achieve such an explanation was done by F. and H. London[1], using a modified Maxwell equation to define the behavior of the "superconductors electrons". In the 1950s comes a big revolution in superconductivity. The decade begins with the publication of the Ginzburg-Landau theory by V. L. Ginzburg[5]. In 1957, two great works divided the attention, first the vortex theory of Abrikosov[9], and then the Bardeen-Cooper-Schrieffer (BCS) microscopic theory[10]. Both works revolutionized the understanding of the nature of the superconductor. The link between the two big theories of Ginzburg and BCS was done by Gor'kov in 1959[11]. More recently, in 1986, the discovery of high-temperature superconductivity[12] opened a huge number of possibilities to superconductors. A new wave of theories and experiments started from this discovery. Another door opened in 2004 with the discovery of two-dimensional graphene which increased interest in two-dimensional materials. The combination of all these milestones allowed us to make this thesis.

The GL theory allowed science to advance in solving complex superconductor problems that could describe superconductivity with inhomogeneous parameters, magnetic fields, or both. The success of the theory pushed the scientific community to expand the equations for new systems that had similarities with superconductivity. Multi-component GL theory is used

to describe superconductors with multiple gaps[13–19], high-temperature superconductors can be described with the GL theory[20, 21], and spin/charge density waves have a phenomenological theory derived from the GL theory of superconductivity[21–26]. In recent years, the study of novel materials with reduced dimensionality, so-called two-dimensional materials, brought new challenges to solid-state physics[27–36].

Transition metal dichalcogenides (TMDs) are a versatile chemical family of layered materials that can be exfoliated to a monolayer. The evidence of the presence of competing collective states, such as charge density waves and superconductivity, has stimulated new studies involving these materials.[37–42]

The focus of this thesis is to understand the interplay between the charge density wave (CDW) and superconductivity (SC) in TMDs. We start by expanding a generic multicomponent GL theory, in which multiple interfaces are present. In the interfaces, the dominant collective state (the CDW) is suppressed and a hidden SC state rises. In such a case, we demonstrate how the number of the parallel interfacial planes and the distance between them is linked to the number and the size of the emerging superconducting gaps in the system, as well as the versatility and temperature evolution of the possible superconducting phases. These findings bear relevance to a broad selection of known layered superconducting materials, as well as to further design of artificial (e.g. oxide) superlattices, where the interplay between competing order parameters paves the way toward otherwise unattainable superconducting states, some with enhanced superconducting critical temperature.

After developing such a general model, we discuss in more detail the interplay between the collective phases in TMDs. In these materials, the CDW is formed by three order parameters representing three charge density distributions. We use an expansion of the GL theory developed by McMillan[23] to describe the CDW in TMD fully. We then developed an efficient imaginary time evolution method for solving the MGL equations resulting from this approach, which allowed us to investigate, in a phenomenological way, the role of different coupling parameters on the CDW patterns and to perform calculations with different energy functionals that lead to several experimentally observed singularities in the CDW phase profiles.[43] In particular, by choosing the appropriate energy functionals, we were able to use this phenomenological model to obtain phases that go beyond the well-known periodic phase slips (discommensurations), exhibiting also topological defects (namely, vortex-antivortex pairs), domain walls where the CDW order parameter is suppressed, and even CDW with broken rotational symmetry. The

effect of these different phases on the profile and critical temperature of the competing emergent superconducting state is also discussed.

The thesis is organized as follows. In chapter 2 we describe the GL theory in detail. Chapter 3 is dedicated to giving a brief introduction to the charge density wave theory, while Chapter 4 expands the theory to the transition metal dichalcogenides. Chapter 5 provides the theory and results from our investigation on the multi-component GL theory for interface superconductivity. Chapter 6 is focused on the interplay between SC and CDW in TMDs. We finish with our conclusions in Chapter 7.

2 SUPERCONDUCTIVITY: GINZBURG-LANDAU THEORY

The discovery of superconductivity in 1911 by Heike K. Onnes [7] in Leiden, Netherlands, brought to the scientific world a new type of phenomenon to investigate. After 110 years of experiments and discoveries, the field keeps providing questions, especially in the pursuit of a room-temperature SC. Novel materials with unusual physical properties have given rise to new and intriguing SC phases when combined with other collective states.

In this chapter, we will review the basic concepts of SC, such as the Meissner-Ochsenfeld effect, critical field, and condensation energy. We will introduce the Ginzburg-Landau (GL) theory[5] and the notations we shall use in this thesis. We will not follow a historical line, but instead, we will step-by-step introduce the concepts and equations necessary to understand the GL theory.

Magnetic field-induced Abrikosov vortices are not among the topics discussed in the results produced by this Thesis. However, since we will discuss vortex-antivortex pairs in CDW later in this work, it is worth providing a brief introduction to vortex states in superconductors, which is done in what follows. For more details on the Abrikosov vortex lattice, see the Appendix.

2.1 Condensation energy of a superconductor

Onnes discovered superconductivity by reducing the temperature of a mercury sample to temperatures below 4.2 K. At this temperature, the electric resistance fell abruptly close to zero (see Fig. 1). He defined the SC as a state where the material has perfect conductivity. Another characteristic of the SC state is the perfect diamagnetism discovered in 1933 by W. Meissner and R. Ochsenfeld[8]. The perfect conductivity explains that a magnetic field can not enter a massive superconductor, but in the Meissner-Ochsenfeld effect, the magnetic field is expelled from a material when it is cooled below its critical temperature, which means that the material does not retain magnetic history. This behavior is sketched in Fig. 2.

The Meissner-Ochesenfeld effect is important for a thermodynamic approach to the study of superconductors. It proves that SC is a reversible and stable state, allowing the study of superconductors by a phase transition theory much like the transition between liquid and gas[44, 45]. Although the GL theory of superconductivity, developed in 1950, was introduced

Figure 1 – First discovery of superconductivity

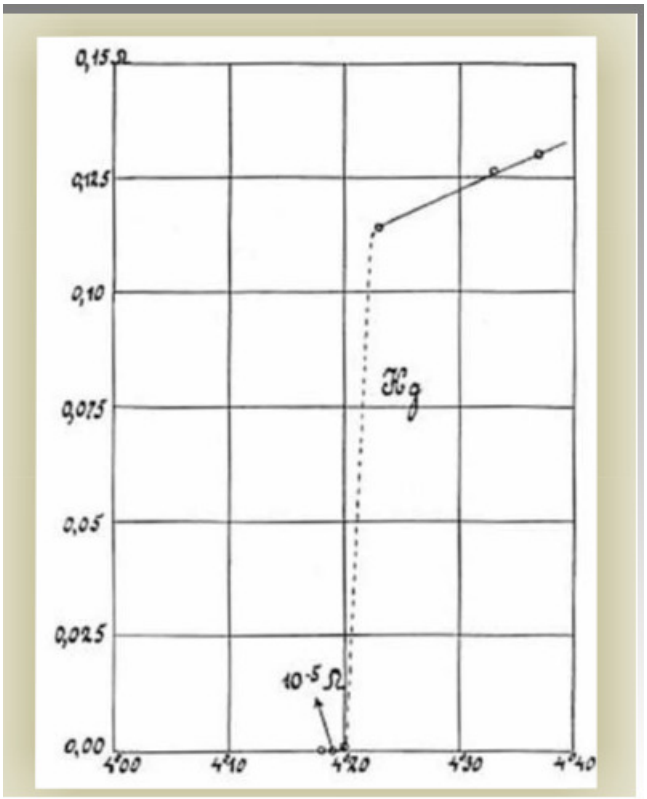

Source: Figure extracted from [7]. Figure extracted from K. Onnes notebook. It shows the drop in resistivity of a mercury sample for temperatures below 4.2 K.

as a phenomenological theory, in 1959, Gor'kov[11] showed that it can be derived from the microscopic theory and, in this way, the GL theory describes the SC phase transition from the thermodynamic point of view.

As the superconductivity state is a thermodynamic state, there are variables that can be used to characterize it, like pressure and temperature, as used for solid, liquid, and gas phases. From the first experimental observations of SC, it is clear that one of the variables is the temperature: there is a critical temperature T_c below which the material goes from the normal state to the superconductivity state. The reversibility of the expulsion of the magnetic field also implies that there is a transition from normal to superconductor state by the magnetic field when a critical magnetic field is applied $H = H_c$[44]. It is important to say that only type-I superconductors, the firsts to be discovered, faithfully obey this distinction between normal and superconducting state - for a type-II superconductor, there is a mixed state where part of the magnetic field penetrates in the superconductor. The set (T, H) then gives us variables that can be used in a thermodynamic framework.

For the superconductor state to be stable its free energy must be lower than the normal state for a set of $(T < T_c, H < H_c)$. We can now use all the tools from thermodynamics

Figure 2 – Skech of the Meissner-Ochsenfeld effect

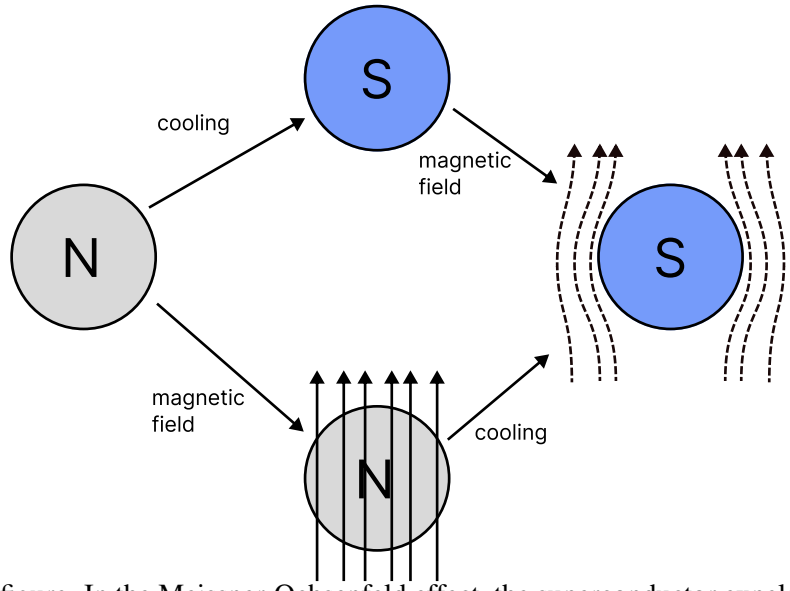

Source: Author's figure. In the Meissner-Ochsenfeld effect, the superconductor expels the magnetic field when it is cooled from the normal state (N) down below the critical temperature, where it becomes superconductor (S), even if the magnetic field is already in place before the cooling.

and apply them to the transition between normal and superconductor states. Starting with the internal energy U,

$$dU = TdS + \mu_0 V \mathbf{H} \cdot d\mathbf{M}, \tag{2.1}$$

where U is the total internal energy, T is the temperature and S the entropy. We can define the Helmholtz, $F(T,\mathbf{M})$, and Gibbs, $G(T,\mathbf{H})$, free energies

$$F(T,\mathbf{M}) = U - TS, \tag{2.2}$$

$$G(T,\mathbf{H}) = F(T,\mathbf{M}) - \mu_0 \mathbf{H} \cdot \mathbf{M}. \tag{2.3}$$

Since the superconductor is a stable state, the Gibbs free energy when we go from $H = 0$ to $H = H_c$, where $H_c(T)$ is the critical field that destroys the superconductor state, has to be lower than the normal state. We can evaluate such change by integrating the Gibbs free energy

$$G_s(T,H_c) - G_s(T,0) = -\mu_0 V \int_0^{H_c} \mathbf{M} \cdot d\mathbf{H}, \tag{2.4}$$

where the subscript s implies that we are referring to the superconducting state. The Meissner-Ochsenfeld effect gives us $\mathbf{M} = -\mathbf{H}$ and thus

$$G_s(T,H_c) - G_s(T,0) = \mu_0 \frac{Hc^2}{2}. \tag{2.5}$$

In the normal state, $\mathbf{M} \approx 0$, apart from the small normal metal para-magnetism or diamagnetism,

so

$$G_n(T,H_c) - G_n(T,0) = 0. \tag{2.6}$$

At the critical field H_c, the normal and superconducting phases are in thermodynamic equilibrium, this implies that the two Gibbs energies are equal,

$$G_s(T,H_c) = G_n(T,H_c). \tag{2.7}$$

Putting together the difference in Gibbs free energies of superconducting and normal states,

$$G_s(T,0) - G_n(T,0) = -\mu_0 \frac{H_c^2}{2} \tag{2.8}$$

or

$$F_s(T,0) - F_n(T,0) = -\mu_0 \frac{H_c^2}{2} \tag{2.9}$$

The difference in the Gibbs energy $\mu_0 \frac{H_c^2}{2}$ is the condensation energy. It is negative, implying the superconducting state is stable, and defines the thermodynamic critical field $H_c(T)$ as a function of the difference of the free energy between the normal and the superconducting phases. It was found empirically that $H_c(T)$[45] is well approximated by a parabolic law

$$H_c(T) \approx H_c(0)[1 - (T/T_c)^2]. \tag{2.10}$$

We can sketch the phase diagram $H \times T$ for type-I superconductors, Fig. 3, where the line is transition Normal/Superconductor.

The experiment of H. K. Onnes showed that the transition in zero fields at T_c is second order, while the transition of the magnetic field is first order, as can be verified by the finite change in entropy between normal and superconductor state and has a finite latent heat,

$$S_\mathrm{s}(T,H_\mathrm{c}) - S_\mathrm{n}(T,H_\mathrm{c}) = -\mu_0 H_\mathrm{c} \frac{\mathrm{d}H_\mathrm{c}}{\mathrm{d}T}. \tag{2.11}$$

The Ginzburg-Landau theory of superconductivity[5] uses the fact that we have a second-order phase transition in the temperature to expand the theory of second-order phase transition developed by L. D. Landau in the 1930s[46].

The value of the theory is in treating the macroscopic behavior of superconductors in nonuniform situations, giving quite reliable predictions of the critical fields and spatial structure of the superconductivity. For the following sections, we use as references the works of [5, 44, 45].

Figure 3 – Sketch of the phase diagram for type-I superconductors

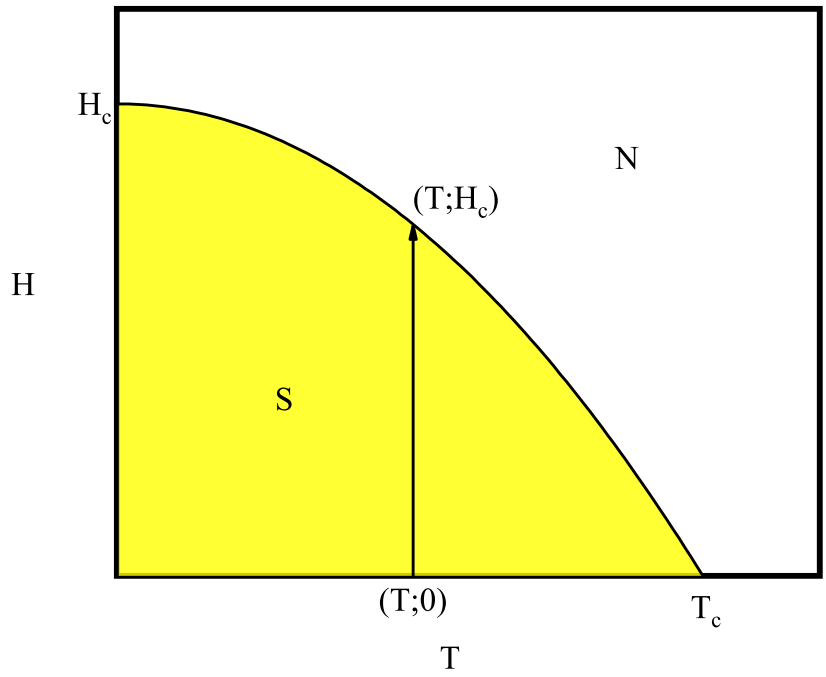

Source: Figure adapted from [45].Sketch of a phase diagram of a transition from Normal (N) to the superconductor (S) state. H_c is the critical field and T_c is the critical temperature. The condensation energy for type-I superconductors is obtained by integration of the Gibbs free energy along the arrow.

2.2 Bulk Superconductors

We start with bulk superconductors. The second-order phase transitions involve a change in the symmetry of the system, below a certain temperature, T_c the superconductivity appears spontaneously. In Landau's theory, the phase transition is characterized by an order parameter (OP). Ginzburg postulated the existence of a complex OP ψ that characterizes the superconductivity. At first, it was not specified of what physical quantity this ψ would represent. Later, Gor'kov proved the relationship between the OP and the density of Cooper pairs in the Bardeen-Cooper-Schrieffer (BCS) theory[10] and their relation with the opening of a gap Δ in the Fermi energy of the system.

The basic postulate of GL is that if ψ varies slowly in space, the free energy density F_s can be expanded in a series of the form,

$$f_s = f_n + a_s|\psi|^2 + \frac{b_s}{2}|\psi|^4 + \frac{1}{2m^*}\left|\left(\frac{\hbar}{i}\nabla - \frac{e^*}{c}\mathbf{A}\right)\psi\right|^2 + \frac{h^2}{8\pi}, \tag{2.12}$$

where a_s and b_s are phenomenological coefficients, $\mathbf{A}$ is vector potential that is related to the applied magnetic field h. The terms $m^* = 2m_e$ and $e^* = 2e$ are the mass and charge of the

Cooper pair, respectively.

In the absence of fields and gradients, we have

$$f_s - f_n = a_s|\psi|^2 + \frac{b_s}{2}|\psi|^4, \tag{2.13}$$

which can be viewed as a series expansion in powers of $|\psi|^2$ with only the first two terms. The phenomenological parameters are temperature dependent and are assumed to be smooth functions of the temperature. For the energy in Eq. (2.13) to have a minimum, the coefficient b_s must be positive. Two cases arise, depending on whether a_s is positive or negative. As is

Figure 4 – Superconductor free energy

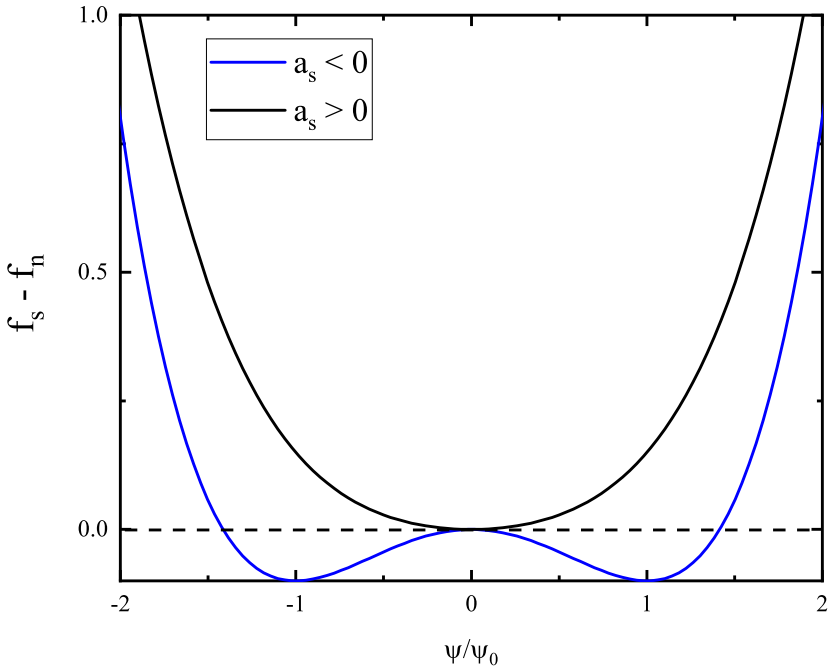

Source: Figure adapted from [45]. Difference between the free energy of the superconducting state and the normal state per unit volume as a function of the order parameter. For $T < T_c$ the free energy has minimums in ψ_0, whereas for $T > T_c$ the minimum union is in $\psi = 0$

illustrated in Fig. 4, if $a_s > 0$ the curve has one minimum at $\psi = 0$. On the other hand, if $a_s < 0$ there are minima whenever

$$|\psi|^2 = |\psi_0|^2 = -a_s/b_s. \tag{2.14}$$

The notation ψ_0 is used to represent a value infinitely deep in the interior of the superconductor. Using this value and Eq. (2.9), we find

$$-\frac{a_s^2}{2b_s} = -\mu_0 \frac{H_c^2}{2},$$

$$H_c^2 = \frac{a_s^2}{\mu_0 b_s}, \tag{2.15}$$

the definition of the thermodynamic critical field H_c.

The phenomenological parameters a_s and b_s must be temperature dependent for the ψ behave like Fig. 4

$$a_s \to a_s(T)$$

$$b_s \to b_s(T)$$

and $a_s(T)$ must change from positive to negative at the temperature T_c, where T_c is the critical temperature of the superconductor, the point of phase transition between the normal and the superconductor state. At temperatures below T_c, the free energy (2.12) has a lower value when the OP $|\psi|^2 \neq 0$ than $|\psi|^2 = 0$. In Eq. (2.10), $H_c(T)$ has a dependence with the term $(1-t)$, where $t = T/T_c$. On another hand, if $H_c(T)$ and a_s are related by Eq. (2.15), then it is expected that $a_s(T)$ to have some kind of dependence with $(1-t)$. We can use Taylor's series expansion of $a_s(T)$ about T_c and retain only the first term

$$a_s(t) = \dot{a_s}(t-1), \tag{2.16}$$

where $\dot{a_s} > 0$. Note that, Eq. (2.16) is consistent with Eqs. (2.15) and (2.10). Now let us consider the remaining term in the expansion from Eq. (2.12). Since ψ is a complex number we can rewrite it as $\psi = |\psi| e^{i\phi}$, where $|\psi|$ is the amplitude and ϕ the phase of the order parameter. The term with the fields and gradients of Eq. (2.12) rewrites as

$$\frac{1}{2m^*}\left[\hbar^2(\nabla|\psi|)^2 + \left(\hbar\nabla\phi - \frac{e^*}{c}\mathbf{A}\right)|\psi|^2\right]. \tag{2.17}$$

The first term is the energy associated with the gradients, the second is the kinetic energy associated with the supercurrents in the gauge-invariant form. Here we can link the GL theory with the London theory of superconductivity [1]. In London's theory, the superconductivity is described in terms of the n_s, the *number density of superconducting electrons*, that would vary continuously from zero at T_c to a limiting value than $T \ll T_c$. In London's theory, kinetic energy is

$$K_{\mathrm{L}} = \frac{A^2}{2\mu_0 \lambda_{\mathrm{eff}}^2} \tag{2.18}$$

where λ_{eff} is the London's effective penetration depth. Using the London gauge in Eq.(2.17), ϕ

is constant and the kinetic term is reduced to

$$K_{\mathrm{GL}} = \frac{e^{*2}A^2|\psi|^2}{2m^*c^2} \tag{2.19}$$

Equating Eq. (2.18) and Eq. (2.19), we obtain

$$\lambda_{\mathrm{eff}}^2 = \frac{m^*c^2}{\mu_0|\psi|^2e^{*2}}. \tag{2.20}$$

Comparing with London's λ

$$\lambda_L^2 = \frac{mc^2}{\mu_0 n_s e^2}, \tag{2.21}$$

we can identify that $|\psi|^2 = n_s^*$, and we have an effective mass m^* and effective charge e^*. Experimental data are fitted better if this effective charge is twice the value of a single electron, $e^* \approx 2e$. The microscopic pairing theory of superconductivity explicitly takes $e^* = 2e$. Then, we can take $m^* = 2m$ and $n_s^* = \frac{1}{2}n_s$, where n_s is the number of single electrons in the condensate and n_s^* the number of electrons pair. The penetration depth coefficient is equal

$$\frac{m^*}{n_s^*e^{*2}} = \frac{m}{n_s e^2}, \tag{2.22}$$

and London's penetration depth is unchanged by the electron pairing. We can evaluate the GL theory parameters by using Eqs. (2.14), (2.15) and (2.20)

$$|\psi_0|^2 = \frac{1}{2}n_s = \frac{mc^2}{8\pi e^2\lambda_{eff}^2}, \tag{2.23}$$

$$a_s(T) = -\frac{2e^2}{mc^2}H_c^2(T)\lambda_{eff}^2, \tag{2.24}$$

$$b_s(T) = \frac{16\pi e^4}{m^2c^4}H_c^2(T)\lambda_{eff}^4. \tag{2.25}$$

Notice that, by inserting the empirical approximations for $H_c \approx H_c(0)[1-t^2]$ and $\lambda^{-2} \approx \lambda(0)[1-t^4]$ into the equations above and using the Taylor expansion, we find

$$|\psi_0|^2 \propto 1-t^4 \approx 4(1-t) \tag{2.26}$$

$$a_s \propto \frac{1-t^2}{1+t^2} \approx 1-t \tag{2.27}$$

$$b_s \propto \frac{1}{1+t^2} \approx \text{const} \tag{2.28}$$

In the GL theory is customary to carry only the leading dependence on temperature; i.e., $|\psi_0|^2$ and a_s are usually taken to vary as $(1-t)$ and b_s constant.

2.3 Ginzburg-Landau Differential Equations

Without boundary conditions, the free energy is minimized by having $\psi = \psi_0$ everywhere. But, when fields, currents, or gradients are imposed, the OP ψ adjusts to minimize the overall free energy given by Eq. (2.12). This variational problem leads to two differential equations, named the Ginzburg-Landau equations. In the first equation, the free energy is minimized with the OP ψ and the second with the potential vector $\mathbf{A}$

2.3.1 First GL equation

Using the Euler-Lagrange equation that minimizes the energy functional F about $\psi^\dagger$, we have:

$$\frac{\partial F}{\partial \psi^\dagger} - \nabla\left[\frac{\partial F}{\partial \nabla \psi^\dagger}\right] = 0, \tag{2.29}$$

where F is the volume integral of Eq. (2.12). Using $|\psi|^4 = (\psi^\dagger\psi)^2$, we have

$$\frac{\partial |\psi|^4}{\partial \psi^\dagger} = 2|\psi|^2\psi^\dagger \tag{2.30}$$

and rewriting the gradient term as

$$\left|\left(-i\hbar\nabla - \frac{e^*}{c}\mathbf{A}\right)\psi\right|^2 = \left(-i\hbar\nabla - \frac{e^*}{c}\mathbf{A}\right)\psi \cdot \left(i\hbar\nabla - \frac{e^*}{c}\mathbf{A}\right)\psi^\dagger$$

$$\left|\left(-i\hbar\nabla - \frac{e^*}{c}\mathbf{A}\right)\psi\right|^2 = \varphi \cdot \left(i\hbar\nabla - \frac{e^*}{c}\mathbf{A}\right)\psi^\dagger \tag{2.31}$$

where $\varphi = \left(-i\hbar\nabla - \frac{e^*}{c}\mathbf{A}\right)\psi$. From Eq. (2.29), we have

$$a_s\psi + b_s|\psi|^2\psi + \frac{1}{2m^*}\left[\varphi\left(-\frac{e^*}{c}\mathbf{A}\right)\right] - \frac{1}{2m^*}(i\hbar\nabla\varphi) = 0$$

$$a_s\psi + b_s|\psi|^2\psi + \frac{1}{2m^*}\left[\left(-i\hbar\nabla - \frac{e^*}{c}\mathbf{A}\right)\left(-\frac{e^*}{c}\mathbf{A}\right) - i\hbar\nabla\left(-i\hbar\nabla - \frac{e^*}{c}\mathbf{A}\right)\right]\psi = 0$$

$$a_s\psi + b_s|\psi|^2\psi + \frac{1}{2m^*}\left[\left(\frac{i\hbar e^*}{c}\nabla\mathbf{A} + \frac{e^{*2}}{c^2}\mathbf{A}^2\right) + (i\hbar)^2\nabla^2 + \frac{i\hbar e^*}{c}\nabla\mathbf{A}\right]\psi = 0$$

$$a_s\psi + b_s|\psi|^2\psi + \frac{1}{2m^*}\left[-\hbar^2\nabla^2 + \frac{2i\hbar e^*}{c}\nabla\mathbf{A} + \frac{e^{*2}}{c^2}\mathbf{A}^2\right]\psi = 0$$

$$a_s\psi + b_s|\psi|^2\psi + \frac{\hbar^2}{2m^*}\left[-\nabla^2 + \frac{2ie^*}{\hbar c}\nabla\mathbf{A} + \left(\frac{e^*}{c}\right)^2\mathbf{A}^2\right]\psi = 0$$

$$(a_s + b_s|\psi|^2)\psi + \frac{\hbar^2}{2m^*}\left[-i\nabla - \frac{e^*}{\hbar c}\mathbf{A}\right]^2\psi = 0 \tag{2.32}$$

The first GL equation is thus similar to the Schrödinger equation, but with a second-order term, which makes it a non-linear equation. Because of this term, the superposition principle cannot be applied.

2.3.2 Second GL equation

The Euler-Lagrange equation about the potential vector **A** is

$$\frac{\partial F}{\partial \mathbf{A}} - \nabla \left[\frac{\partial F}{\partial \nabla \times \mathbf{A}} \right] = 0, \tag{2.33}$$

Re-writing the gradient term as Eq. (2.31) and using the magnetic field as $\mathbf{B} = \nabla \times \mathbf{A}$, we find the second GL equation

$$\mathbf{J} = \frac{-ie^*\hbar}{2m^*} \left(\psi^\dagger \nabla \psi - \psi \nabla \psi^\dagger \right) - \frac{e^{*2}}{m^* c} |\psi|^2 \mathbf{A} \tag{2.34}$$

where

$$\mathbf{J} = \frac{c}{4\pi} \nabla \times \nabla \times \mathbf{A} \tag{2.35}$$

The boundary condition used by Ginzburg-Landau to carry through the variational process is

$$\left(\frac{\hbar}{i} \nabla - \frac{e^*}{c} \mathbf{A} \right) \psi \Big|_n = 0 \tag{2.36}$$

which assures that no current passes through the surface.

2.4 Superconductors' characteristic lengths

2.4.1 Coherence Length

The equations (2.32) and (2.34) are the core of the GL theory. Solving both equations with the appropriate boundary conditions is no easy task, and most solutions are only achieved through numerical methods. One of the problems that have an analytical solution is the interface between a superconductor and normal states. Suppose the interface is contained in the yz plane and separates the metal region, $x < 0$, from the superconductor, $x > 0$, as shown in Fig. 5. In the absence of magnetic field $\mathbf{A} = 0$, the first GL equation is

$$-\frac{\hbar^2}{2m^*} \frac{\mathrm{d}^2 \psi}{dx^2} + (a_s + b_s |\psi|^2) = 0. \tag{2.37}$$

Using $f = \psi/\psi_0$, where $\psi_0^2 = -a_s/b_s > 0$, the Eq. (2.37) can be written as

$$\frac{\hbar^2}{2m^*|a_s|} \frac{\mathrm{d}^2 f}{dx^2} + f - f^3 = 0 \tag{2.38}$$

We can define the coherence length $\xi(T)$ as

$$\xi^2(T) = \frac{\hbar^2}{2m^*|a_s(T)|} \tag{2.39}$$

The Eq. (2.38) takes the form

$$\xi^2(T)\frac{\mathrm{d}^2 f}{\mathrm{d}x^2} + f - f^3 = 0, \tag{2.40}$$

whose solution is[47]

$$\psi(x) = \psi_0 \tanh\left(\frac{x}{\sqrt{2}\xi(T)}\right) \tag{2.41}$$

The significance of $\xi(T)$ as a characteristic length is evident by plotting the solution in the interface, like Fig. 5. It measures the distance of the interface that the order parameter increases

Figure 5 – Superconductor solution in interface

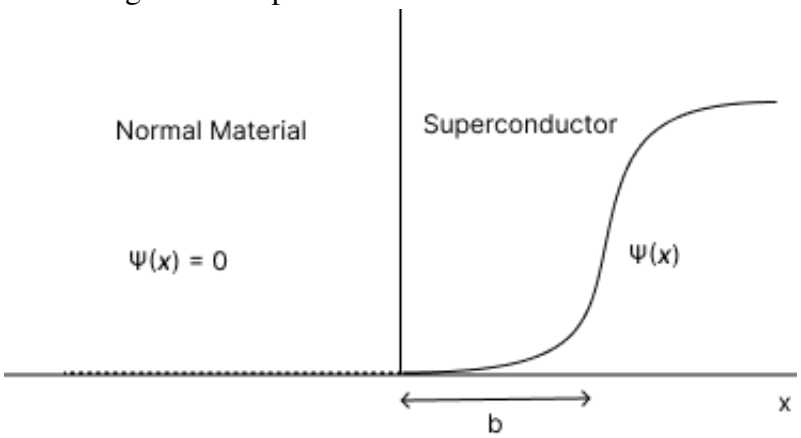

Source: Author's figure. Schematic diagram illustrating the variation of ψ in an interface. The length b is the length at which OP ψ increases to ψ_0 inside the superconductor.

to the maximum value of ψ_0 in the interior of the superconductor.

We can use Eq. (2.24) to calculate ξ,

$$\xi(T) = \frac{\Phi_0}{2\sqrt{2}\pi H_c(T)\lambda_{eff}(T)} \tag{2.42}$$

where

$$\Phi_0 = \frac{hc}{e^*} = \frac{hc}{2e} \tag{2.43}$$

is the flux quantum. This parameter plays an important role in type-II superconductors, where magnetic field can penetrate the superconductor above a lower critical field in the form of vortices carrying quantized magnetic flux.

2.4.2 London's penetration length

Let the same interface include a magnetic field on the z-axis. Assume the superconductor is homogeneous, that is, $|\psi|^2 = \psi_0$. The second GL equation is used to calculate the change in the magnetic field inside the superconductor. Using Eq. (2.34)

$$\mathbf{J} = -\frac{e^{*2}}{m^* c}|\psi|^2 \mathbf{A}. \tag{2.44}$$

Applying the rotational, we obtain

$$\nabla \times \mathbf{J} = -\frac{e^{*2}}{m^* c}|\psi|^2 \nabla \times \mathbf{A}. \tag{2.45}$$

Using the relations $\nabla \times \mathbf{J} = \nabla \times \nabla \times \mathbf{H}$ and $\nabla \times \mathbf{A} = \mathbf{H}$, we get,

$$\nabla \times \nabla \times \mathbf{H} = -\frac{e^{*2}}{m^* c}|\psi|^2 \mathbf{H}, \tag{2.46}$$

and using the vector identity $\nabla \times \nabla \times \mathbf{H} = \nabla(\nabla \cdot \mathbf{H}) - \nabla^2 \mathbf{H}$, we get the differential equation

$$\nabla^2 \mathbf{H} = \frac{e^{*2}}{m^* c}\frac{|a_s|}{b_s}\mathbf{H} \tag{2.47}$$

The solution to this equation

$$H = H_0 \mathrm{e}^{-z/\lambda(T)} \tag{2.48}$$

where λ is London's penetration length. This is roughly the distance that the magnetic field penetrates the superconductor before being suppressed, as illustrated in Fig. 6. With these two

Figure 6 – Magnetic field at the interface of superconductor

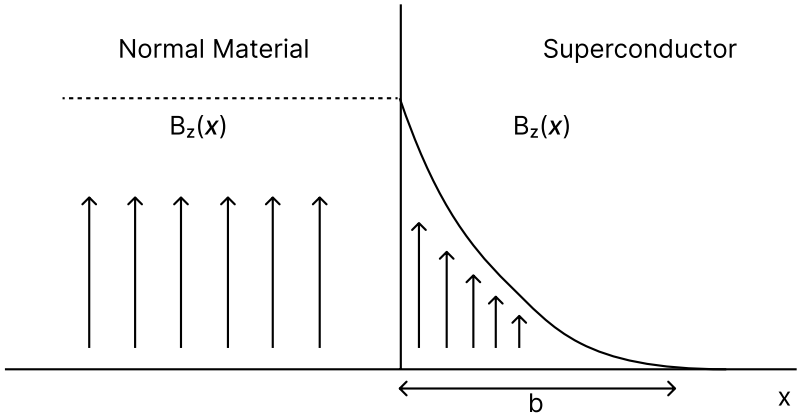

Source: Author's figure. Schematic diagram illustrating the variation of B_z in an interface. The length b is the length at which magnetic field B_z decreases to zero inside the superconductor.

characteristic lengths, we can characterize superconductors.

Ginzburg and Landau introduced a dimensionless parameter that does not depend

on temperature,

$$\kappa = \frac{\lambda(T)}{\xi(T)} \tag{2.49}$$

This GL parameter was used by A. Abrikosov to classify superconductors into two types: Type-I ($\kappa < 1/\sqrt{2}$) and Type-II ($\kappa > 1/\sqrt{2}$). Type-I superconductors destroy the superconductivity when the critical field is reached. Type-II superconductors were discovered when A. Abrikosov [9] studied what would happen if $\xi(T) < \lambda(T)$. His article demonstrated that, for this type of superconductor, there was a second-order phase transition about the magnetic field. In place of the abrupt destruction of superconductivity, Abrikosov has shown a continuous growth of the magnetic flux within the superconductor from a critical field H_{c1} to a second critical field H_{c2} where superconductivity is destroyed.

3 CHARGE DENSITY WAVES

Besides the superconducting phase, electronic phases with broken symmetries are amongst the most interesting topics in current research on solid-state physics. Density waves are broken symmetry states due to electron-phonon or electron-electron interaction, creating an inhomogeneous charge distribution with periodicity different from the periodicity of the crystal. When the state originates from electron-phonon interactions, it creates a charge density wave (CDW). Else, if it originates from electron-electron correlations, it is characterized as a spin density wave.

Fröhlich and Peielrs[48, 49] made the first theoretical prediction of the charge density wave in 1954 and 1955, respectively. They predicted that a highly anisotropic band structure is necessary to observe this state. The first experimental observation of charge density waves happened much later, when low-dimensional materials were discovered and studied, see e.g. [43, 50–53].

This chapter focuses on introducing the most relevant aspects of CDW and presenting the concepts of commensurate and incommensurate CDW. For a more in-depth overview of the topic, see [25, 43, 54, 55].

3.1 Peierls transition and Kohn anomaly

Since low dimensionality is required to observe CDW phases, reviewing some useful results from the one-dimension electron gas is essential.

The energy dispersion of electrons is

$$\varepsilon(k) = \frac{\hbar^2 k^2}{2m} \tag{3.1}$$

and its Fermi energy is

$$\varepsilon(k_F) = \frac{\hbar^2 k_F^2}{2m}, \tag{3.2}$$

where k_F is the Fermi wave vector. Let us consider a time-independent potential $\phi(\mathbf{r})$ acting on the electron gas. The charge density $\rho(\mathbf{r})$ is rearranged following the expression

$$\rho(\mathbf{q}) = \chi(\mathbf{q})\phi(\mathbf{q}) \tag{3.3}$$

where $\mathbf{q}$ is the wave vector in the momentum space and $\chi(\mathbf{q})$ is the Lindhard response function

given by, in d dimensions:

$$\chi(\mathbf{q}) = \int \frac{d\mathbf{k}}{(2\pi)^d} \frac{f_k - f_{k+q}}{\varepsilon_k - \varepsilon_{k+q}} \tag{3.4}$$

$f_k = f(\varepsilon_k)$ is the Fermi distribution function. Solving for one dimension, assuming a linear dispersion function, we get

$$\chi(q) = -e^2 n(\varepsilon_F) \ln \left| \frac{q+2k_F}{q-2k_F} \right| \tag{3.5}$$

where $n(\varepsilon_F)$ is the density of states at the Fermi level. Notice that χ diverges for $q = 2k_F$, known as Kohn anomaly, as seen in Fig. 7. The Kohn anomaly implies that, at $T = 0$, the

Figure 7 – Lindhard response and Kohn anomaly

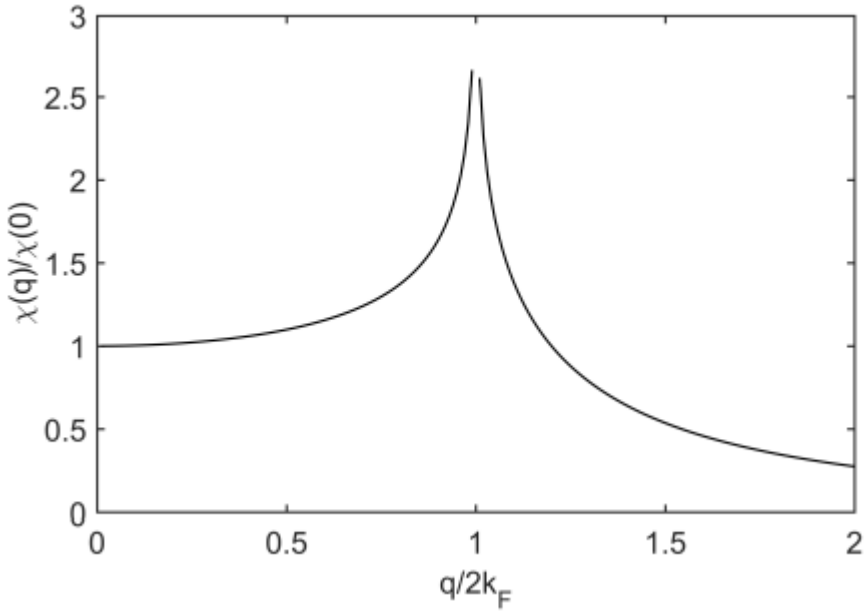

Source: Figure extracted from [43]. Susceptibility of the 1D electron gas as a function of wave-vector. When $q = 2k_{\mathrm{F}}$, the Lindhard response diverge, characterizing the Kohn anomaly.

electron gas is unstable to the formation of a periodically varying electron density. This leads to a phase transition to the CDW state, known as the Peierls transition.

The transition is a consequence of strong electron-phonon coupling and we can use the mean-field description to write a Hamiltonian for the interactions

$$H = \sum_{\mathbf{k}} \varepsilon_{\mathbf{k}} c^\dagger_{\mathbf{k}} c_{\mathbf{k}} + \sum_{\mathbf{q}} \hbar\omega_{\mathbf{q}} b^\dagger_{\mathbf{q}} b_{\mathbf{q}} + \sum_{\mathbf{k},\mathbf{q}} g_{\mathbf{q}} c^\dagger_{\mathbf{k}+\mathbf{q}} c_{\mathbf{k}} (b^\dagger_{-\mathbf{q}} + b_{\mathbf{q}}). \tag{3.6}$$

Equation (3.6) is called the Fröhlich Hamiltonian, where the first term is the electron gas Hamiltonian with $c^\dagger_{\mathbf{k}}$ and $c_{\mathbf{k}}$ being the creation and annihilation operators for the electron states. The second term is the phonon Hamiltonian, where $b^\dagger_{\mathbf{q}}$ and $b_{\mathbf{q}}$ are the creation and annihilation operators for the phonon with wave-vector $\mathbf{q}$ and normal mode frequencies $\omega_{\mathbf{q}}$. The last term is the electron-phonon interaction Hamiltonian, where $g_{\mathbf{q}}$ is the coupling constant.

Using the linear response theory and the equation of motion for the Hamiltonian (3.6), one finds the re-normalized phonon frequency

$$\tilde{\omega}_q^2 = \omega_q^2 \left(1 + \frac{2g_q^2}{\hbar\omega_q}\chi(q,T)\right). \tag{3.7}$$

Combining it with Eq. (3.5), one has

$$\tilde{\omega}_q^2 = \omega_q^2 \left(1 - \frac{2g_q^2 n(\varepsilon_F)}{\hbar\omega_q}\ln\left|\frac{q+2k_F}{q-2k_F}\right|\right). \tag{3.8}$$

For $q = 2k_F$, equation (3.8) becomes

$$\tilde{\omega}_{2k_F}^2 = \omega_{2k_F}^2 \left(1 - \frac{2g_{2k_F} n(\varepsilon_F)}{\hbar\omega_{2k_F}}\ln(1.14\varepsilon_F/k_B T)\right). \tag{3.9}$$

A decrease in temperature softens the phonon mode. When temperature is low enough, the re-normalized frequency becomes $\tilde{\omega_q^2} = 0$. We can find the transition temperature using equation (3.9) with $\tilde{\omega_q^2} = 0$

$$k_B T_{CDW}^{mf} = 1.14\varepsilon_F \exp(-1/\lambda) \tag{3.10}$$

where λ is the dimensionless electron-phonon coupling constant

$$\lambda = \frac{g_{2k_F}^2 n(\varepsilon_F)}{\hbar\omega_{2k_F}}. \tag{3.11}$$

In summary, the Kohn anomaly indicates the electron gas is unstable to the formation of a periodic charge density and for temperatures low enough, given by equation (3.10), the electron-phonon coupling reaches the anomaly that leads to the phase transition to the CDW state. Below the transition temperature, a gap (Δ) opens in the single particle spectrum at the Fermi energy, much like in superconductivity. This gap follows the same characteristics of the Bardeen-Cooper-Schrieffer (BCS) theory, including its temperature dependence.

The periodic charge density that characterizes the CDW is described by an amplitude ρ_1, the wave-vector $\mathbf{q}_0$, and a phase φ

$$\rho(\mathbf{r}) = \rho_0 + \rho_1 \cdot \cos(\mathbf{q}_0 \cdot \mathbf{r} + \varphi), \tag{3.12}$$

where ρ_0 is the electron density in the normal state, ρ_1 is proportional to the gap and q_0 connects the electron-hole pairs in momentum space. The phase φ describes the relative position of the CDW to the atomic lattice. In the following chapters, we will see that the density modulation $\delta\rho = \rho - \rho_0$ is proportional to a complex order parameter, and we will formulate a theory

similar to the Ginzburg-Landau theory for superconductivity, but for CDW in transition-metal dichalcogenides.

3.2 Commensurate and Incommensurate CDW

For a one-dimensional system, one can sketch the periodic charge density in a very simplistic way. Imagine a chain of ions placed at a distance a_L from each other - this is the lattice period. In the first site, there is a high charge density. In the following site, a lower charge density and the alternation from high to low continue along the lattice. This CDW is the so-called *commensurate* CDW. This specific case, where the CDW period is $2a_L$, is illustrated in Fig. 8.

Figure 8 – Sketch of the charge density wave in an ion lattice

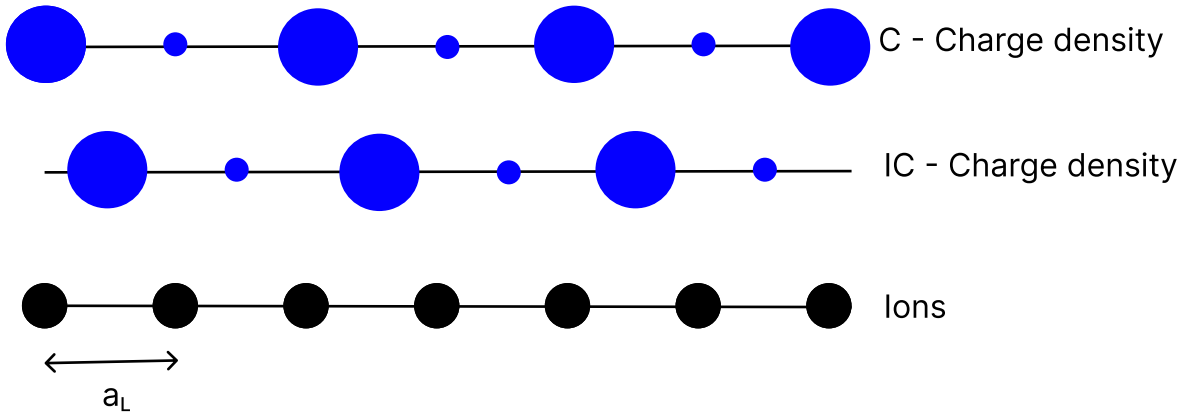

Source: Figure adapted from [56]. Sketch of the C-CDW (top) and IC-CDW (middle) in a periodic ion lattice.

In a three-dimensional case, one simply writes the CDW in terms of the reciprocal lattice vectors $\mathbf{q_0} = \alpha\mathbf{a} + \beta\mathbf{b} + \gamma\mathbf{c}$. If the numbers α, β, and γ are all rational, the CDW is commensurate. Otherwise, if any of them is irrational, we have incommensurate ordering, in which case the wave-vector is not aligned/commensurate with the ion lattice.

4 MCMILLAN THEORY FOR CDW IN TRANSITION-METAL DICHALCOGENIDES

In the previous Chapter, we discussed the main characteristics of the CDW from a broad point of view. Much like the SC, the phase transition to CDW opens a gap in the energy spectrum, and a complex order parameter describes both. In the case of the CDW, it is defined as

$$\psi = \Delta e^{i\phi} = g_{\mathbf{q}_0} \langle b_{\mathbf{q}_0} + b_{-\mathbf{q}_0} \rangle \tag{4.1}$$

These similarities inspired W. L. McMillan[22–24] to develop a theory to describe the particularities of the CDW in transition-metal dichalcogenides (TMDs). Let's start by giving an overview of the characteristics of this family of materials and then introduce the McMillan model.

4.1 TMDs: Overview

The TMDs are layered materials, where each layer consists of transition-metal ions in a central plane forming a triangular lattice, surrounded by two sheets of a triangular lattice of chalcogen atoms, one above and one below, as seen in Fig. 9(a,b). The intra-sheet bonds are predominantly covalent, while each layer is maintained by a weak van der Waals force. The way the layers are stacked can vary, each variation is called polytype, making this family even bigger. The two main polytypes used in the experimental studies and in the theoretical study of Chen *et. al.* are the 1T and the 2H polytypes. In the 1T polytype, the unit cell is composed of a single sheet and the metal atom sits in the center of a chalcogen octahedron. In the 2H polytype, the metal atom has trigonal prismatic coordination and two sheets are involved in the unit cell.

There are numerous TMDs that can be studied that are notable for their robust CDW and SC phases. But the low charge density of 1T-$TiSe_2$ makes it easier to spot the transition between the C-CDW, IC-CDW, and NC-CDW, as well as the presence of a superconductor dome.

Pristine niobium diselenide $2H - NbSe_2$ is a superconducting TMD at ambient pressure with a superconducting transition temperature $T_{sc} = 7$ K. It can be found in different polytypes, it is most commonly studied in the 2H phase in which the lattice constant is $a = 3.45$ angstrom. The material not only has a natural superconductivity phase, but also a CDW state that can be incommensurate which when suppressed enhances the superconductivity critical

Figure 9 – Sketch of the Fermi surface of 1T-TaS_2

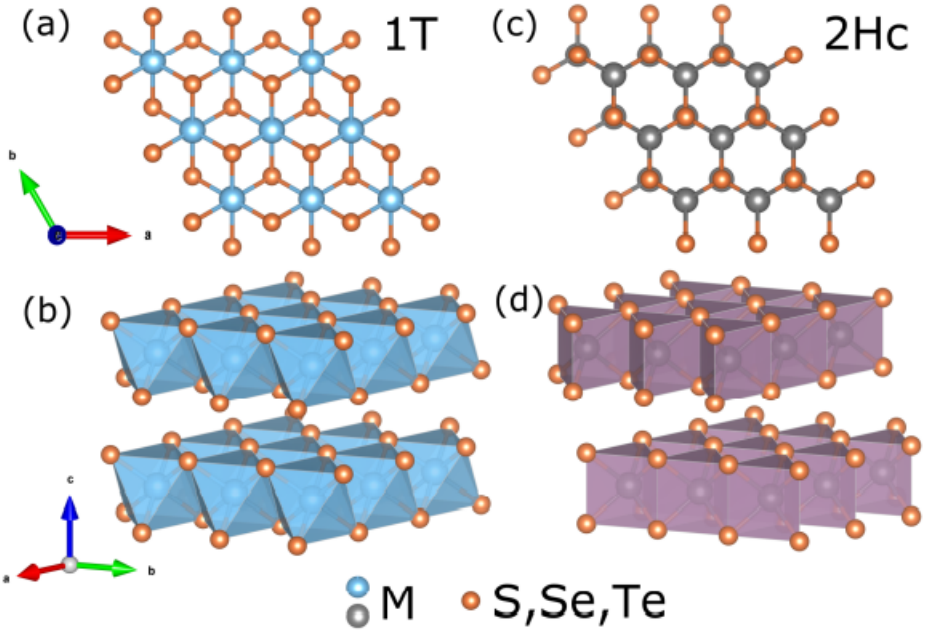

Source: Figure from [43]. Crystal structures of transition metal dichalcogenides.

temperature[43].

4.2 McMillan model

The two-dimensional CDW in these layers is formed in the ΓM directions. The 2D CDW in TMDs is composed of three coexisting 1D CDW, one in each direction of the reciprocal vectors $\mathbf{q}_i$. Fig 10 is a sketch of the Fermi surface for the TMD $1T-TaS_2$, where these lattice vectors are illustrated.

Within this framework, we use an extension of the McMillan functional to account for the symmetries of transition metal dichalcogenides[57]. We start with the density modulation for a commensurate CDW (C-CDW),

$$\rho(\mathbf{r}) = \sum_j e^{i\mathbf{r}\cdot\mathbf{Q}_j^C} \psi_j + c.c. \tag{4.2}$$

where ψ_j is the OP associated to the commensurate wave-vectors in each j-th direction $\mathbf{Q}_j^C$, that are multiples of the primitive reciprocal vector $\mathbf{G}_j$ of the material.

The McMillan-Ginzburg-Landau (MGL) energy functional for TMDs carries the contribution of the three order parameters ψ_j,

$$f_{\text{MGL}} = f_0 + f_1, \tag{4.3}$$

Figure 10 – Sketch of the Fermi surface of 1T-TaS_2

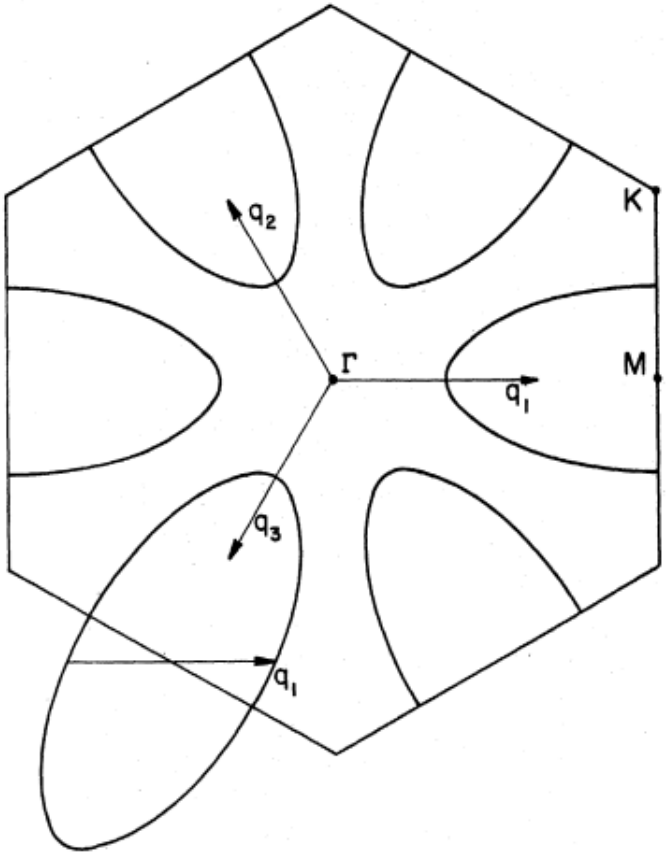

Source: Figure from [22]. Sketch of the Fermi surface of 1T-TaS_2 of the first Brillouin zone. The three vectors of the three CDW form the complete CDW and are separated by a 120º angle.

where f_0 is the conventional Ginzburg-Landau-like portion,

$$f_0(\mathbf{r}) = \sum_j \left[\alpha\tau|\psi_j|^2 + G|\psi_j|^4 + B\left|\left(i\nabla + \mathbf{q}_j^I\right)\psi_j\right|^2 \right] \tag{4.4}$$

where α, G, and B are phenomenological parameters, much like the ones for superconductivity. The parameter $\tau = T/T_{cdw} - 1$ is the effective temperature. The parameter $\mathbf{q}_j^I$ is the incommensurability vector defined as

$$\mathbf{q}_j^I \equiv \delta_j \mathbf{Q}_j^C. \tag{4.5}$$

The CDW OP can be re-written in terms of their amplitude $\phi_j(\mathbf{r})$ and phase $\theta_j(\mathbf{r})$ as

$$\psi_j(\mathbf{r}) = \phi_j(\mathbf{r})\mathrm{e}^{i\theta_j(\mathbf{r})}. \tag{4.6}$$

The phase parameter quantifies the deviations in comparison to the commensurate wave-vector which we can define in terms of the incommensurability vector $\theta_j(\mathbf{r}) = \mathbf{q}_j^I \cdot \mathbf{r}$. Combining

equations (4.2), (4.5) and (4.6) leads to an effective wave-vector,

$$\mathbf{Q} = \mathbf{Q}_j^C(1+\delta_j). \tag{4.7}$$

It is easy to see that, when the parameter δ is an integer, the effective wave-vector is multiple of the commensurate wave-vector, leading to a commensurate state. When δ is not an integer, the effective wave-vector deviates from the commensurate state to the incommensurate one in the j direction.

The second term of the MGL energy functional gathers the possible (symmetry-allowed) couplings between order parameters,

$$f_1 = -\frac{E}{2}\sum_j \left(\psi_j^2 + \psi_j^{\dagger 2}\right) - \frac{3D}{2}\left(\psi_1\psi_2\psi_3 + c.c.\right) + \frac{K}{2}\sum_{i,j>i}\left|\psi_i\psi_j\right|^2 - \frac{M}{2}\sum_{j,k\neq l\neq j}\left(\psi_j\psi_k^*\psi_l^* + \text{c.c.}\right), \tag{4.8}$$

where E, D, K and M are coefficients to map the symmetries of the TMDs.

From f_0, the B term favors the incommensurate solution, by yielding lower energy as $\theta_j(\mathbf{r}) \to \mathbf{q}_j^I \cdot \mathbf{r}$. On the other hand, the $E > 0$ term in f_1 favors the commensurate solution: since $(\psi_j^2 + \psi^{\dagger 2}) = 2\phi_j^2\cos(2\theta_j)$, the energy is minimized as the phase approaches $n\pi$, for integer n. The parameter E is called lock-in energy, which stabilizes the commensurate and incommensurate states, and is inversely proportional to the total electron density.

McMillan used the free energy to show that the phase transition between the commensurate and incommensurate states is a second-order phase transition, and defined a new defect in the commensurate CDW state, the discommensuration (DC)[23]. These DC are regions on a commensurate CDW state that exhibit an incommensurate CDW (IC-CDW) state in between them. In the free energy functional, equations (4.4) and (4.8), the balance between the lock-in term (E) and the B term dictates in what state the CDW is. For $E \to 0$, the B term minimizes the energy for the IC-CDW, while for $E \to \infty$, the lock-in term minimizes for the C-CDW. For values of E not extremely low or high, the CDW enters a mixed state of IC-CDW and C-CDW called the near-commensurate state (NC-CDW). In the NC-CDW, lock-in C-CDW states are separated by IC-CDW states, the DC. This behavior can be seen by plotting the CDW phase θ_j in real space, like shown in figure 11.

The flat horizontal regions are the C-CDW states with the rapidly varying phase regions in between are the DC, where the IC-CDW state is present. The NC-CDW state proposed

Figure 11 – DC in TMD materials

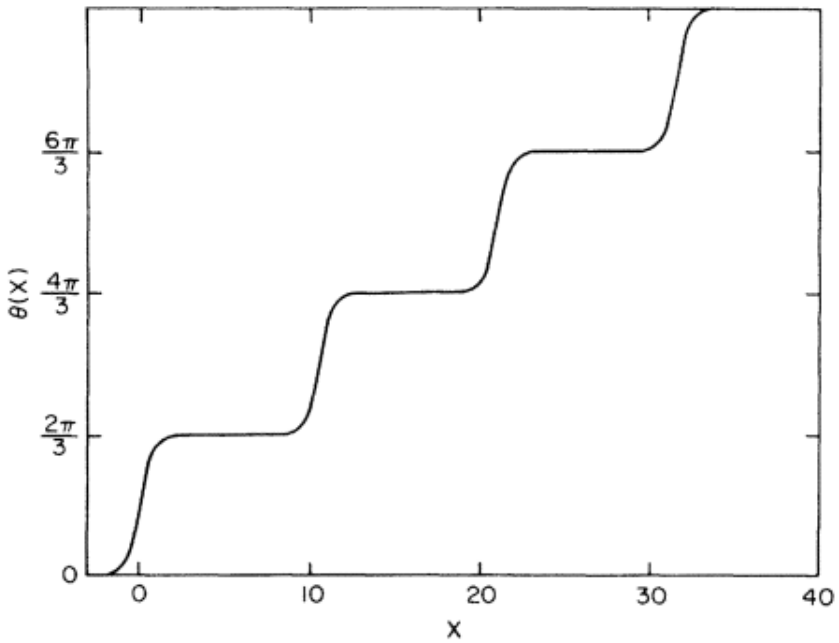

Source: Figure from [23]. DC of the CDW in 1T-TaS_2. The rapidly varying phases are the DC, where IC-CDW is preset, in between the commensurate phases.

by McMillan was studied primarily in the TMD $1T - TaS_2$ and in the charge-ordered phase of cuprate superconductors[58]. The study of Árpád Pásztor *et. al.*[43] used STM imaging on the material $2H - NbSe_2$ and not only confirmed the coexistence of three order parameters for CDW in this material but also found discommensurations, Fig. 12c, that mimics the McMillan prediction. Figs. 12a and b are the *in situ* cleaved surfaces and the phase map of one of the

Figure 12 – STM imaging of the CDW in $2H - NbSe_2$

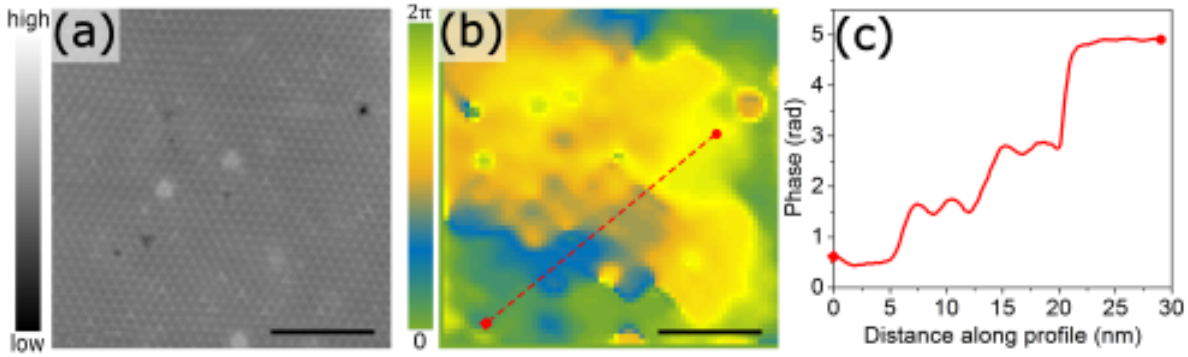

Source: Figure adapted from [43]. STM imaging of crystalline defects, CDW DC in 2H-$NbSe_2$. (a) STM micrograph with atomic defects. (b) Phase map of the corresponding q2 CDW. (c) Phase profile extracted from the diamond to the circle along the red dashed line in (b)

CDW, respectively.

In recent studies, the relationship between emergent superconductivity in doped TMDs and the CDW state were investigated. Experiments suggest the enhancement of super-

Figure 13 – Phase diagram of $1T - TaS_2$

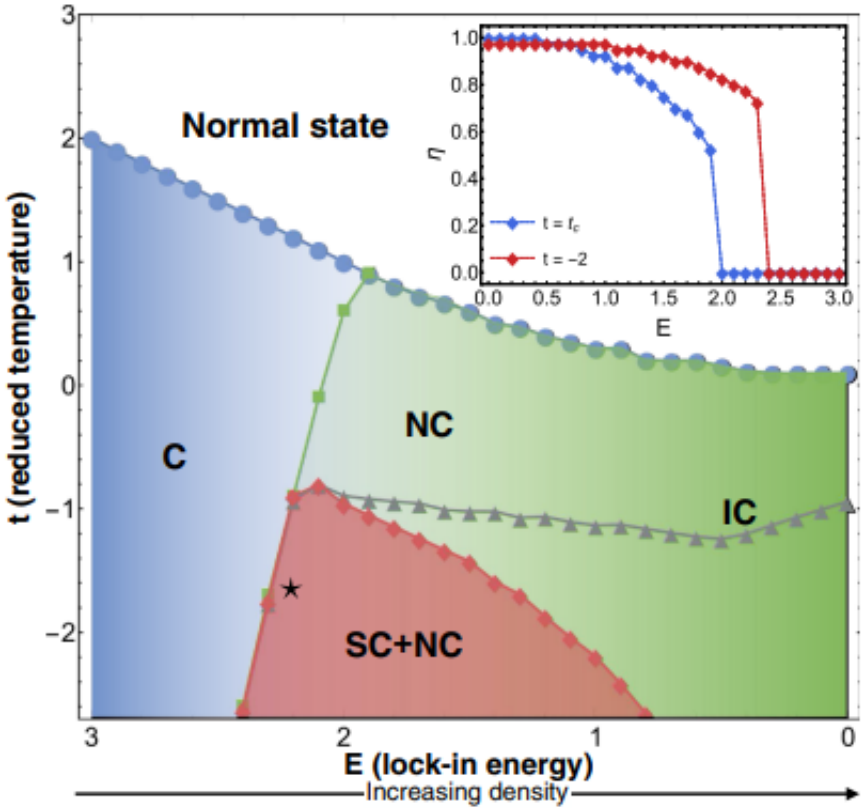

Source: Figure extracted from [57]. Phase diagram of $1T - TaS_2$. Labels C, NC, and IC stand for commensurate, near-commensurate, and incommensurate CDW phases, respectively. The lines are the transition boundary between each state. The inset shows the η which determines if the solution is C ($\eta = 0$), IC ($\eta = 1$), or NC, versus the lock-in energy.

conductivity in these materials is linked with the NC-CDW state and the DCs. Chen *et. al.* used the McMillan theory to describe the cooperative coexistence of the CDW and superconducting order in two-dimensional TMDs. They mapped the transition between the CDW states and monitored the development of the DC and found that the NC-CDW enhances nonuniform superconductivity. The phase diagram, Fig. 13, is in qualitative agreement with experiments.

In the phase diagram of t, the reduced temperature, versus E, the lock-in energy, the authors show the transition between the CDW states, going from the C-CDW to the NC-CDW and then to IC-CDW. Notice the increase in the critical temperature of the SC when the CDW is in the near-commensurate state suggesting that the DCs are related to the presence of superconductivity. In the next chapter, we will present our study that shows when there is competition between a collective state (like CDW) and SC, defects (or suppression) of the collective state enhance the presence of SC. This work suggests the DCs, which are defects of the C-CDW, make the superconductivity viable in TMDs, by increasing their critical temperature. In fact, our calculations demonstrate that several other types of defects experimentally observed e.g. by

[43], such as phase domain walls and vortex-antivortex pairs, can also be described by MacMillan theory provided we start from a proper choice of incommensuration vectors $\mathbf{q_j^I}$. The effect of these features in CDW on the SC critical temperature will be discussed later on, in Chapter 6.

5 LATENT SUPERCONDUCTIVITY AT PARALLEL INTERFACES IN A SUPERLATTICE DOMINATED BY ANOTHER COLLECTIVE QUANTUM PHASE

In the previous chapter, we presented the phase diagram for TMDs in which the critical temperature of the superconductivity increases as the CDW transition between the C, NC, and IC phases. This indicates an interplay between the CDW and SC.

Controlling and enhancing the thresholds of the SC phase is challenging. Over the past decades, multiple approaches have been proposed to enhance the critical temperature of different superconducting materials[59–67]. In iron pnictides and cuprates, the increase of the SC critical temperature is intimately connected with the competition between the SC and other collective quantum states[68–71]. These additionally ordered quantum phases may suppress SC by competing for the same electrons wrapped in the Cooper-pairing mechanism. Using a two-component GL model, Moor *et. al.*[72] provided a general analysis to describe the rise of the interface superconductivity as a hidden order parameter in a single interface between two separate regions where another collective phenomenon is dominant.

We develop an extension of the model to investigate the role of several parallel interface coupling on parameters such as SC critical temperature and Cooper pairs density.

5.1 Theoretical Model

Consider two OP, Δ and W, describing a (hidden) SC phase and another collective excitation, CDW for example. In a general way, the one-dimensional GL free energy is defined as

$$F = \int dx \left\{ \xi_s^2 (\nabla\Delta)^2 - a_s\Delta^2 + \frac{b_s}{2}\Delta^4 + \xi_w^2 (\nabla W)^2 - a_w(x)W^2 + \frac{b_w}{2}W^4 + \gamma W^2\Delta^2 \right\} \tag{5.1}$$

where ξ_i, a_i, and b_i are the usual phenomenological parameters in the GL formalism, while γ is the coupling term between the condensate densities. For a numerical approach, it is common to rewrite the free energy in a dimensionless form

$$\mathscr{F} = \int dx \left\{ \frac{1}{\delta^2}(\nabla\Delta)^2 + \frac{\xi_r^2}{\delta^2}\left[-a_s\Delta^2 + \frac{1}{2}\Delta^4 \right] + + (\nabla W)^2 - \Omega_w(x)W^2 + \frac{1}{2}W^4 + \sigma W^2\Delta^2 \right\} \tag{5.2}$$

where we use the unit of energy $F_0 = a_{w0}^2/b_w$ (a_{w0} is the parameter a_w in the bulk). The parameter $\delta = W_b/\Delta_b$ measures the relative strength between the maximum values of the OP in the

bulk. The coefficient

$$\xi_r^2 = \xi_w^2/\xi_s^2 \tag{5.3}$$

relates the coherence lengths of both OP, $\sigma = \gamma\delta^2/a_{w0}$, and $a_s = 1 - T/T_\Delta$, where T_Δ is the bulk critical temperature of the SC phase. In this framework, the parameter a_w is spacial-dependent $a_w \to a_w(x)$ to induce the suppression of the dominant OP W at the interfaces. In dimensionless form, we have $\Omega(x)$ takes this role

$$\Omega(x) = \begin{cases} -a_0, & |x-\chi_j| < L, \\ +1, & |x-\chi_j| \geq L \end{cases}, \tag{5.4}$$

where $a_0 \geq 0$, L is the width of the interfacial regions, and χ_j ($j = 1,2,3,\ldots,N$) is the position of the j-th interface.

Minimizing $\mathscr{F}$ with respect to Δ and W leads to two GL first equations

$$-\frac{\mathrm{d}^2 \mathrm{W}}{\mathrm{dx}^2} + \left[-\Omega_w(x) + W^2 + \sigma\Delta^2\right] W = 0 \tag{5.5}$$

$$-\frac{\mathrm{d}^2\Delta}{\mathrm{d}x^2} + \left[-a_s + \Delta^2 + \frac{\sigma\delta^2}{\xi_r^2}W^2\right]\Delta = 0. \tag{5.6}$$

Eqs. (5.5) and (5.6) are solvable numerically using a self-consistent relaxation procedure, and we will discuss the complete solution in a further section. But we will start with the solutions based on the linearized GL formalism, to gain insights into the physics behind the full equations.

Assuming a weak superconducting gap at the interface, higher-order terms of Δ can be neglected in Eqs. (5.5) and (5.6), so that

$$-\frac{\mathrm{d}^2 W}{\mathrm{d}x^2} + \left[-\Omega_w(x) + W^2\right] W = 0 \tag{5.7}$$

$$-\frac{\mathrm{d}^2\Delta}{\mathrm{d}x^2} + \left[-a_s + \frac{\sigma\delta^2}{\xi_r^2}W^2\right]\Delta = 0 \tag{5.8}$$

Starting with equation (5.7), we can solve it by means of the relaxation method. Using a finite-difference scheme on a uniform Cartesian grid with $0.1\xi_w$ spacing, an initial arbitrary trial function of $W(x)$ evolves in time as

$$W_i^{t+1} = W_i^t + dt\left[\frac{W_{i+1}^t - 2W_i^t + W_{i-1}^t}{2x^2} - \Omega_w^i W_i^t + (W_i^t)^3\right], \tag{5.9}$$

with a dimensionless time step $dt = 0.01$, until convergence is reached up to tolerance $\left|W_i^{t+1} - W_i^t\right| \leq 10^{-8}$ at any point in space x_i.

The converged solution for $W(x)$ is then used as input in Eq. (5.8)

$$-\frac{\mathrm{d}^2\Delta}{\mathrm{d}x^2} + \sigma\delta^2|W|^2\Delta = \varepsilon\Delta, \tag{5.10}$$

where $\varepsilon = \xi_r^2 a_s$ and the equation is discretized in the same spatial grid. Equation (5.10) is a Schrödinger equation for a $V = \sigma\delta^2|W(x)|^2$ potential. We can solve this eigenvalue equation numerically, which yields a series of solutions for the superconducting order parameter, each with an eigenvalue ε_n and a gap distribution $\Delta_n(x)$. The OP Δ is non-zero when in the interface, where the OP W is suppressed, thus describing interface superconducting states. This situation is sketched in Fig. 14.

Figure 14 – Sketch of a system with two adjacent interfaces

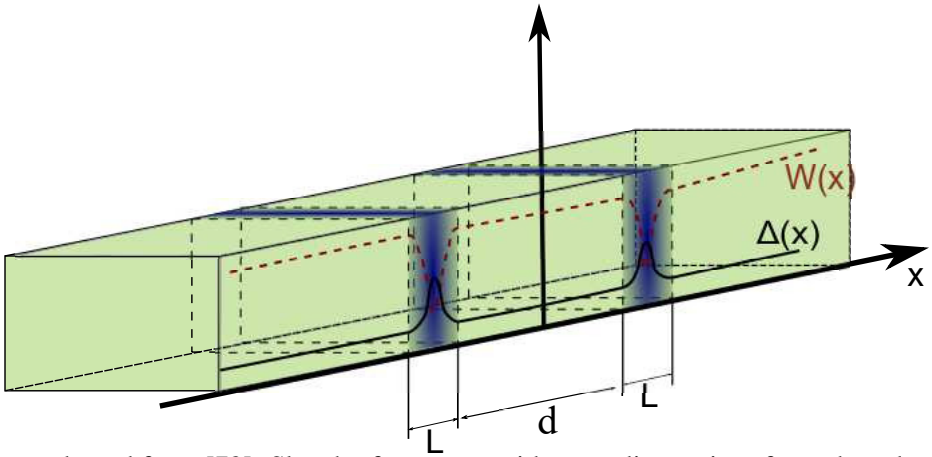

Source: Figure adapted from [72]. Sketch of a system with two adjacent interfaces, based on the single-interface system proposed in Ref. [72]. Here, the order parameter $W(x)$ (dashed line) describes a collective excitation (e.g. spin or charge density waves) dominating in the bulk (green), that is suppressed along parallel interfaces (blue) of width L, separated by distance d (see Eq. (5.4)). The hidden order parameter $\Delta(x)$, which describes the superconducting phase, arises at these interfaces (plotted as a solid line).

Given the temperature dependence of the parameters a_s and the value of ξ_r^2, we can obtain the critical temperature T_{cn} for each n-th superconducting eigenstate. Alternatively, we can solve Eq. (5.8) through the relaxation method to find the temperature dependence of the OP $\Delta_n(x)$. The solutions for the full non-linear GL equations are also obtained by the same procedure and the discussion on these is postponed to the final section of the chapter.

The model proposed in this chapter applies to superconductors with co-existing collective states, such as CDW. In the next chapter, we discuss how the MGL theory can be used to describe the DC in TMDs and how we can apply this general model to a specific material.

5.2 Interface eigenstates and their criticality

Moor *et. al.* did an extensive study of interface superconductivity in a single interface[72, 73] and showed that the eigenstates of Eq. (5.10) represent possible distributions of the SC OP $\Delta(x)$, each with different eigenvalue ε_n. The behavior is reminiscent of the eigenstates of the Schrödinger equation for a particle confined in a quantum well. For two or more parallel interfaces, Eqs. (5.9) and (5.10) were solved for the SC ground state in the interfaces. All interfaces will have the same width $L = 2\ \xi_w$ and the distance between the interfaces will vary in fractions of ξ_w.

The collective state $W(x)$ and the SC OP $\Delta(x)$ are shown in Fig. 15(a) and 15(b), respectively. The two interfaces are separated by distance $d = 12\ \xi_w$ and we assume the SC coherence length and the healing coefficient of W are equal, i.e. $\xi_w = \xi_s$ or $\xi_r = 1$. At the position, $\chi_1 = -6\ \xi_w$ and $\chi_2 = +6\ \xi_w$, the solution for Eq. (5.9) has two dips in the position of the interfaces with Ω_w given by Eq. (5.4), representing the suppression of the collective state.

Increasing the value of a_0 leads to a stronger suppression of W in the interface. We consider $a_0 = 1$ as a weak suppression and $a_0 = 5$ as a strong suppression. The two lowest eigenfunctions of the SC in the $a_0 = 5$ case are in Fig. 15 and their peaks at the interfaces, thus representing the rise of interface superconductivity. Note the symmetric and anti-symmetric character of the solutions which resembles the double quantum well.

In the double quantum well, the eigenvalues of the symmetric and anti-symmetric solutions becomes degenerate when the wells are far from each other. We expect the same to happen for the eigenvalues of Eq. (5.10) when the interfaces are far (i.e. $d \to \infty$), whereas this degeneracy is lifted as they are brought closer. This behavior is shown in Fig. 16, representing the eigenvalues ε of the SC states for the symmetric (black solid) and anti-symmetric (red dashed) eigenfunctions. Even small suppression of the W OP gives rise to interface superconductivity. Notice the dependence of the eigenvalues on the distance between interfaces d is affected by how strongly the other collective state is suppressed. In fact, in the case of a_0 is set to a high value, the W OP does not reach its maximum value in the region between interfaces as the distance between them is made shorter, as can be seen in the inset of Fig. 16(a). Notice that in the case of strong suppression, when $d < 2\ \xi_w$, the region in between the interfaces is also affected by the suppressed OP inside the interfaces, creating effectively a single region of weakly modulated OP, maximizing the induced SC Δ.

Figure 15 – Spatial distribution of the order parameters

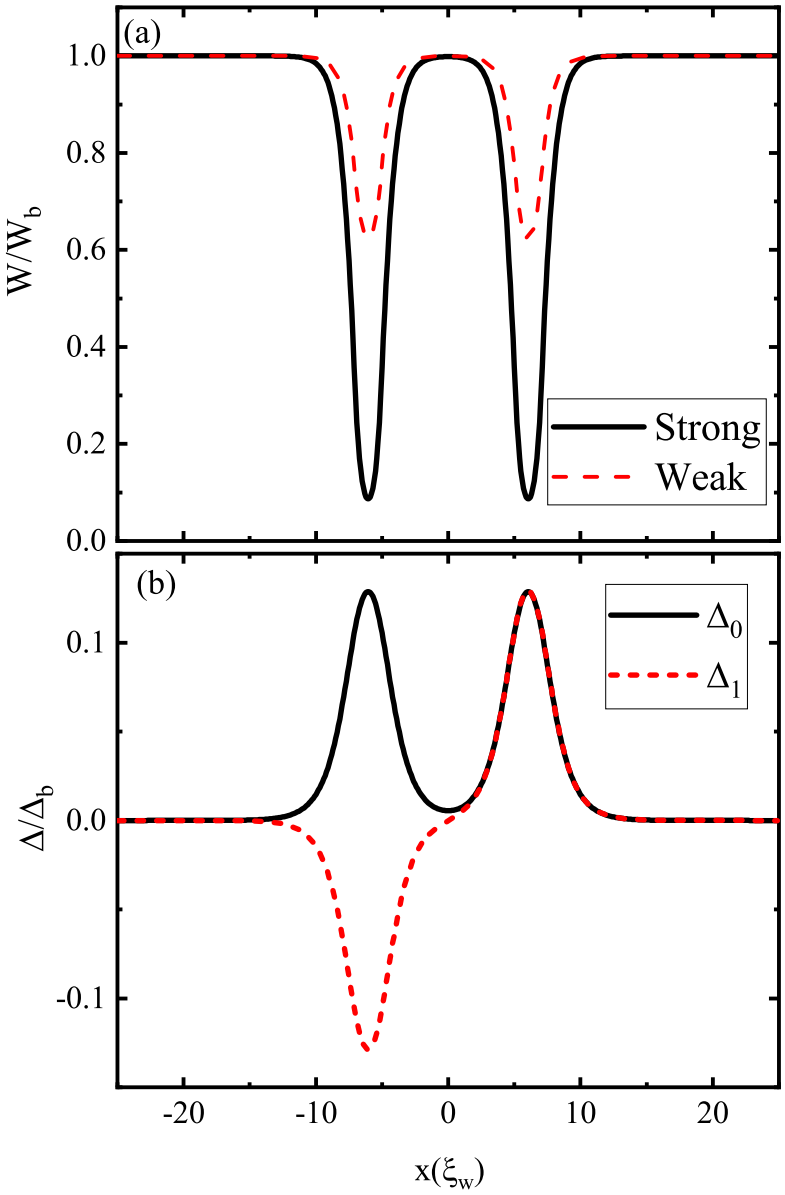

Spatial distribution of the order parameters (a) of the density wave W, assuming its strong ($\alpha_0 = 5$, solid line) and weak ($\alpha_0 = 1$, dashed line) suppression at the interfaces, and (b) lowest-lying eigenfunctions of the SC state Δ_n in the strong suppression case, for two interfaces of width $L = 2\ \xi_w$, separated by $d = 12\ \xi_w$ (cf. Fig. 14).

5.2.1 Tight-binding model for interface SC

The lift of the eigenstates degeneracy in Figs. 16(a,b) resembles the one in a double quantum well, where a tight-biding model can be developed. The same can be done for our system, re-writing the eigenvalue Eq. (5.8) as

$$D\Delta = \varepsilon\Delta \tag{5.11}$$

Figure 16 – Eigenvalues for two interfaces

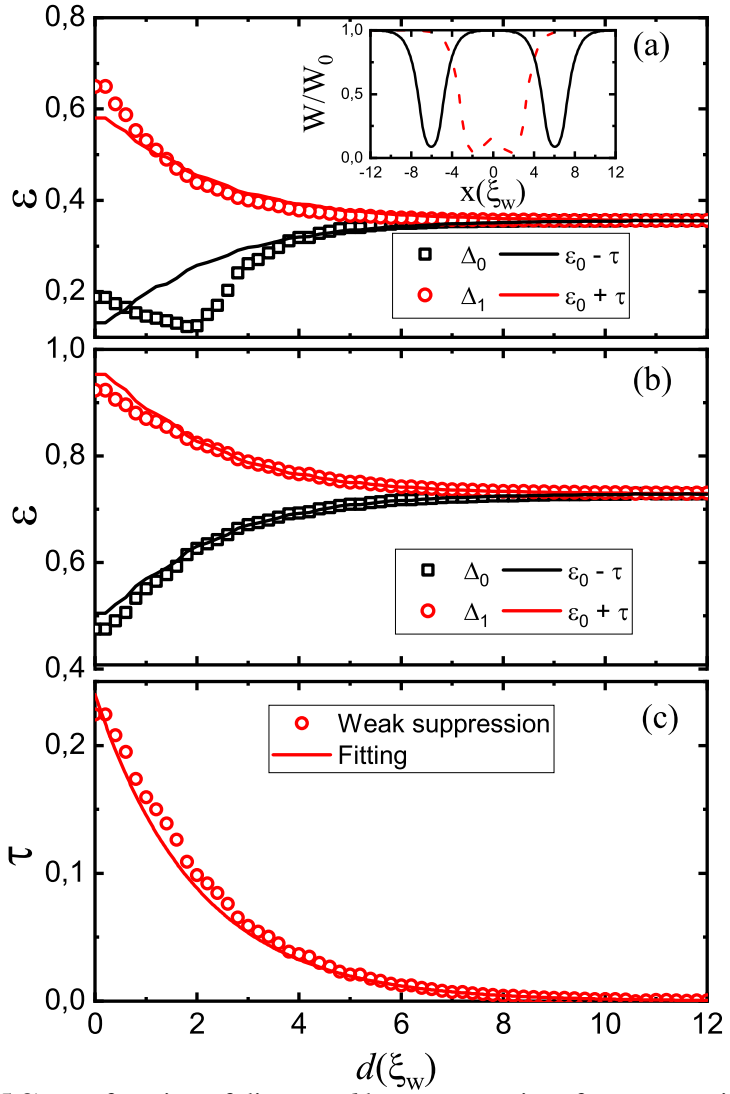

Eigenvalues of Eq. (5.8) as a function of distance d between two interfaces, assuming strong (a) and weak (b) suppression of the W order parameter W, i.e. with $\alpha_0 = 5$ and $\alpha_0 = 1$, respectively. Lines show the numerically obtained results for symmetric (black solid) and anti-symmetric (red dashed) eigenfunctions, while open symbols plot results of a tight-binding approach for the same states. (c) The calculated hopping parameter τ as a function of distance d for a weak suppression case (open symbols), with an analytical fitting function, plotted as well (solid curve). Inset in (a) shows the order parameter with $\alpha_0 = 5$ assuming $d = 4\xi_W$ (red dashed) and $d = 6\xi_W$ (black solid).

and the eigenvalues are obtained by diagonalization of the matrix D with the diagonal terms given by the ground state eigenvalue of each interface

$$D_{11} = D_{22} = \varepsilon_0, \tag{5.12}$$

and the off-diagonal

$$D_{21} = D_{12} = -\tau, \tag{5.13}$$

where τ plays the role of a hopping parameter between the interfaces. The diagonalization of the matrix leads to eigenvalues of

$$\varepsilon_{\pm} = \varepsilon_0 \pm \tau \tag{5.14}$$

along with symmetric and anti-symmetric eigenfunctions, qualitatively similar to those in Fig. 15(b). The hopping parameter τ increases with the distance d between the interface, controlling the separation between the eigenvalues. The results of the model are shown as open symbols in Figs. 16(a,b), with good agreement with the numerical results for weak suppression. For the strong suppression case, the tight-binding model results are good for larger interface separations. In comparison, it falls short for closer separations due to the W behavior explained in the previous section.

The dependence of the hopping parameter τ on the interface separation is plotted as open symbols in Fig. 16(c) for the weak suppression case. The tight-binding model can be expanded for multiple interfaces, which we investigate in the next section. To facilitate its use, the numerically obtained hopping parameters are fitted by the function

$$\tau(d) = \tau_{\max} \mathrm{e}^{-\frac{d}{2}}. \tag{5.15}$$

The fitted function is plotted as a solid curve in Fig. 16(c), using $\tau_{\max} = 0.24$. The importance of a simplistic model is to have a convenient way to estimate the eigenvalues for any number of interfaces.

5.2.2 Multiple interfaces

In the case of multiple interfaces, we first investigate a system consisting of 3 and 4 parallel interfaces and then generalize for any number of interfaces using the tight-binding model. The order parameter $W(x)$ for systems with interfaces separated by $d = 12\ \xi_w$ is shown in Figs. 17(a) and 17(b). The first 3 and 4 low-lying eigenfunctions $\Delta_n(x)$ are shown in Figs. 17(c,d), respectively. Interestingly, different eigenvalues produce eigenfunctions $\Delta_n(x)$ describing higher superconducting gaps at specific interfaces. For example, considering four interfaces, Δ_0 and Δ_3 states exhibit higher peaks at the two internal interfaces, while Δ_1 and Δ_2 peaks at the external. This suggests that as the system's temperature increases, the critical temperatures associated with ε_n sates are exceeded sequentially, and the superconducting states Δ_n becomes available one by one, each with a different spatial distribution of gaps among the interfaces. The solution for the full GL Eqs. (5.5) and (5.6) for Δ is a linear combination of the available

Figure 17 – Order parameter for 3 and 4 interfaces

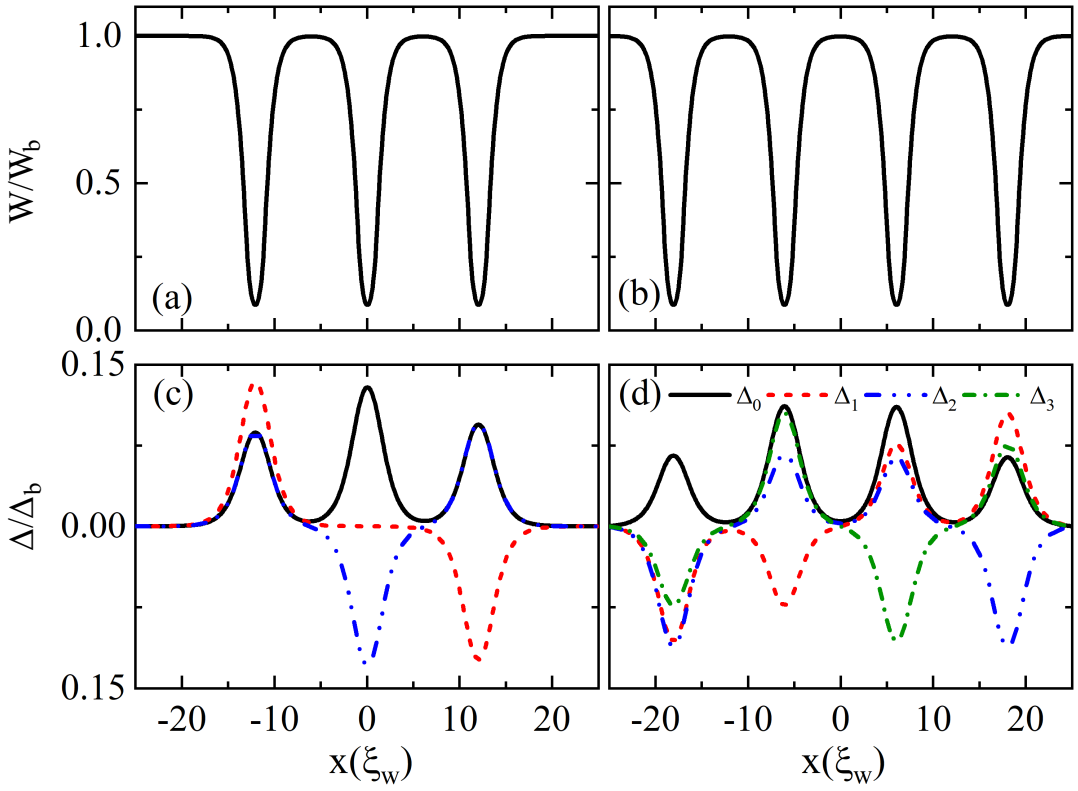

Order parameter W for a system consisting of (a) 3 and (b) 4 parallel interfaces, separated by distance $d = 12\ \xi_w$. The SC order parameters Δ_n of the first 3 and 4 low-lying eigenstates of these systems are shown in panels (c) and (d), respectively.

eigenstates Δ_n, therefore, as the temperature decreases (especially for rapid cooling), one may find solutions where Δ contains contributions of higher n eigenstates that lead to non-trivial spatial distributions of the Cooper-pairs condensate on the interfaces.

The numerically obtained ε_n eigenstates in systems with 3 and 4 interfaces are plotted as solid lines in Figs. 18(a) and 17(b), respectively, for the weak suppression case. Results obtained with the tight-binding model, using hopping parameters given by Eq. (5.15), are shown as open symbols, where good agreement is observed only for interface separations beyond $d \approx 4\ \xi_w$. As previously discussed, the disagreement between the numerical and the tight-binding results for shorter d has the same explanation as given for the disagreement for two interfaces in the strong suppression case, so that the problem of several interfaces with short separation can no longer be described as a combination of several single-interface problems in a tight-binding approach. For instance, in the case of 3 interfaces, even the intermediate eigenvalue state ε_1, which in the tight-binding model is a constant ε_0, starts to decrease as d becomes smaller in the actual system as a consequence of the decreasing $W(x)$ between the interfaces. In

Figure 18 – Eigenvalues of the SC order parameter for 3 and 4 interfaces

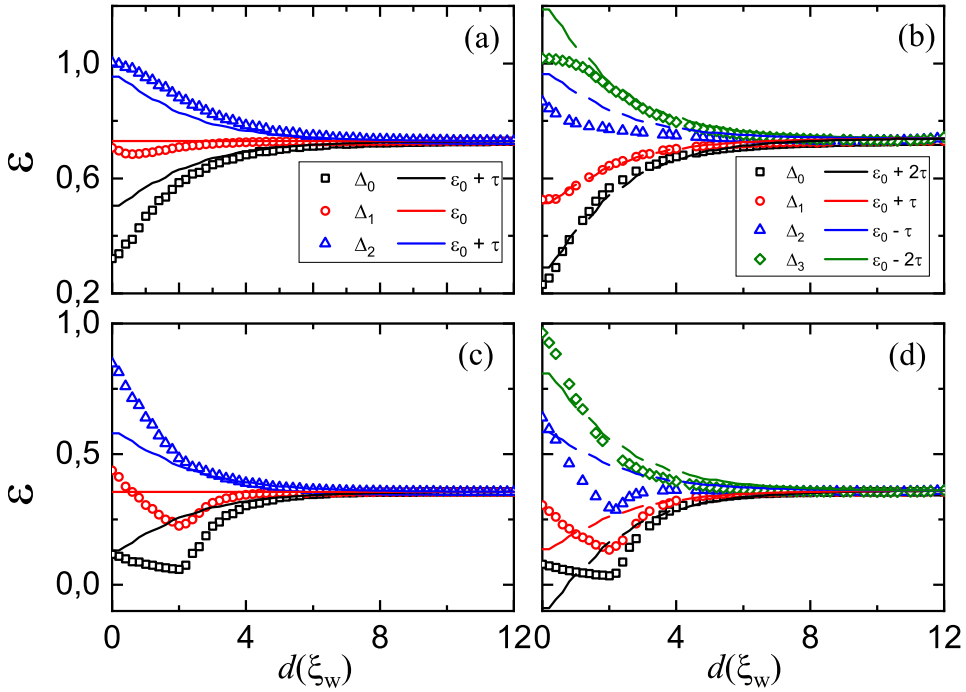

Eigenvalues of the SC order parameter, from Eq. (5.8), assuming (a,b) weak and (c,d) strong W suppression, in a system with (a,c) 3 and (b,d) 4 interfaces. For separation larger than $d \approx 4\ \xi_w$, the tight-binding model (symbols) predicts the eigenvalues reasonably well in all cases.

the case of strong suppression, this situation worsens, as shown in Figs. 17(c) and 17(d).

The sharp kinks seen in these figures result from the strong suppression in between the interfaces at small separation d, similar to those observed for the 2 interface case in Fig. 16(a). Nevertheless, the tight-binding model proposed here still yields a good quantitative prediction for $d > 4\ \xi_w$ in all cases, while preserving at least good qualitative predictions of the behavior of the eigenvalues in the weak-suppression regime even for smaller d.

The SC order parameter's maximum value, $\Delta_{max,n}$, offers us an estimation of the superconducting gap at the interfaces. As the temperature decreases below the critical temperature of the n-th eigenstate in Eq. (5.10), this value increases from zero. Although this equation determines each eigenstate's critical temperature T_{cn} through the relation $\varepsilon_n = \xi_r^2(1 - T_{cn}/T_\Delta)$, it does not provide the temperature dependence of each $\Delta_{max,n}$. To obtain this information, we use a relaxation procedure to solve Eq. (5.8) at various temperatures. The results are illustrated in Figs. 19(a) and (b), which plot $\Delta_{max,n}$ of the first three (four) states for a system with three (four) interfaces as a function of temperature.

We can now extend our results to the case of an infinite number of interfaces ($N \to \infty$) since the tight-binding model has reasonable reliability. For any value of N, the proposed tight-binding matrix D takes on the tri-diagonal Toeplitz form as described in [74]. Its

Figure 19 – Maximum values of the superconducting order parameter $\Delta_n(x)$ as a function of temperature

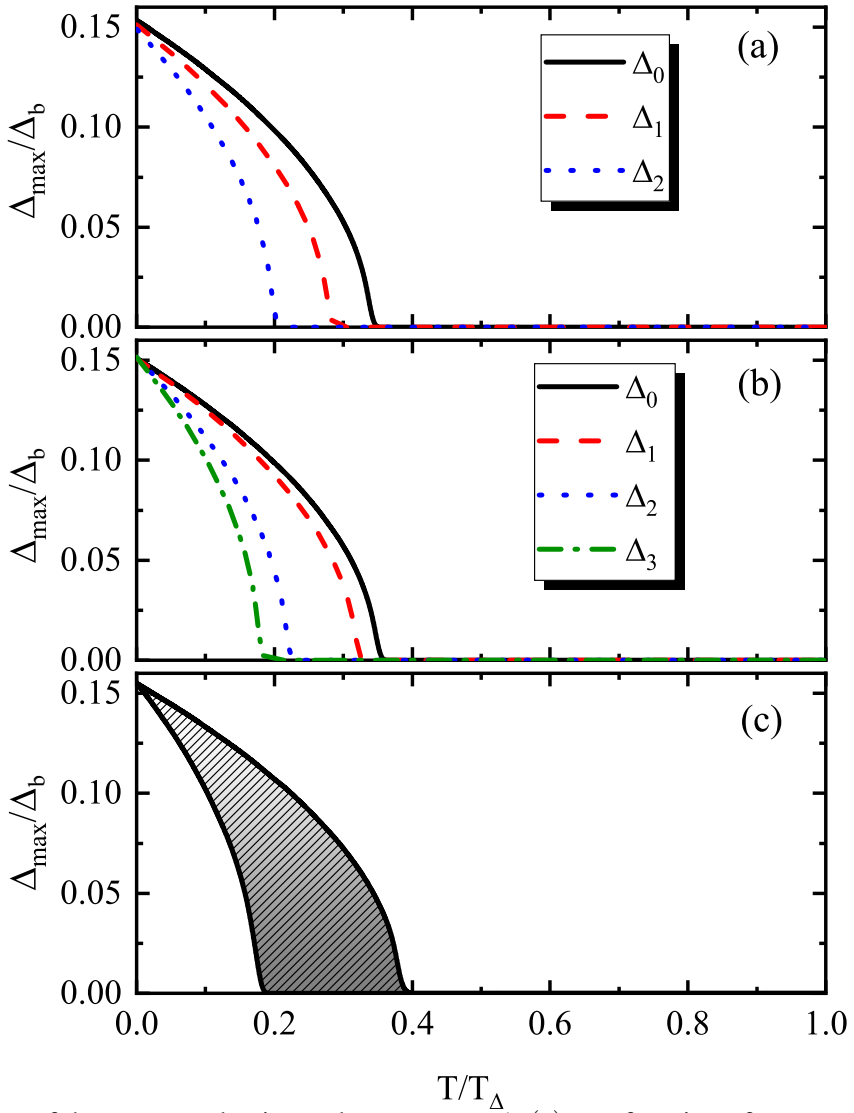

Maximum values of the superconducting order parameter $\Delta_n(x)$ as a function of temperature, for the first (a) three eigenstates of a three-interfaces system, and (b) four eigenstates of a four-interfaces system. (c) The same as (a,b), but for an infinite superlattice of equally spaced parallel interfaces. In all cases, interfaces are separated by $d = 3.5\ \xi_{\mathbf{w}}$, assuming weak suppression $a_0 = 1$.

eigenvalues are.

$$\varepsilon_n = \varepsilon_0 - 2\tau(d)\cos\left(\frac{n\pi}{N+1}\right). \tag{5.16}$$

It is easy to see that the results for $N = 2-4$ are special cases of this general expression. As N approaches infinity, an infinite number of states form a band of eigenvalues

$$\varepsilon(k) = \varepsilon_0 - 2\tau(d)\cos(kd), \tag{5.17}$$

limited to the range $[\varepsilon_0 - 2\tau, \varepsilon_0 + 2\tau]$. As a result, there will be a range of critical temperatures such that, as the system cools down, a series of SC eigenstates at the interfaces become ener-

getically favorable one after the other, for temperatures within this range. This is illustrated by the shaded area in Fig. 19(c). Importantly, the upper limit of this range of critical temperatures is determined by the strength of the interface coupling, τ, which depends on factors such as the separation between the interfaces.

This can be seen as a way to effectively increase the critical temperature of interface superconductivity in a system with many parallel interfaces, as we will discuss further. It is worth noting that these critical temperatures are higher than those expected for a single interface or for multiple non-coupled interfaces (i.e. far apart from each other), although they are still lower than the critical temperature expected for the same order parameter in the bulk case.

5.3 Superconducting states as a function of temperature - The complete solution

The solutions derived from our linearized Ginzburg-Landau (GL) analysis highlight an intriguing interaction of superconductivity across the interfaces. Specifically, when there are multiple interfaces, there is a critical temperature for the degeneracy of different superconducting eigenstates. This degeneracy is lifted as the interfaces are brought closer together. However, these solutions do not provide a full resolution of the GL equation. Instead, they serve as a foundation that can be used to express the full solutions. For instance, if there are only two interfaces, the full solution can be represented as a linear combination of Δ_0 and Δ_1 eigenstates. It is crucial to examine the impact of these eigenstates on the overall solution, which requires solving the coupled set of equations, Eq. (5.5) and Eq. (5.6), self-consistently using the relaxation method.

We start with the simplest scenario of two interfaces. The complete solution in this case must either be symmetrical, anti-symmetrical, or a combination of the two, as shown in Fig. 15(b). However, Fig. 16 indicates that the symmetrical and anti-symmetrical eigenstates have different critical temperatures, depending on the separation distance d, with Δ_0 always having a higher critical temperature. Fig. 20 shows the reduced temperature T/T_Δ at which the superconducting (SC) order parameter Δ first appears from zero. In the model, if the sample is entirely superconducting, this reduced temperature would be $T/T_\Delta = 1$. But, instead, the sample is in the collective state, which competes with and suppresses superconductivity throughout the system. The suppression of the other collective OP at the interfaces leads to superconductivity, and it occurs at temperatures that are only a fraction of the critical temperature T_Δ.

As seen in Fig. 20(a), interfaces separated by $d = 6\ \xi_w$ become superconducting at $T \approx 0.09T_\Delta$. The effective critical temperature decreases further to $T \approx 0.058T_\Delta$ and $\approx$

Figure 20 – Color maps of the Cooper pairs density Δ

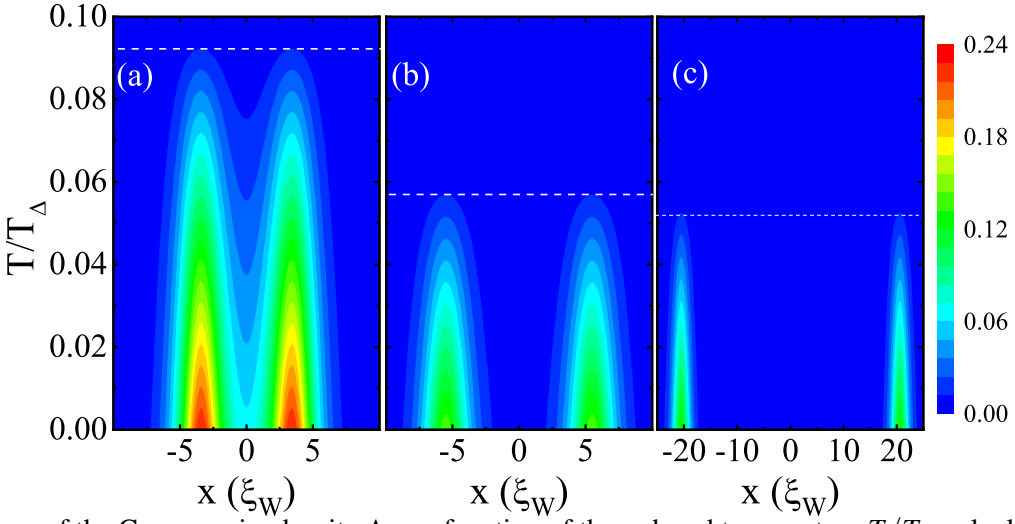

Color maps of the Cooper pairs density Δ as a function of the reduced temperature T/T_Δ, calculated by the self-consistent solution of Eqs. (5.5) and (5.6), for two interfaces separated by (a) $d = 6\ \xi_w$, (b) $12\ \xi_w$ and (c) $40\ \xi_w$. For shorter separations, the SC order parameter in the interfaces is enhanced and the effective critical temperature, marked by the horizontal dashed lines, increases, from the predictions of the linearized GL formalism.

$0.052T_\Delta$ for larger separations $d = 12\ \xi_w$ and $40\ \xi_w$ in Figs. 20(b) and 20(c), respectively. This dependence of the effective SC critical temperature on the separation d is expected based on the results of the linearized equations. As the interfaces get closer, the critical temperature of the symmetrical eigenstate Δ_0, which is the highest one, increases. This demonstrates the potential for enhancing the SC critical temperature by creating superlattices with interfaces stacked closer together or by increasing the number of stacked interfaces, since the critical temperature of the eigenstate Δ_0 also increases with N – as confirmed in Fig. 19.

At lower temperatures, the critical temperature of the anti-symmetric eigenstate Δ_1 is reached, enabling it to serve as a potential basis for the SC order parameter. With both eigenstates attainable, solutions in the form $\Delta = a_0\Delta_0 + a_1\Delta_1$ become possible. For example, a combination with $a_0 = a_1$ results in superconductivity only occurring in one interface, as depicted in Fig. 21(a), where this solution is shown to be metastable up to $T/T_\Delta \approx 0.01$. However, at zero temperature, this single-interface superconducting state is only stable if the interfaces are far apart (beyond $35\ \xi_w$ in this scenario) so that the energies of either symmetric, anti-symmetric, or a combination of the two eigenstates are equivalent. But as the interfaces come closer, the single-interface SC state becomes unstable, as seen in Fig. 21(b). This is a result of Cooper pairs tunneling through the W region separating the interfaces, leading to superconductivity in both interfaces if one is superconducting.

The tight-binding model described in the last section predicts that the critical tem-

Figure 21 – Color map of the Cooper-pair density in two parallel interfaces

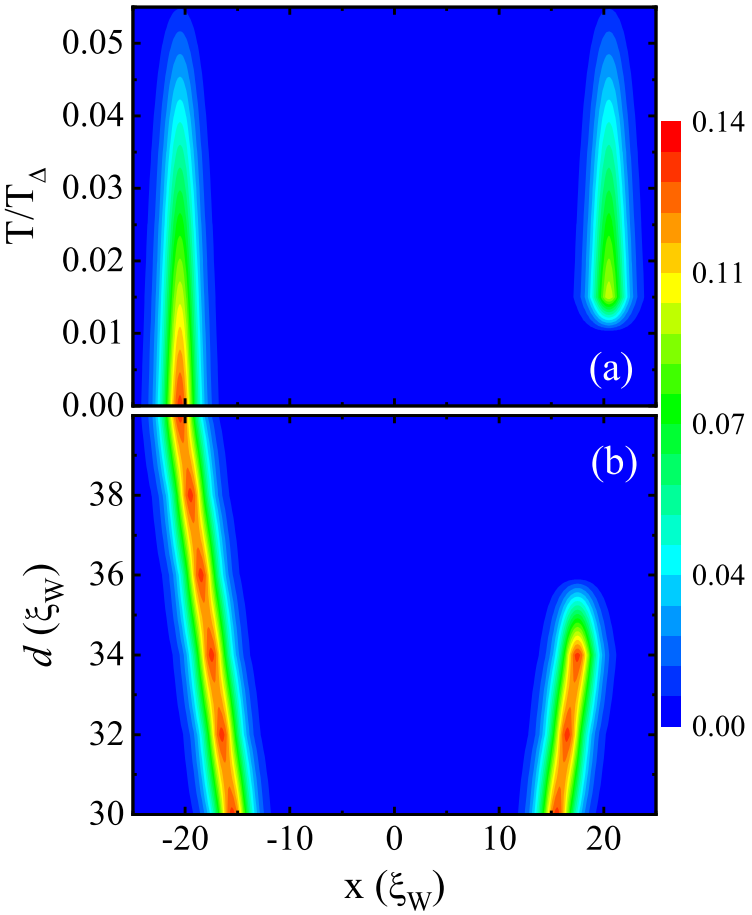

Color map of the Cooper-pair density in two parallel interfaces, obtained by solving the full nonlinear GL set of equations, as a function of (a) temperature, for a fixed interface separation distance $d = 40\ \xi_w$, and (b) as a function of d, for a fixed temperature $T = 0$. The metastable solution where SC is active only in one of the interfaces (left) is obtained only for larger separation between the interfaces and is expected to be experimentally achieved after a rapid quench to low temperatures.

perature of interface superconductivity increases with the number of stacked interfaces. This is demonstrated in Figure 22 which shows three potential states for a system of $N = 10$ interfaces.

The state displayed in Figure 22(a), obtained from relaxing a randomly generated initial trial function, shows all interfaces with superconductivity at low temperatures, with slightly higher Cooper-pair densities in the inner interfaces than in the outer ones. As the temperature rises, superconductivity in the peripheral interfaces is suppressed first. On the other hand, Figures 22(b) and 22(c) shows stable states where superconductivity is completely suppressed in some of the inner interfaces. As the temperature decreases, the critical temperatures of different superconducting eigenstates are reached, allowing several combinations of eigen-

Figure 22 – Color map of the Cooper-pair density in 10 parallel interfaces

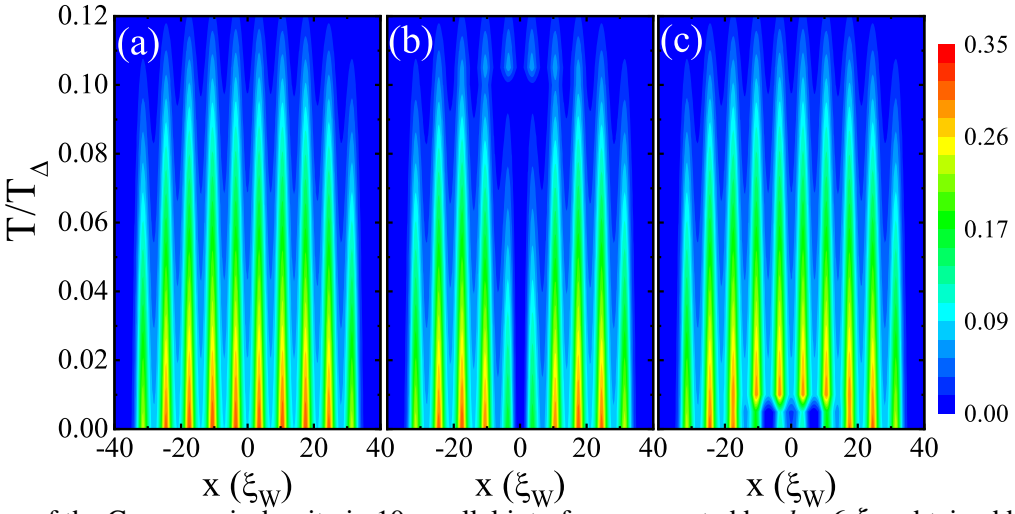

Color map of the Cooper-pair density in 10 parallel interfaces separated by $d = 6\ \xi_w$, obtained by solving the full nonlinear GL set of equations as a function of temperature. Panels (a)-(c) exemplify three different metastable states at low temperatures, obtained after initialization from many different initial conditions (simulating nucleation from the normal state).

functions with varying numbers of spatial nodes and phase shifts. At low temperatures, there may be stable solutions with suppressed Cooper-pair density in one or more interfaces, similar to what is shown in Figure 21(a) for $N = 2$. These are metastable states, but they are higher in energy than the state shown in Figure 22(a) and therefore less likely to be obtained from different initial conditions. However, they may still be relevant for experimental observation, particularly in the field-cooled regime where the system is rapidly cooled to low temperatures from the normal state.

The composition of the superconducting states in Figs. 22(b) and 22(c) is presented in the top and bottom panels of Fig. 23. It is important to note that the state in Fig. 22(a) consists only of the ground eigenstate Δ_0 at all temperatures and thus, it is not shown in Fig. 23. On the other hand, the state in Fig. 22(b) is a combination of eigenstates with odd indices until $T = 0.1T_\Delta$, where Δ_0 becomes dominant and the final state resembles that of Fig. 22(a) at higher temperatures. The contribution of the eigenstates with higher eigenvalues (lower critical temperature) decreases, especially at higher temperatures. Fig. 22(c), which shows strong suppression of SC in the inner interfaces up to $T = 0.01T_\Delta$, is composed of the eigenstates with even indices as shown in the bottom panel of Fig. 23.

The suppression of superconductivity in specific interfaces, as shown in Figs. 21 and 22, is a type of latent superconductivity. In these states, the system is below the critical temperature for superconductivity, but there are no competing order parameters present in the affected interfaces. The combination of specific eigenstates, which can have opposing phases,

Figure 23 – Projections of the Cooper-pair densities

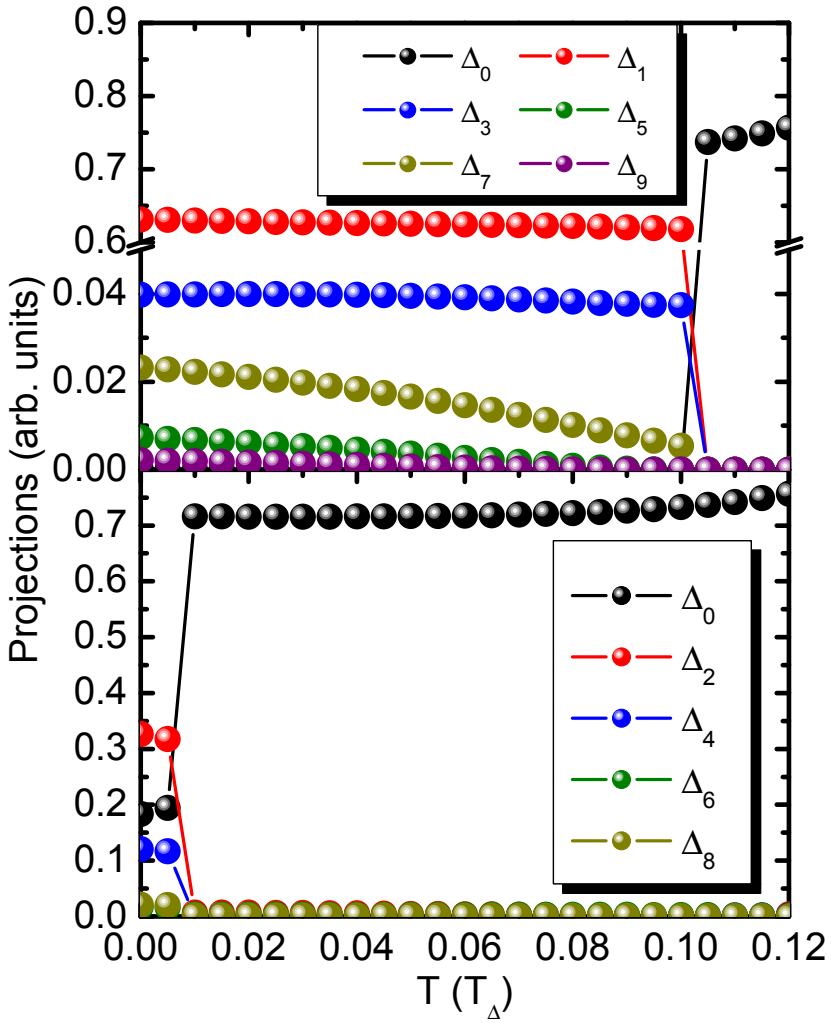

Projections of the Cooper-pair densities shown in Fig. 22(b) (top panel) and Fig. 22(c) (bottom panel) on the eigenstates Δ_n of a system with ten stacked interfaces.

can result in a partial cancellation of the superconducting order parameter in some interfaces. However, it is important to note that these exotic, metastable states are not easily attainable through slow cooling but rather require a rapid quenching of the temperature below the critical temperature of the exotic state. Such a rapid cooling process would allow the system to reach one of these metastable states at low temperatures. Subsequently, warming the system slowly would provide insight into the behavior of the order parameter distribution as seen in Figs. 21 and 22.

6 SINGULARITIES AND DISCOMMENSURATIONS IN CHARGE DENSITY WAVE STATES OF TRANSITION METAL DICHALCOGENIDES

The relationship between collective phases and their competition is a central discussion in solid-state physics[67, 75–83]. With the discovery of high-temperature superconductivity, researchers have been studying the interplay between superconductivity and other collective phenomena such as nematic order[76, 77, 84], anti-ferromagnetism[69], and charge/spin density waves in these materials. Transition-metal dichalcogenides (TMDs) exhibit superconductivity when doped in the form of a dome in the temperature-doping phase diagram of the material.

It is believed that the fluctuations of the TMDs' charge density wave (CDW) order, play a role in enhancing the superconducting critical temperature[57, 85, 86]. In chapter 4 shows the study of A. Pasztor *et al.* in their study [43] utilized the scanning tunneling microscopy (STM) technique to obtain high-resolution images of the charge density wave (CDW) phase in VSe_2 and $NbSe_2$. This novel method allows the extraction of the amplitude and phase maps of the different components of the CDW pattern. The results showed that the CDW in these transition-metal dichalcogenides (TMDs) consists of three separate charge modulation order parameters. The phase images revealed not only discommensurations, which had been predicted by McMillan theory [23], but also topological defects and domain walls in the nearly-commensurate state.

Recently, the McMillan-Ginzburg-Landau model (MGL) was employed to explain the transformation from incommensurate to commensurate CDW phases in TMDs [57]. This study revealed the presence of discommensurations in the near-commensurate phase and proposed a connection between the CDW and SC phases by way of a modulation of the quadratic term of the SC order parameter in the Ginzburg-Landau energy functional, which is proportional to the gradient of the CDW order parameter. This approach allowed for the modeling of the SC dome in the near-commensurate region of the TMD phase diagram, as the SC phase appeared in areas with high variations in the CDW order parameters, such as in the discommensurations.

In Chapter 5, we have shown the relation between the SC and another collective state. However, a more in-depth analysis is necessary to better understand the different parameters involved in the MGL model and to examine the impact of the experimentally observed phase domain walls and topological defects on the CDW profile, to accurately predict and control the shape of the SC dome in the phase diagram of different TMD-based systems.

6.1 Theoretical Model

Recalling the equations for TMDs of chapter 4 we have the density modulation of the C-CDW, Eq. (4.2), and the MGL energy functional for TMDs is given by the sum of Eqs. (4.4) and (4.8). The former equation gives the energy for the formation of the CDW phase, while the latter accounts for the TMDs symmetries.

The SC energy can be included in the full energy functional for the TMDs

$$f = f_{\mathrm{MGL}} + f_s + \gamma \sum_j |\psi_j|^2 |\Phi|^2, \tag{6.1}$$

where f_s is the standard GL functional without a magnetic field

$$f_s = a_s |\Phi|^2 + \frac{b_s}{2} |\Phi|^4 + \frac{1}{2m^*} \left| \frac{\hbar}{i} \nabla \Phi \right|^2 \tag{6.2}$$

The method we use for coupling CDW profiles and SC via a bi-quadratic term $\gamma \sum_j |\psi_j|^2 |\Phi|^2$, is the same as in the previous chapter. Notice the same rationality from the previous chapter applies to this case. The CDW is well settled when superconductivity arises, this way, we can neglect the influence of the SC OP on the CDW.

Three Euler-Lagrange equations, one for each j-direction, are used to minimize the energy in the MGL functional and using an effective mass term m^* to re-write $B = \frac{\hbar^2}{2m^*}$ we get a better physical insight:

$$\left[\alpha\tau + G|\psi_j|^2 + \frac{K}{2}\left(|\psi_l|^2 + |\psi_k|^2\right) \right] \psi_j - E\psi_j^\dagger - \frac{\hbar^2}{2m^*}(i\nabla + \mathbf{q}_j^I)^2 \psi_j + \frac{3D}{2}(\psi_l^\dagger \psi_k^\dagger) + \frac{M}{2}(\psi_l \psi_k + 2\mathbb{R}[\psi_l \psi_k]) = 0, \tag{6.3}$$

where $l \neq k \neq j$. Defining a characteristic length $\xi = \sqrt{\hbar^2 / 2m^* \alpha}$ and re-scale energies by α. Equation 6.3 become

$$\left[\tau + \frac{G}{\alpha}|\psi_j|^2 + \frac{K}{2\alpha}\left(|\psi_l|^2 + |\psi_k|^2\right) \right] \psi_j - \frac{E}{\alpha}\psi^\dagger - \xi^2 (i\nabla + \mathbf{q}_j^I)^2 \psi_j + \frac{3D}{2\alpha}(\psi_l^\dagger \psi_k^\dagger) - \frac{M}{2\alpha}(\psi_l \psi_k + 2[\psi_l \psi_k]) = 0. \tag{6.4}$$

For the SC, the Euler-Lagrange equation that minimizes f_s is simply the GL equation, coupled to the CDW parameter by γ[87]

$$\left(a_s + b_s|\Phi|^2\right)|\Phi - \frac{1}{2m^*}\left(\frac{\hbar}{i}\nabla\right)^2 \Phi + \gamma\Phi \sum_k |\psi_k|^2 = 0 \tag{6.5}$$

Both Equations (6.4) and (6.5) are solved by numerical methods. The SC equation can be solved by the relaxation method, the same way as in the last chapter. For CDW equations Eqs. (6.4) can be solved by using the imaginary time evolution technique, which has proven to be effective in similar mathematical cases such as the Gross-Pitaevskii equation in Bose-Einstein condensation[88–90].

6.2 Imaginary time evolution technique

The split-operator technique[91], a numerical method for time evolution, is utilized to carry out the process, where the initial wavefunctions $\psi_j(x,y,t=0)$ are evolved to solve the set of coupled equations. This technique involves dividing the time evolution operator, as described in [92].

$$e^{-\frac{i}{\hbar}\int_t^{t+\Delta t} f_M(t)dt} \approx e^{-\frac{i}{2\hbar}\hat{V}\Delta_t} e^{-\frac{i}{2\hbar}\hat{T}\Delta_t} e^{-\frac{i}{2\hbar}\hat{V}\Delta_t} + O(\Delta t^3), \tag{6.6}$$

where the $O(\Delta t^3)$ error accounts for the non-commutativity between the $\hat{V}$ and $\hat{T}$ operators, which are defined as

$$\hat{V} = \left[\tau + \bar{G}\left|\psi_j\right|^2 + \frac{\bar{K}}{2}\left(|\psi_l|^2 + |\psi_k|^2\right)\right] - \bar{E}\frac{\psi_j^*}{\psi_j} + \frac{3\bar{D}}{2\psi_j}(\psi_l^*\psi_k^*) - \frac{\bar{M}}{2\psi_j}(\psi_l\psi_k + 2\mathbb{R}[\psi_l\psi_k]) \tag{6.7}$$

and

$$\hat{T} = -\left(i\nabla + \mathbf{q}_j^I\right)^2 \tag{6.8}$$

In the model, the parameters $\bar{E},\bar{G},\bar{K},\bar{D}$, and $\bar{M}$ are expressed in units of α, while lengths are measured in units of ξ. As the initial order parameters $\psi_j(x,y,t=0)$ evolve in the imaginary time $T_i = it$, they will eventually reach the profiles that minimize the McMillan energy functional. It should be noted that the $\hat{V}$ term in Eq. (6.7) depends on ψ_j and therefore, it changes with time. This would require a time integral in the terms in Eq. (6.6) that are dependent on $\hat{V}$. To overcome this issue, we approximate $\hat{V}$ to be approximately constant within the interval $[t,t+\Delta t]$, provided that Δt is small enough to produce a converged energy result with an error of less than 1

In some cases that we will discuss further, we will need to use a vector field $\mathbf{q}_j^I(x,y)$ as the incommensurability wave-vector instead of a constant wave-vector. This can create difficulties for the application of the exponential of the $\hat{T}$ term in Eq. (6.6), which now includes both derivative operators and functions. However, this challenge is addressed by the gauge-invariant

finite difference method presented in Ref. [93].

6.3 Results and discussion

In this section, the parameters $G = K = 2\alpha$, $M = \alpha$, and $D = -\alpha$ are selected, following the choice made in Ref. [57], unless specified otherwise. This allows us to make comparisons with previous studies while also enabling us to modify the parameters individually to see how they impact the results.

6.3.1 Physical insights from a phase-only approximation

The CDW order parameters can be written in terms of their amplitude and phase, Equation 4.6. In terms of the amplitude and phase of each order parameter, the McMillan energy functional is re-written as

$$\begin{aligned} F_{\text{cdw}} = \sum_{j=1,2,3} \big\{ \tau\phi_j^2 + G\phi_j^4 + \xi^2[(\mathbf{q}_j^I - \nabla\theta_j)^2\phi_j^2 + (\nabla\phi_j)^2] \\ -E\phi_j^2\cos(2\theta_j)\big\} - \phi_1\phi_2\phi_3[3D\cos(\Theta) + M\sum_{j=1,2,3}\cos(\Theta_j)] + \\ \frac{K}{2}\sum_{i\neq j}\phi_i^2\phi_j^2 \end{aligned} \tag{6.9}$$

where $\Theta = \theta_1 + \theta_2 + \theta_3$ and $\Theta_j = \theta_j - \theta_{j+1} - \theta_{j+2}$.

From the McMillan energy functional, it becomes evident that in a phase-only model, meaning for constant ϕ_j, without any coupling term and for $E = 0$, the energy minimum is achieved when

$$\nabla\theta_j = \mathbf{q}_j^I. \tag{6.10}$$

This implies that as E approaches 0, the solution must tend towards the incommensurate case, where $\theta_j = \mathbf{q}_j^I \cdot \mathbf{r}$ and thus, the phase adds a $\mathbf{q}_j^I$ correction to the CDW wave-vector $\mathbf{Q}_j^C$.

The Euler-Lagrange equations for θ_j that minimize F_{cdw} reads

$$\begin{aligned} \phi_j\nabla^2\theta_j + 2\nabla\phi_j\nabla\theta_j - 2\mathbf{q}_j^I\cdot\nabla\phi_j - \frac{E}{\xi^2}\phi_j\sin(2\theta_j) - \frac{3D}{2\xi^2}\phi_{j+1}\phi_{j+2}\sin(\Theta) \\ -\frac{M}{2\xi^2}\phi_{j+1}\phi_{j+2}[\sin(\Theta_j) - \sin(\Theta_{j+1}) - \sin(\Theta_{j+2})] = 0 \end{aligned} \tag{6.11}$$

In this equation, the incommensurate phase $\theta_j = \mathbf{q}_j^I \cdot \mathbf{r}$ is still the solution of this equation for $E = 0$ even at a non-constant ϕ_j and non-zero coupling D, since the term involving the latter is zero, as $\Theta = (\mathbf{q}_1^I + \mathbf{q}_2^I + \mathbf{q}_3^I)\cdot\mathbf{r} = 0$ in this case. On the other hand, a non-zero coupling constant M does not guarantee the incommensurate solution as the lowest energy state

in the system. Therefore, increasing the coupling constant M may harness the ability to control the transitions between commensurate, near-commensurate, and incommensurate phases of the CDW only through the parameter E.

Furthermore, in the phase-only model in the absence of couplings and for non-zero E, Eq. (6.11) reduces to

$$\nabla^2\theta_j - \frac{E}{\xi^2}\sin(2\theta_j) = 0, \tag{6.12}$$

which is easily identified as the sine-Gordon equation, whose solution takes the form of a soliton. This suggests that increasing E leads to soliton-like solutions for the phase, which would perfectly mimic the experimentally observed discommensurations in CDW. Since the stationary soliton solution has the general form

$$\theta_j(x_j) \propto \tan^{-1}\{\exp[\sqrt{E}(x_j - x_{j0})/\xi]\}, \tag{6.13}$$

where x_j is the coordinate along the j-th direction and x_{j0} is an offset for the soliton position, the sharpness of the soliton steps are controllable by either E or ξ, which are related to the total charge density and the deviation parameter δ_j, respectively. The analysis of these limits in our model suggests that in the absence of couplings:

1. $E \to 0$ leads to the incommensurate solution,

2. moderate values of E lead to a combination between an incommensurate phase and soliton-like phase-slips, which can be seen as discommensurations,

3. $E \to \infty$ leads to an infinitely long soliton-like step, which is eventually interpreted as the commensurate phase.

It is important to check how the presence of couplings K, D, and M between the different CDW order parameters change this scenario.

The prediction that $\nabla\theta_j$ must converge to $\mathbf{q}_j^I$ in order to minimize the energy can be used as a convenient way to modify the MGL model as to produce different defects in CDW. For instance, consider a domain wall perpendicular to a given direction $\mathbf{G}_j$, at $x_j = 0$, separating regions where the phase is constant.[43, 94] The associated phase θ_j can be mathematically described as a kink function $\theta_j = h_i \tanh(x_j/a_i)$, where a_i and h_i controls the width of the interface region and its height, respectively. Such a phase distribution is readily obtained from

the imaginary time evolution by defining an effective incommensurability vector field

$$\mathbf{q}_j^I(x_j) = \frac{h_i}{a_i} sech^2\left(\frac{x_j}{a_i}\right)\hat{x}_j \tag{6.14}$$

such that $\nabla\theta_j = \mathbf{q}_j^I(x)$ yields the expected kink profile for θ_j. As another example of the application of this concept, a vortex-antivortex pair along the x-axis in θ_j is obtained by an incommensurability vector field[19]

$$\mathbf{q}_j^I(x,y) = \left(\frac{-y}{r_v^2} + \frac{y}{r_{av}^2}\right)\hat{x} + \left(\frac{x-\frac{d_{vav}}{2}}{r_v^2} - \frac{x+\frac{d_{vav}}{2}}{r_{av}^2}\right)\hat{y} \tag{6.15}$$

where $r_v = \sqrt{(x-d_{vav}/2)^2+y^2}$, $r_{av} = \sqrt{(x+d_{vav}/2)^2+y^2}$, and d_{vav} is the vortex-antivortex separation. The profiles of the order parameters obtained from the MGL theory with constant $\mathbf{q}_j^I$, as well as with vector fields defined by Eqs. (6.14) and (6.15), are discussed in what follows.

6.3.2 Discommensurations revisited

In this discussion, we first consider the scenario of constant $\delta_j\mathbf{Q}_j^C$, which results in discommensurations. To simplify, let's assume the same δ_j for all three directions ($j = 1-3$). Figure 24(a) displays the phase distribution along the reciprocal lattice direction $j = 1$, for various values of the energy parameter E, with $\delta_j = 0.1$. The results and conclusions for the other directions $j = 2$ and 3 are identical to those for $j = 1$, so they are omitted. For $E = 0$, the phase is simply $\theta_1(x_1) = q_1^I x_1$, meaning the system is in a perfectly incommensurate phase, with the effective wave-vector of the CDW in this direction being

$$Q_1^C(1+\delta_1) = 1.1Q_1^C. \tag{6.16}$$

As E increases, the soliton-like steps predicted in the previous section are observed, creating regions where the system is locally commensurate, separated by phase slips, or discommensurations. At higher values of E, the soliton steps become so long that the phase is virtually constant, leading to the effective wave-vector of the CDW being Q_1^C, which results in the commensurate phase.

By taking the derivative of θ_1 and calculating the height and distance between the resulting peaks, one can estimate the steepness of the discommensurations and the length of the steps produced by them, respectively. The former is represented by red line-squares, and the latter by black lines, in Figure 24(b) as a function of the lock-in energy E. Lengths are expressed in units of the lattice parameter a_L. Since the length of discommensurations steps can be effec-

Figure 24 – Phase of CDW order parameter versus lock-in energy

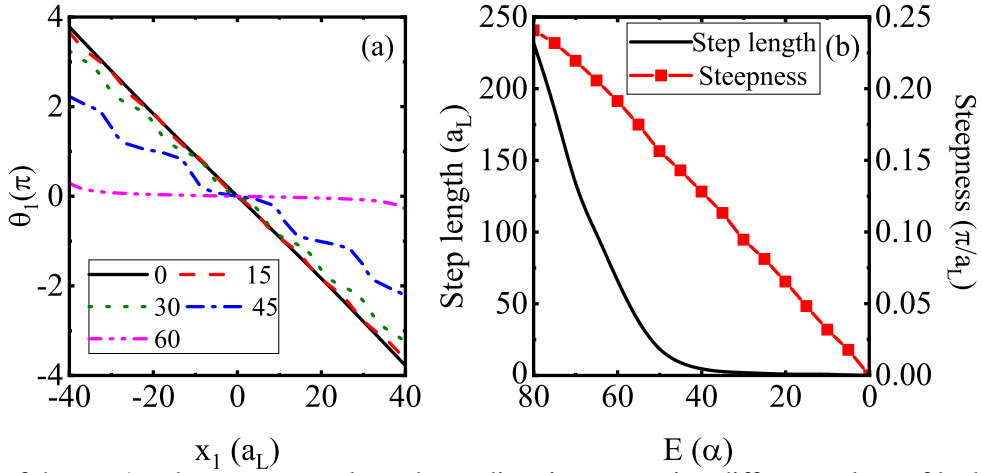

(a) Phase of the $j = 1$ order parameter along the x_1 direction, assuming different values of lock-in energy $E = 0$, 15, 30, 45, and 60 α. (b) Length of the discommensuration steps (black line, left axis), along with the discommensuration steepness (red line-symbols, right axis), as a function of the lock in energy E. The lock-in energy axis is reversed to help visualization since the actual experimentally controllable parameter is the overall charge density, which is inversely proportional to E.

tively measured by current experimental techniques (such as in Ref. [43]), the results presented here enable us to estimate some of the parameters needed for a proper theoretical description of a CDW phase in a given TMD. As the lock-in energy increases (i.e., the overall charge density decreases), the length of the discommensuration steps rapidly increases, eventually leading to the commensurate phase.

Figure 25 – Phase of CDW order parameter versus M parameter

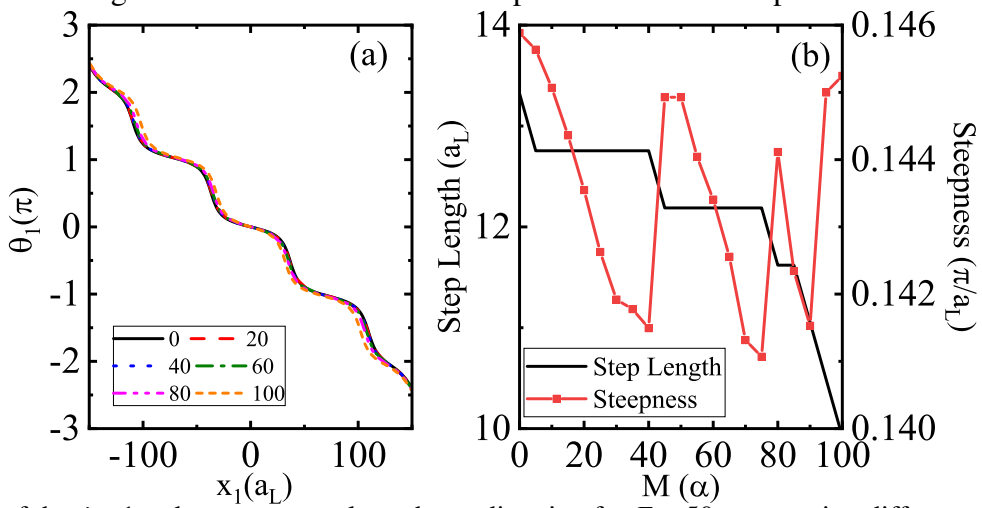

(a) Phase of the $j = 1$ order parameter along the x_1 direction for $E = 50\alpha$, assuming different values of the third order coupling energy $M = 0$, 20, 40, 60, 80 and 100 α.

Previously, it was stated that the coupling parameter M has a negative impact on the formation of discommensurations in the CDW phase profile. To evaluate the significance of this coupling, the effect of M on the length and height of the discommensuration steps is

shown in Fig. 25. As M increases, the step lengths decrease and the distance between the discommensurations becomes shorter, as shown in Fig. 25(a). A decrease of about 30% in step length is observed when M increases from 0 to 100α. On the other hand, the height of the steps is not significantly impacted, with oscillations of less than 3% of the average value, seen in Fig. 25(b), which are within the margin of error in our calculations.

The long and steep steps in the phase profiles observed in Fig. 24 become significantly smaller as one increases the incommensurability factor δ_j. This is illustrated in Fig. 26, where we consider $\delta_j = 0.15$. In this case, increasing E within the same range as in Fig. 24, the step length is still two orders of magnitude shorter than that observed in the $\delta_j = 0.1$ case, while the steepness is $\approx 30\%$ smaller.

Figure 26 – Phase of CDW order parameter versus lock-in energy for higher δ_j

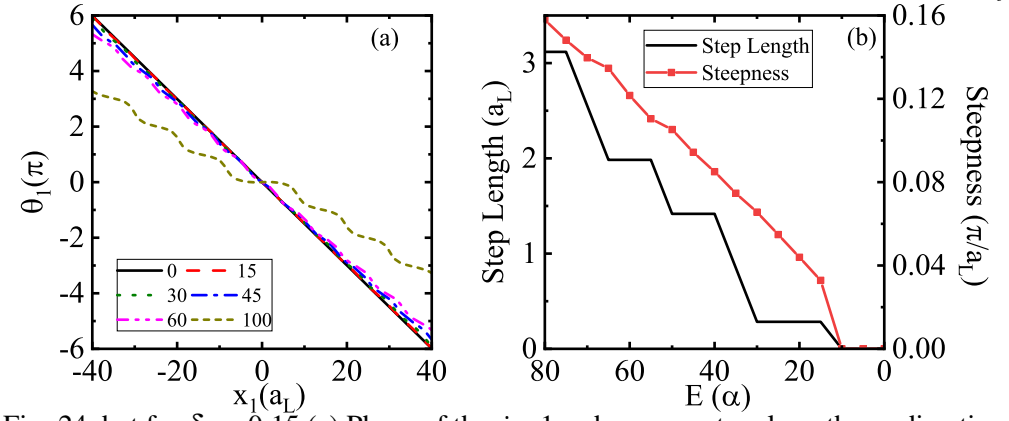

Same as Fig. 24, but for $\delta_j = 0.15$ (a) Phase of the j = 1 order parameter along the x_1 direction, assuming different values of lock-in energy $E = 0$, 15, 30, 45, 60 and 100 α. It needs a higher value of the lock-in energy to achieve the soliton solution (b) Length of the discommensuration steps (black line, left axis), along with the discommensurations steepness (red line-symbols, left axis), as a function of the lock-in energy E.

Increasing the lock-in energy E effectively increases the critical temperature of the CDW, as inferred by Eq. (6.11), where one sees that the temperature parameter $\tau = T/T_{cdw} - 1$, which multiplies ϕ_j^2, is effectively changed as $T/T_{cdw} - 1 - E\cos(2\theta_j)$. As E increases and the phase converges to $\theta_j \equiv 0$ as the lowest energy (commensurate) solution, higher temperatures are required to induce the normal/CDW phase transition. However, how fast θ_j converges to 0 depends on the different system parameters: higher discommensuration factors δ_j, for example, lead to a delayed convergence of θ_j to zero at significantly higher E. Therefore, the control of the CDW critical temperature is expected to depend e.g. on δ_j, which is confirmed by our numerical results in Fig. 27, which shows the effective critical temperature as a function of the lock in energy E for different values of δ_j. The delayed convergence of $\cos(2\theta_j)$ to 1 for higher δ_j eventually hinders the contribution of E to the effective critical temperature, thus making the

Figure 27 – Effective critical temperature as a function of the lock-in energy

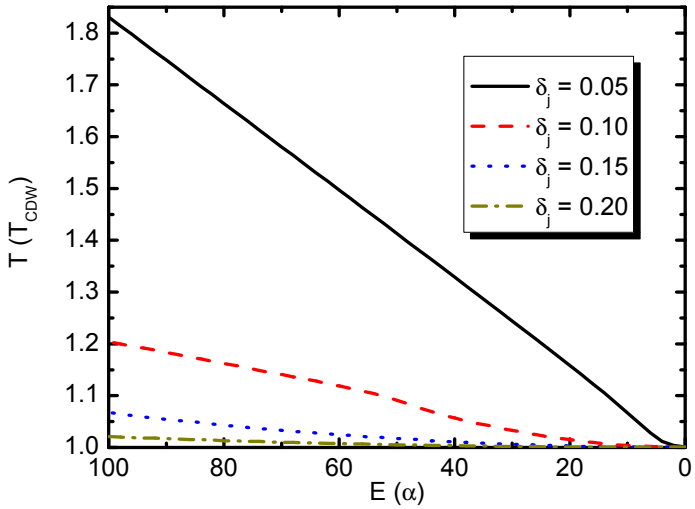

Effective critical temperature as a function of the lock in energy E for different values of the discommensuration parameter δ_j, which is considered the same for all three reciprocal vector directions $j = 1-3$.

control of the CDW critical temperature via E less efficient.

6.3.3 Phase domain walls and topological defects

Figure 28(a) shows a color map of a CDW profile, calculated with Eq. (4.2), in the presence of a phase domain wall. Such domain wall is obtained by defining the incommensurability vector fields $\mathbf{q}_1^I(x,y)$ and $\mathbf{q}_2^I(x,y)$ as in Eq. (6.14), which leads to the formation of identical domain walls in the order parameters ψ_1 and ψ_2, as observed in Ref. [43]. Indeed, the phase slips observed due to the domain wall leads to a CDW profile that qualitatively resembles those experimentally observed e.g. in Ref. [43, 94]. The amplitude (squared modulus) of the ψ_1 order parameter is shown as a solid line in Fig. 28(a) and exhibits a strong suppression in the interface. The $|\psi_2|^2$ profile is the same, therefore, it is omitted.

Figure 29 illustrates the phase and amplitude obtained from our calculations defining the incommensurability vector field $\mathbf{q}_1^I(x,y)$ as in Eq. (6.15), which yields the formation of a vortex-antivortex pair.

Either in the presence of the domain wall or vortex-antivortex pair defects, it is clear that along the line where the phase of the CDW order parameter changes abruptly, its amplitude drops to zero, thus enabling the emergence of a SC phase, as we will discuss later.

Figure 28 – Phase domain wall in CDW

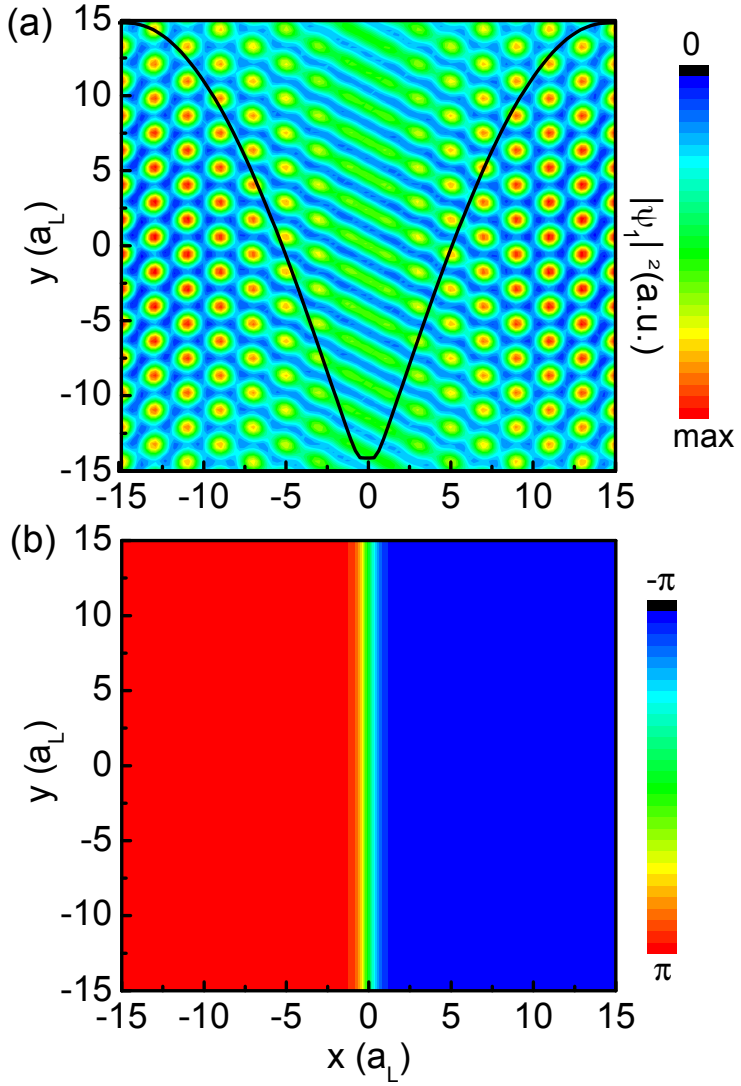

(a) Color map of the CDW profile in the presence of a phase domain wall in the order parameters ψ_1 and ψ_2, obtained by defining their incommensurability vector fields as in Eq. (6.14). The amplitude of the order parameter ψ_1 along the x-direction is superposed on the color map, for comparison. The amplitude of the order parameter ψ_2 is the same in this case. (b) Phase distribution of the CDW order parameter ψ_1.

6.3.4 CDW with broken rotational symmetry

Earlier experiments on $NbSe_2$ revealed the existence of a CDW phase characterized by a wave with a single direction, for instance, $\mathbf{Q}_3^C > 0$, with the effective wave vector being zero in the other directions, known as the uni-directional charge density wave phase (1q-CDW)[43].

In the model presented here, a similar phase can be obtained by considering an anisotropic form for the incommensurability vectors, Eq. (4.5), where two of the discommensuration parameters are set to -1, e.g. $\delta_1 = \delta_2 = -1$, while δ_3 is set to a small value, such as $\delta_3 = 0.1$, as an example. The numerical solution of Eq. (6.4) with this set of δ_j values is found to be unstable if the first-order coupling terms proportional to D and M are non-zero. As

Figure 29 – Vortex-antivortex pair in CDW

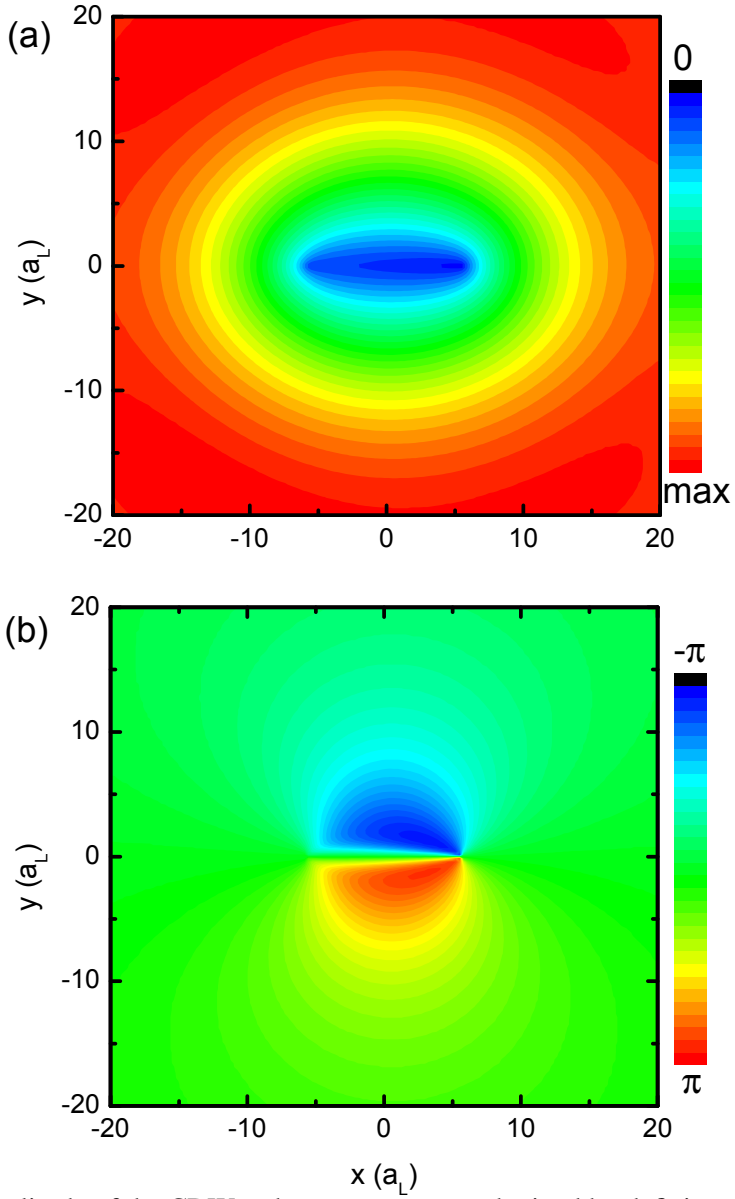

(a) Phase and (b) amplitude of the CDW order parameter ψ_1, obtained by defining the incommensurability vector field as in Eq. (6.15).

the one-directional phase is observed experimentally, this suggests a way to potentially rule out some coupling terms that, although allowed by symmetry[57], may not be significant in certain physical situations. Hence, results in this section are presented assuming $D = M = 0$.

Figure 30 shows the CDW profile with this set of parameters, which indeed leads to uni-directional CDW along the Q_3^C direction. In the case of low lock in energy $E = 100\alpha$, no defect is observed in the CDW periodicity, see Fig. 30(a). However, as this energy decreases to $E = 40\alpha$, our model predicts the occurrence of phase slips, due to discommensurations, in the CDW profile, see Fig. 30(b). For $E = 0$, we observe in Fig. 30(c) a perfectly periodic, although incommensurate, CDW profile. It is easy to verify that unidirectional CDW in the $j =$

1, 2 directions can be similarly obtained just by making $\delta_j \neq 0$ and $\delta_n = 1$ for $n \neq j$.

Figure 30 – CDW distribution $\rho(\mathbf{r})$ assuming an anisotropic set of incommensurability

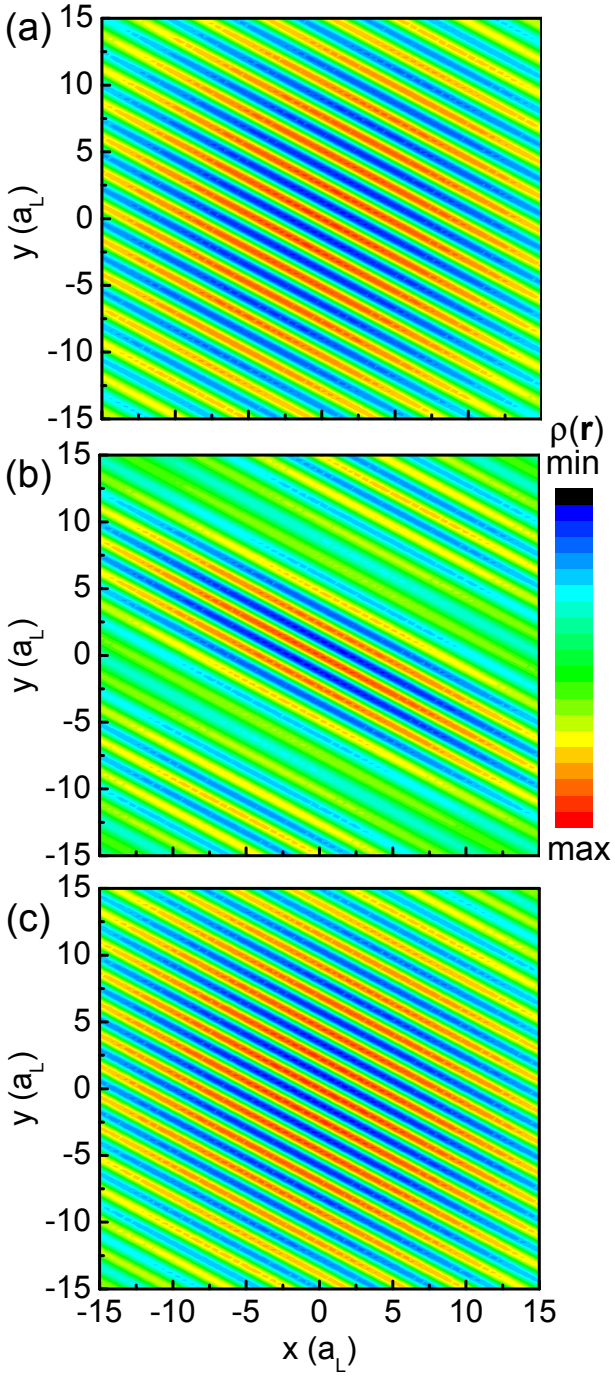

CDW distribution $\rho(\mathbf{r})$ assuming an anisotropic set of incommensurability vectors such that $\mathbf{q}_3^I = 0.1\mathbf{Q}_3^C$, $\mathbf{q}_2^I = \mathbf{Q}_3^C$ and $\mathbf{q}_1^I = \mathbf{Q}_1^C$, for $D = M = 0$, thus leading to an uni-directional charge density oscillation. Three values of lock-in energy are considered: (a) $E = 100\alpha$, (b) $E = 40\alpha$, and (c) $E = 0$.

Notice that the minima in the 1q-CDW profile $\rho(\mathbf{r})$ shown in Fig. 30 for $E = 0$ and $E = 100\alpha$ do not result from modulation of the amplitude of the order parameter, but rather from the oscillations originating from the exponential terms in Eq. (4.2). Therefore, the minima in these 1q-CDW cases are not expected to affect the SC phase, which couples to the

order parameters ψ_j, rather than to the total CDW profile ρ in the MGL model.

6.3.5 Effects on the emergent superconducting phase

In this section, we will explore the impact of the CDW defects, as outlined in the previous section, on superconductivity in a qualitative manner. Our model suggests that there is a competition between the superconducting order parameter Φ and the CDW order parameters ψ_j, which are linked through the γ parameter in equation (6.1). The superconducting phase is expected to develop in areas where the CDW order parameters are diminished. This approach resembles the hidden order parameter model discussed in references [72, 87]. In fact, the bi-quadratic coupling in equation 6.1 can be compared to the coupling presented in reference [57] by grouping all terms that multiply $|\psi_j|^2$. This results in an effective $\alpha_s^* = \alpha_s - \sum_j \gamma|\psi_j|^2$.

Based on the temperature dependence in GL theory [15], $\alpha_s(T) = \alpha_0(T/T_{SC} - 1)$, where T_{SC} is the reference superconductor critical temperature, the γ coupling decreases the critical temperature of the superconducting phase wherever $|\psi_j|^2$ is suppressed. For clarity, temperatures are scaled to T_{SC}. In the absence of CDW, the superconducting phase transition would occur at $T = T_{SC}$. However, high values of $|\psi_j|^2$ inhibit superconductivity and lower the effective superconductor critical temperature.

Figure 31 – Color map of the superconducting order parameter

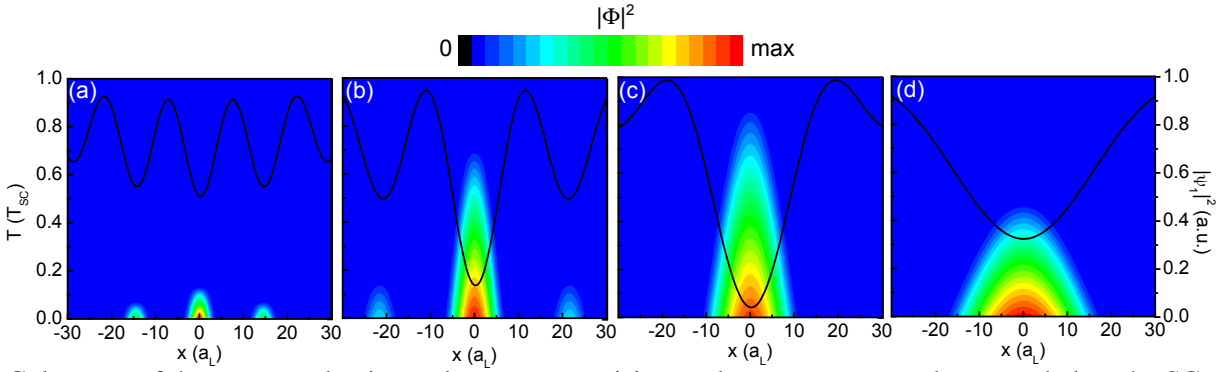

Color map of the superconducting order parameter rising as the temperature T decreases below the SC critical temperature T_{SC}, in the system where the CDW order parameter ψ_1 exhibits discommensurations along the x-direction, for lock-in energies E = (a) 40α, (b) 50α, (c) 60α, and (d) 70α, assuming a coupling parameter $\gamma = 4$. The profile of the CDW is superposed in each panel as a solid line.

In the following discussion on the rise of the superconducting order parameter in the interstitial spaces, for simplicity, we will assume two approximations: first, a *one dimensional* CDW. This allows us to easily qualitatively predict the behavior of the superconducting critical temperature dome in terms of the parameters of the CDW. A generalization of this discussion to the case of a combination of three CDW order parameters is straightforward. Second, we will

also neglect the influence of the SC order parameter on the CDW profile. This is a reasonable approximation since the CDW is already well settled in place when the critical temperature for the superconductivity phase is reached. This fact is supported by the phase diagram of several materials, e.g. cuprates and iron-pnictides[95–99]. The GL equation for the SC order parameter resulting from these approximations reads[87]

$$-\frac{1}{\xi_r^2}\frac{d^2\Phi}{dx^2}+\left[\frac{T}{T_{SC}}-\left(1-\frac{\gamma}{\xi_r^2}|\psi_1|^2\right)+|\Phi|^2\right]\Phi=0, \tag{6.17}$$

For example, we assume coherent lengths of CDW and SC order parameters with a $\xi_r = \xi/\xi_{SC}$ = 0.7 ratio.

The amplitude of the CDW order parameter exhibit dips at the discommensurations, whose depth is given by the steepness of the discommensuration. Within the model employed here, the effective superconducting critical temperature increases as the dips in the CDW are made deeper and closer[87]. Therefore, Fig. 24 allows us to predict that starting with low values of E, the discommensurations become steeper as E increases, thus increasing the superconducting critical temperature. On the other hand, for intermediate E, the discommensurations become too far from each other, decreasing the critical temperature again, until it goes back to zero at the commensurate phase, where discommensurations are no longer seen. This explains the emergence of a superconducting dome in the temperature versus charge density phase diagram.

Indeed, this behavior is verified in the color maps of the calculated SC order parameter along the x_1-axis as a function of temperature in Fig. 31. The profile of the CDW order parameter in the E = (a) 40α, (b) 50α, (c) 60α, and (d) 70α are shown as solid lines in each panel, for comparison. For $E = 60\alpha$, the dips in this order parameter are deep and close, leading to an SC order parameter that is active almost up to $T = T_{SC}$ for $\gamma = 4$, see Fig. 31(c). However, superconductivity in the center of the sample vanishes at lower effective critical temperatures as E is made either higher or lower than $E = 60\alpha$. For either $E < 40\alpha$ or $E > 90\alpha$, these dips are no longer able to sustain SC and the effective SC critical temperature drops to zero.

Figure 32 shows the SC dome delimited by the effective critical temperatures found as the temperature at which $|\Phi|^2$ drops to zero for each value of E. In the case where the discommensuration parameter is $\delta_1 = 0.10$ and the coupling between SC and CDW order parameters is high, the SC dome reaches values as high as 85% of the nominal SC critical temperature at $E = 40\alpha$, assuming $\gamma = 2.5$. Considering a lower coupling parameter, $\gamma = 2.0$, the SC dome

Figure 32 – Superconductor dome in TMDs

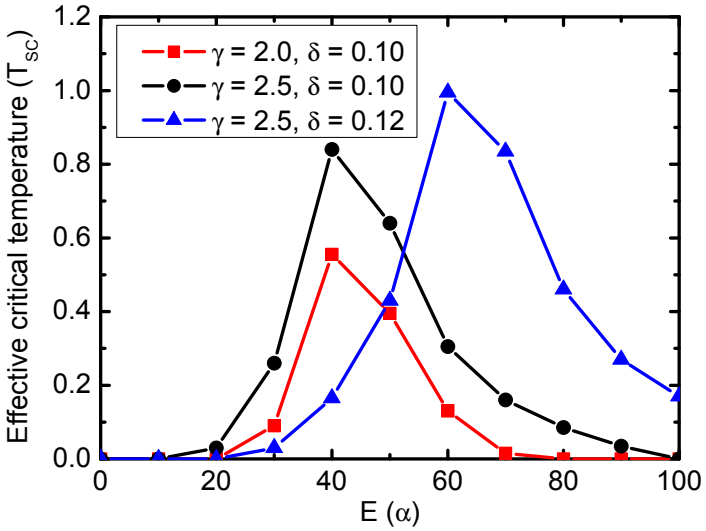

Dome delimited by the effective SC critical temperatures as a function of the lock in energy assuming γ = 3.5 (red) and 4 (black) for a $\delta_1 = 0.1$ discommensuration parameter, and $\gamma = 4$ for $\delta_1 = 0.15$ (blue).

becomes smaller. It is hard to predict the strength of the SC-CDW coupling with the phenomenological model proposed here for an actual sample, but the behavior of the SC dome for systems with different discommensuration lengths can be compared. In this case, our model predicts that for $\delta_1 = 0.12$, where discommensurations are shorter in space and more weakly affected by the lock in E (see Fig. 26), the SC dome becomes considerably higher and wider, as shown by the blue symbols in Fig. 32. Since the superconductivity is expected to emerge only at the discommensurations, superconducting lines would be further apart also in systems with high coupling M. Consequently, the superconducting dome is expected to exhibit lower critical temperatures in systems with high M as well.

SC is also expected to emerge within the dips in the CDW order parameter ψ_1 due to the defects. A color map of the SC order parameter profile in (a,b) vortex-antivortex defects as a function of temperature T is shown in Fig. 33, assuming coupling parameters $\gamma = 4$ (a) and $\gamma = 1$ (b). As in the previously discussed case where SC rises in the discommensurations, a higher γ coupling here also enhances the effective SC critical temperature. However, in this case, changing the lock in energy E does not affect either the depth or width of the minimum in ψ_1, therefore, although these defects are expected to enhance superconductivity in the sample, they are not expected to affect the profile of the SC dome in the temperature versus density phase diagram.

Figure 33 – Superconductivity in a CDW vortex-antivortex pair

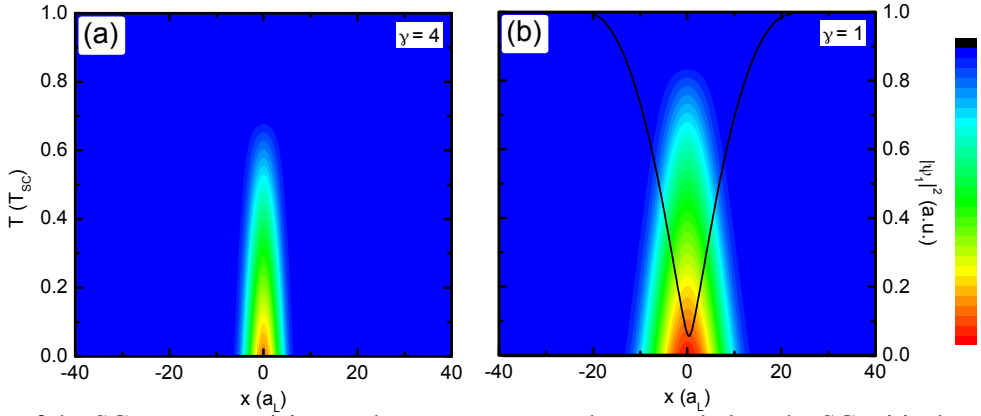

Color map of the SC parameter rising as the temperature T decreases below the SC critical temperature T_{SC}, in the system where the CDW order parameter ψ_1 exhibits a vortex-antivortex defect along the x-direction. Two values of the coupling parameter between SC and CDW are considered: (a) $\gamma = 4$ and (b) $\gamma = 1$. The profile of the amplitude of the CDW order parameter ψ_1 along the x-direction is shown in each panel, for comparison.

7 CONCLUSION

In this thesis, I studied two different problems involving collective phases and superconductivity that are closely related. First, interface superconductivity is modeled with a general approach to describe the interplay between one dominant collective state and superconductivity. The results of this model are then used to expand the theory of the formation of a superconducting dome in the temperature versus density phase diagram of TMDs, where a CDW state is dominant and a superconducting phase emerges among the defects in the CDW profile.

We have employed a two-component GL model to investigate properties of superconductivity arising in competition with another dominant (spin/charge density) order in a series of parallel interfaces. The model is developed on top of the one previously proposed in Ref. [72], where two competing order parameters exhibit density-density coupling but are easily extendable to other coupling forms stemming from a microscopic derivation. We go beyond this previous model by expanding its concept to the case of several parallel interfaces, where we demonstrate that as more interfaces are stacked together, the number of possible superconducting states across these interfaces increases, each with a different critical temperature. The critical temperature of the ground state, which would thus be the superconducting critical temperature of the system, depends on the distance between interfaces, the number of stacked interfaces, and, generally speaking, the coupling between adjacent interfaces. Bearing in mind the large number of systems where interface superconductivity is relevant, especially the artificially fabricated ones, our study conveniently indicates pathways towards control of critical temperature by nanoengineering of material superlattices.

Different (meta)stable superconducting states we found in the superlattice of interfaces are not only rich in number, but also in different physical manifestation, since some of them can host rather nontrivial spatial distribution of the Cooper-pair condensate, and even contain intrinsic π-Josephson junctions between parts of the superlattice. That suggests very rich possible behavior of the system in applied current and/or magnetic field, which is worth be explore further.

We also have demonstrated how an appropriate choice of parameters and functional forms of the MacMillan-Ginzburg-Landau energy functional can be used to describe not only

the formation of discommensurations in the CDW phase profiles but also the emergence of topological defects (vortex-antivortex pairs) and domain walls in the phase, as well as the appearance of a uni-directional CDW state. Revealing the mechanism behind the formation of these states, which have been observed in recent experiments, allowed us to investigate, within a phenomenological model, how modifications on the phase step lengths and heights and on the vortex-antivortex separation affect the profile of the CDW order parameters.

Since this order parameter is known to compete with an emergent SC order parameter in these systems, we have also used our model to elucidate the mechanism behind the emergence of the SC dome in their phase diagrams. Much like the previously discussed general model of hidden SC order parameter, we demonstrate that the SC state rises in defects of the pure C-CDW (or IC-CDW), like DC, vortex-antivortex, and domain walls. We also showed that the SC critical temperature depends on the distance and depth of the modulations in the CDW order parameter, which allows us to design systems where this critical temperature is effectively enhanced.

In this thesis, we introduce a powerful theoretical and numerical model that can handle non-uniform cases, like the domain wall and vortex-antivortex which opens multiple interesting paths to study. With this framework, we can explore the phase diagrams of the CDW, by modifying the multiple parameters present. Or apply magnetic and electric fields to understand the response of the CDW and how affect the rise of superconductivity. We showed the superconductivity rising in the defects of the CDW, another point that can be explored is if the regions in between the defects can function as Josephson junctions. In the interfaces, we saw the tunneling of the superconductivity, could this happen for the discommensurations in the CDW?

The charge density and superconductivity in transition-metal dichalcogenides are an interesting branch of condensed physics for future studies and we provide a robust theoretical and numerical framework to explore this rich environment.

APPENDIX A – ABRIKOSOV VORTEX STATE

A.1 Abrikosov Lattice

The greatest strength of the GL theory over the other existing theories of SC at that time was its capability to solve multiple problems without having to look at the microscopic aspects of the superconductor. Another advantage is that it is considerably easier to work with the GL theory when the order parameter has a spatial dependency. The theory allowed A. A. Abrikosov[9] to study type-II superconductors in a magnetic field. He predicted that just below H_{c2} the order parameter forms a periodic vortex lattice, where each vortex carries a quantum of magnetic flux. His work explains why type-II superconductors let the magnetic field enter without losing superconductivity and why $\kappa = 1/\sqrt{2}$ is the division between type-I and type-II. Abrikosov won the Nobel Prize in physics in 2003 for his important contributions to the understanding of vortices in superconductors.

A.1.1 Fluxoid quantization

Let's apply the GL theory in a superconductor ring with a perpendicular magnetic field, as illustrated in Fig. 34. Using cylindrical coordinates the OP $\psi(r,\phi,z)$ must be periodic

Figure 34 – Magnetic field in a superconducting ring

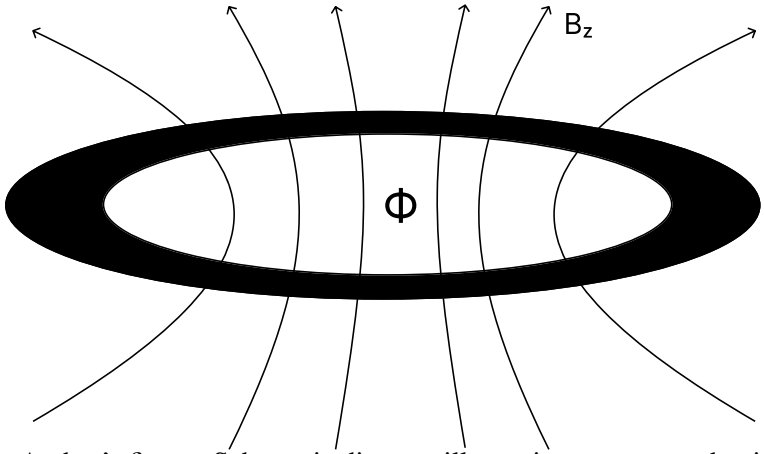

Source: Author's figure. Schematic diagram illustrating a superconducting ring

in ϕ. Assuming the superconductor ring is uniform, the solution does not depend on z or r. The solution takes the form:

$$\psi(\phi) = \psi_0 e^{in\phi} \tag{A.1}$$

where n is an integer. The magnetic flux passing through the wire is given by the integral

$$\Phi = \int \mathbf{B} \cdot d\mathbf{S} = \int \nabla \times \mathbf{A} \cdot d\mathbf{S} = \oint \mathbf{A} \cdot d\mathbf{r} = 2\pi r A_\phi \tag{A.2}$$

where the vector potential can be written as

$$A_\phi = \frac{\Phi}{2\pi r}. \tag{A.3}$$

Applying Eq. (A.1) and (A.3) in the integral form of the free energy equation (2.12)

$$F_s(T) = F_n(T) + \int d^3r \left(\frac{1}{2m^*} \left| \left(\frac{\hbar}{i}\nabla - \frac{e^*}{c}\mathrm{A} \right) \psi \right|^2 + a_s|\psi|^2 + \frac{b_s}{2}|\psi|^4 \right) + E_B \tag{A.4}$$

or

$$F_s(T) = F_s^0 + V\frac{\hbar^2}{2m^*R^2}\left(n - \frac{\Phi}{\Phi_0}\right)^2 |\psi|^2 + E_B \tag{A.5}$$

where

$$F_s^0 = F_n(T) + \int d^3r\, a_s|\psi|^2 + \frac{b_s}{2}|\psi|^4 \tag{A.6}$$

is the ring's free energy in the absence of magnetic flux and

$$E_B = \frac{1}{2\mu_0}\int B^2 d^3r \tag{A.7}$$

is the magnetic field energy in the vacuum.

In the second term in Eq. (A.5), $\Phi_0 = hc/e^*$ is the fluxoid quantum. If we want to minimize the ring's energy, the flux Φ must be an integer multiple of the fluxoid quantum

$$\Phi = n\Phi_0 \tag{A.8}$$

It is interesting to note that we can have several values of n that minimize the free energy. When the ring is cooled below the critical temperature T_c, the system will enter one of the meta-states, depending on the field that has been applied. The magnetic field induces a current in the superconducting ring. If the magnetic field is removed, the ring will still be in one of the energy minima illustrated in Fig. 35 and the induced current will persist.

Abrikosov used these results and showed that, in type-II superconductors, the magnetic flux that penetrates the superconductor is quantized to minimize the free energy. The clearest peculiarity of type-II superconductors is the magnetic field increase inside the superconductor without destroying superconductivity, thus constituting a second-order phase transition. The magnetic flux continuously increases from a critical field H_{c1} to a second critical

Figure 35 – Energy minima as a function of the quantum flux

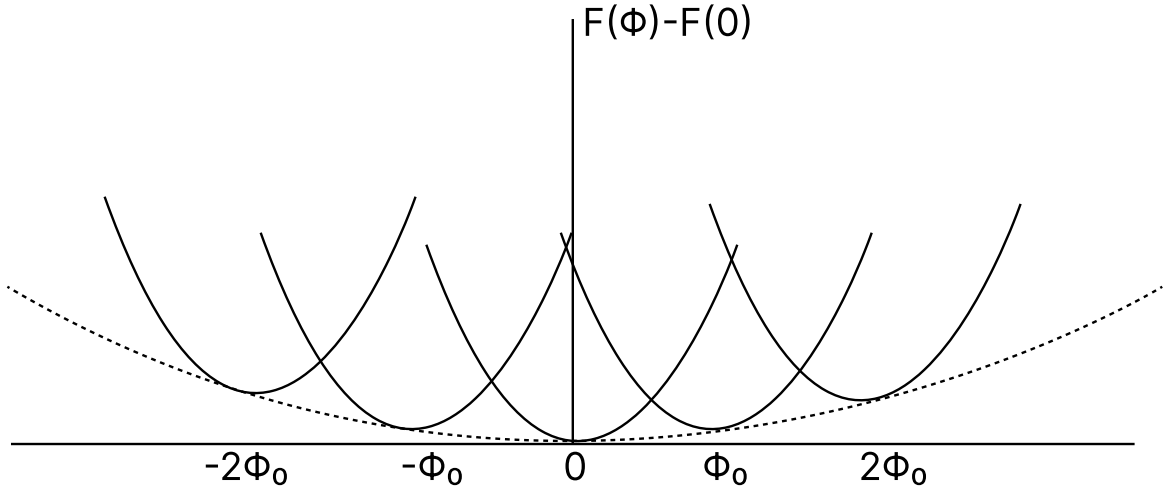

Source: Figure adapted from [44]. Energy minimum as a function of the quantum flux. When the superconductor is cooled in a magnetic field, the OP enters at one of the minima of energy depending on the field applied.

field H_{c2}, where the superconductivity is destroyed. A. A. Abrikosov developed a theory that explains this behavior, demonstrating the existence of the two types of superconductors and the existence of a periodic lattice of magnetic vortices.

The order parameter ψ is small at the vicinity of H_{c2}. With this premise, we can use the linear form of the first GL equation, by removing the non-linear term,

$$\frac{\hbar^2}{2m^*}\left[-i\nabla - \frac{e^*}{\hbar c}\mathbf{A}\right]^2 \psi + a_s\psi = 0. \tag{A.9}$$

Assuming a magnetic field at the z-component

$$\mathbf{B} = (0,0,B) \tag{A.10}$$

and using Landau gauge to write the potential vector **A**,

$$\mathbf{A} = (0,xB,0). \tag{A.11}$$

Replacing the potential vector in Eq. (A.9), we have

$$\frac{\hbar^2}{2m^*}\left(-i\nabla - \frac{e^*B}{\hbar c}x\hat{y}\right)\cdot\left(-i\nabla - \frac{e^*B}{\hbar c}x\hat{y}\right)\psi + a_s\psi = 0 \tag{A.12}$$

$$\left(-\frac{\hbar^2}{2m^*}\nabla^2 + \frac{i\hbar e^*B}{m^*c}x\frac{\partial}{\partial y} + \frac{(e^*B)^2}{2m^*c^2}x^2\right)\psi + a_s\psi = 0 \tag{A.13}$$

Introducing the term $\omega_c = \frac{e^*B}{cm^*}$ and considering that a_s is negative in the superconducting regime,

we can rewrite (A.13) as an eigenvalue equation

$$\left(-\frac{\hbar}{2m^*}\nabla^2+\hbar\omega_c ix\frac{\partial}{\partial x}+\frac{m^*\omega_c^2}{2}x^2\right)\psi=|a_s|\psi. \tag{A.14}$$

The equation takes the form of a Schrödinger equation for a charged particle in a magnetic field [47]. The ansatz for this type is

$$\psi(\mathbf{r})=\mathrm{e}^{i(k_y y+k_z z)}f(x), \tag{A.15}$$

where it is necessary to find the unknown function $f(x)$. Let us emply this ansatz in Equation A.14

$$-\frac{\hbar^2}{2m^*}\frac{\mathrm{d}^2 f}{dx^2}+\left(\hbar\omega_c k_y x+\frac{m^*\omega_c^2}{2}x^2\right)f=\left(|a_s|-\frac{\hbar^2(k_y^2+k_z^2)}{2m^*}\right)f. \tag{A.16}$$

We can complete the term on the left side

$$\left(\hbar\omega_c k_y x+\frac{m^*\omega_c^2}{2}x^2\right)=\frac{m^*\omega_c^2}{2}x^2(x-x_0)^2-\frac{m^*\omega_c^2}{2}x_0^2 \tag{A.17}$$

where $x_0=\hbar k_y/m^*\omega_c$, and rearranging the terms

$$-\frac{\hbar^2}{2m^*}\frac{\mathrm{d}^2 f}{\mathrm{d}x^2}+\frac{m^*\omega_c^2}{2}(x-x_0)^2 f=\left(|a_s|-\frac{\hbar^2 k_z^2}{2m^*}\right)f \tag{A.18}$$

Equation (A.18) is the Schrödinger equation for a harmonic oscillator displaced from the origin of x_0[47], where f plays the role of an eigenstate

$$Hf=Ef. \tag{A.19}$$

The right term in the parentheses is the energy of the oscillator

$$\left(n+\frac{1}{2}\right)\hbar\omega_c+\frac{\hbar^2 k_z^2}{2m^*}, \tag{A.20}$$

so that, isolating $|a_s|$,

$$|a_s(T)|=\left(n+\frac{1}{2}\right)\hbar\omega_c+\frac{\hbar^2 k_z^2}{2m^*}. \tag{A.21}$$

When a superconductor in the presence of an external magnetic field B is cooled down, at the critical temperature $T_c(H=0)$, the critical temperature at a zero magnetic field, it is impossible to solve Eq. (A.21), since $|a_s(T)|=0$, but the minimum energy of an oscillator (right side) is the ground state, with $n=0$, $k_z=0$ and $E=\hbar\omega_c/2$. Therefore, the temperature for which the

transition occurs depends on the external magnetic field

$$\frac{\hbar\omega_c}{2} = a_0(T_c - T), \tag{A.22}$$

$$T(H) = T_c(0) - \frac{\hbar\omega_c}{2}. \tag{A.23}$$

The temperature needed for the phase transition is therefore lower as the magnetic field increases.

Another possible situation is to keep the superconductor at a fixed temperature below T_c and decrease the magnetic field B. When the magnetic field crosses the H_{c2}, the superconductivity appears in the ground state. Using Eq. (A.22)

$$\frac{\hbar e^* B}{m^* c} = a_0(T_c - T) \tag{A.24}$$

$$B_{c2} = \frac{2m^* a_0(T_c - T)}{\hbar^2}\frac{h}{2\pi} \tag{A.25}$$

$$H_{c2} = \frac{\Phi_0}{2\pi\mu_0\xi(T)^2} \tag{A.26}$$

This expression determines the number of quantum flux per unit of area that can exist simultaneously in the superconductor.

The thermodynamic critical field, equation (2.15), is related to the free energy difference between the superconducting state and the normal state. The second critical field, equation (A.26), is also related to the transition between the normal and the superconducting states. We have an ambiguity, which one is correct? Let's compare the equations

$$H_c = \frac{a_0}{(\mu_0 b_s)^{1/2}}(T_c - T) \tag{A.27}$$

we can rewrite in terms of the characteristic lengths

$$H_c = \frac{\Phi_0}{2\pi\sqrt{2}\xi\lambda} \tag{A.28}$$

using the H_{c2}

$$H_c = \frac{H_{c2}}{\sqrt{2}\kappa} \tag{A.29}$$

or

$$H_{c2} = \sqrt{2}\kappa H_c \tag{A.30}$$

where $\kappa = \lambda/\xi$. We have two possible outcomes depending on the κ. If $\kappa > 1/\sqrt{2}$, $H_{c2} > H_c$ and the superconductor goes through two phase transitions. First, when the magnetic field is

H_c, the superconductor goes from the pure Meissner state, without vortex, to the mixed state, where part of the magnetic field enters the superconductor. The second transition is when the magnetic field is H_{c2} and the superconductor becomes the normal state. Fig. 36 is a schema of the superconductor magnetization versus the applied field for this behavior. These superconductors are classified as type-II. The second outcome is when $\kappa < 1/\sqrt{2}$, then $H_{c2} < H_c$,

Figure 36 – Sketchy of the magnetization for type-II superconductors

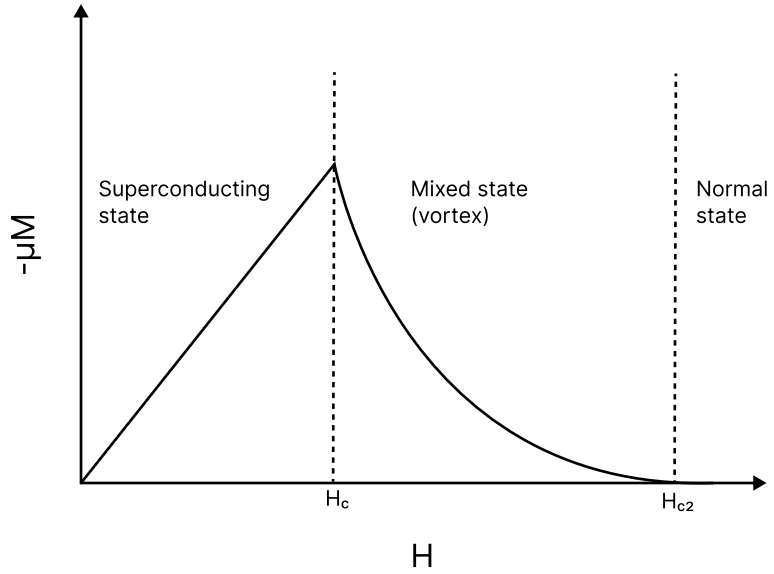

Source: Author's figure. The magnetization versus the magnetic field for type-II superconductors. To expel the magnetic field, the magnetization increases until the first critical H_c, where the vortex starts to penetrate the superconductor. Between H_c and H_{c2}, increases the number of vortexes in the superconductor and the magnetization slowly decreases until H_{c2}, where the superconductivity is destroyed.

and the superconductor goes through one phase transition. When the magnetic field is H_c, the superconductor goes from the superconducting state to the normal state directly. This first-order phase transition is sketched in Fig. 37 and the superconductor is classified as type-I. Pure materials are mostly type-I superconductors, which is one of the reasons they were discovered first. Type-II superconductors allowed for studies with high magnetic fields due to the mixed state and the vortex states and their behavior is one of the most studied topics in superconductivity.

The linearized GL equation allowed us to evaluate H_{c2} and classify the superconductors, but we still do not have information about the distribution of the OP. We need to return to the non-linear GL equation and try to solve it. Abrikosov used an insightful ansatz that led to the solution. He realized that in the linearized equation, only the ground state of the oscillator, $n = 0$ and $k_z = 0$, is important, but there are infinite degenerate states that correspond to the

Figure 37 – Sketchy of the magnetization for type-I superconductors

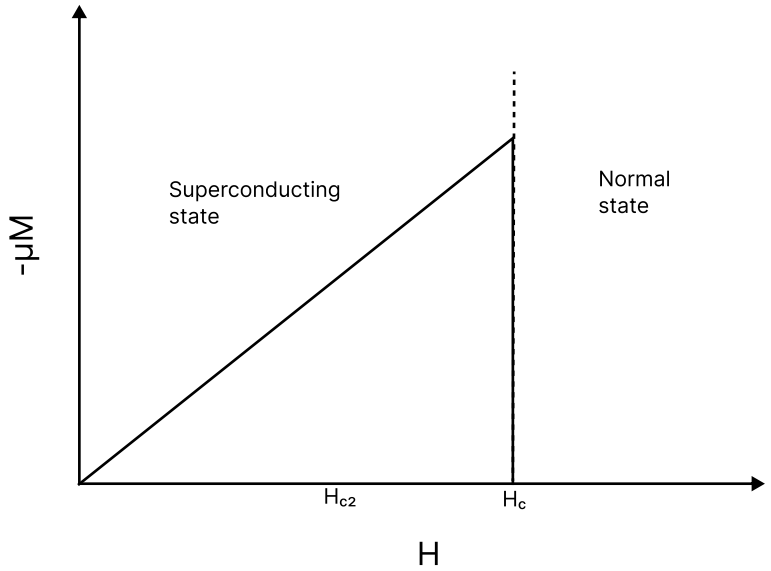

Author's figure. The magnetization versus the magnetic field for type-I superconductors. To expel the magnetic field, the magnetization increases until the first critical H_c. After H_c, the superconductivity is destroyed.

different values of k_y. The solution to the ground stat is a Gaussian function[47]

$$\psi(\mathbf{r}) = Ce^{ik_y y} e^{-(x-x_0)^2/\xi(T)^2} \tag{A.31}$$

Abrikosov assumed that the final solution should be periodic in y and restricted the values of k_y

$$k_y = \frac{2\pi}{l_y} n, \tag{A.32}$$

where n is integer, positive or negative, and l_y is the period. The term x_0 in the oscillator solution takes the value of

$$x_0 = -\frac{2\pi\hbar}{m\omega_c l_y} = -\frac{\Phi_0}{B l_y} n \tag{A.33}$$

The periodic solution has the form

$$\psi(\mathbf{r}) = \sum_{n=-\infty}^{\infty} C_n e^{i(2\pi n y/l_y)} e^{-(x+n\Phi_0/Bl_y)^2/\xi(T)^2}. \tag{A.34}$$

The parameter C_n is a variational parameter that is chosen to minimize the free energy of the system.

The solution is periodic in y, but not in x. Abrikosov forced the solution to also be periodic in x, thus the coefficients C_n are periodic for a parameter ν

$$C_{n+\nu} = C_n \tag{A.35}$$

and the period l_x is

$$l_x = \nu \frac{\Phi_0}{B l_y}. \tag{A.36}$$

Now, the solution is periodic in y and x. We need yet to choose the value of ν to minimize the free energy.

In his study, Abrikosov used $\nu = 1$ which creates a square lattice. Further studies have shown that the triangular lattice, with $\nu = 2$, has a free energy slightly smaller than the square lattice. Whatever the configuration, the main point of Abrikosov's work is that the OP $\psi(\mathbf{r})$ goes to zero at one point for each unit cell, and a quantum flux Φ_0 enters the superconductor, creating a mixed (vortex) state. The final solution is a periodic vortex lattice, as shown in Fig. 38.

Figure 38 – Abrikosov vortex lattice

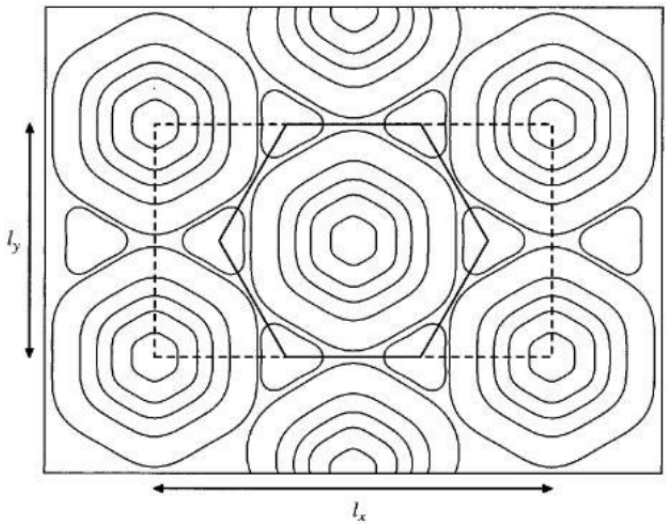

Source: Figure extracted from [45]. Vortex lattice in a type-II superconductor. Each vortex carries one quantum flux Φ.

REFERENCES

[1] LONDON, F.; LONDON, H. The electromagnetic equations of the supraconductor. *Proceedings of the Royal Society of London A: Mathematical, Physical and Engineering Sciences*, v. 149, p. 71–88, 3.

[2] BORN M., C. K. Theory of superconductivity. *Nature*, p. 968–969, 1948.

[3] FRENKEL, J. On a possible explanation of superconductivity. *Physical Review*, American Physical Society, v. 43, p. 907–912, jun. 1933.

[4] TISZA, L. Theory of superconductivity. *Physical Review*, American Physical Society, v. 80, p. 717–726, nov. 1950.

[5] GINZBURG, V. L. On the theory of superconductivity. *Il Nuovo Cimento (1955-1965)*, v. 2, p. 1234–1250. ISSN 1827-6121.

[6] LANDAU, L. The theory of phase transitions. *Nature*, p. 840–841, 1936.

[7] DELFT, D. V.; KES, P. The discovery of superconductivity. *Physics today*, v. 63, n. 9, p. 38–43, 2010.

[8] MEISSNER, W.; OCHSENFELD, R. Ein neuer effekt bei eintritt der supraleitfähigkeit. *Naturwissenschaften*, Springer-Verlag Berlin/Heidelberg, v. 21, p. 787–788, 1933. ISSN 0028-1042.

[9] ABRIKOSOV, A. The magnetic properties of superconducting alloys. *Journal of Physics and Chemistry of Solids*, v. 2, p. 199–208, 1. ISSN 00223697.

[10] BARDEEN, J.; COOPER, L.; SCHRIEFFER, J. Theory of superconductivity. *Physical Review*, v. 108, p. 1175. ISSN 0031-899X.

[11] GOR'KOV, L. P. Microscopic derivation of the ginzburg-landau equations in the theory of superconductivity. *Soviet Physics Journal of Experimental and Theoretical Physics*, v. 36, p. 1364–1367. ISSN 0038-5646.

[12] BEDNORZ, J.; MULLER, K. Possible high tc superconductivity in the BaLaCuO system. *Zeitschrift für Physik B*, v. 64, p. 189–193, 1986. ISSN 0722-3277.

[13] THE Ginzburg–Landau theory in application. *Physica C: Superconductivity*, v. 470, n. 19, p. 791–795, 2010. ISSN 0921-4534. Vortex Matter in Nanostructured Superconductors.

[14] BERDIYOROV G. R., M. M. V.; PEETERS, F. M. Vortex configurations and critical parameters in superconducting thin films containing antidot arrays: nonlinear ginzburg-landau theory. *Physical Review B*, American Physical Society, v. 74, p. 174512, nov. 2006.

[15] GEURTS, R.; MILOSEVIC, M. V.; PEETERS, F. M. Vortex matter in mesoscopic two-gap superconducting disks: influence of josephson and magnetic coupling. *Physical Review B*, American Physical Society, v. 81, p. 214514, jun. 2010.

[16] KOMENDOVÁ, L. *et al.* Different length scales for order parameters in two-gap superconductors: Extended ginzburg-landau theory. *Physical Review B*, American Physical Society, v. 84, p. 064522, aug 2011.

[17] KOMENDOVÁ, L. *et al.* Two-band superconductors: hidden criticality deep in the superconducting state. *Physical Review Letters*, American Physical Society, v. 108, p. 207002, may. 2012.

[18] DANTAS, D. S. *et al.* Bound vortex states and exotic lattices in multicomponent bose-einstein condensates: The role of vortex-vortex interaction. *Physical Review A*, 2015. ISSN 10941622.

[19] CHAVES, A. *et al.* Conditions for nonmonotonic vortex interaction in two-band superconductors. *Physical Review B*, v. 83, n. 21, p. 214523, jun. 2011. ISSN 10980121.

[20] HIKAMI, S.; FUJITA, A. Nonlocal Ginzburg-Landau Model for High-Temperature Superconductors in a Magnetic Field. *Progress of Theoretical Physics*, v. 83, n. 3, p. 443–454, 03 1990. ISSN 0033-068X.

[21] TEWORDT, L.; WERMBTER, S.; WÖLKHAUSEN, T. Ginzburg-landau-gorkov theory for high-temperature superconductors. *Physical Review B*, American Physical Society, v. 40, p. 6878–6883, oct. 1989.

[22] MCMILLAN, W. Landau theory of cdw in transition-metal dichalcogenides. *Physical Review B*, v. 12, p. 1187, 1975.

[23] MCMILLAN, W. L. Theory of discommensurations and the commensurate-incommensurate charge-density-wave phase transition. *Physical Review B*, v. 14, p. 1496–1502, 1976. ISSN 01631829.

[24] MCMILLAN, W. L. Collective modes of a charge-density wave near the lock-in transition. *Physical Review B*, American Physical Society, v. 16, p. 4655–4658, 11. ISSN 01631829.

[25] GRüNER, G.; GOR'KOV, L. P. *Charge density waves in solids*. [S.l.]: Elsevier, 2012. ISBN 0444600736.

[26] TURGUT, S.; FALICOV, L. M. Phenomenological ginzburg-landau theory of charge-density-wave spectra. *Physical Review B*, American Physical Society, v. 50, p. 8221–8229, sep. 1994.

[27] GEIM, A. K.; GRIGORIEVA, I. V. Van der waals heterostructures. *Nature*, Nature Publishing Group UK London, v. 499, n. 7459, p. 419–425, 2013.

[28] BHIMANAPATI, G. R. *et al.* Recent advances in two-dimensional materials beyond graphene. *ACS nano*, ACS Publications, v. 9, n. 12, p. 11509–11539, 2015.

[29] GOLI, P. *et al.* Charge density waves in exfoliated films of van der waals materials: evolution of raman spectrum in tise2. *Nano letters*, ACS Publications, v. 12, n. 11, p. 5941–5945, 2012.

[30] XI, X. *et al.* Strongly enhanced charge-density-wave order in monolayer nbse2. *Nature nanotechnology*, Nature Publishing Group UK London, v. 10, n. 9, p. 765–769, 2015.

[31] REN, Y.; QIAO, Z.; NIU, Q. Topological phases in two-dimensional materials: a review. *Reports on Progress in Physics*, IOP Publishing, v. 79, n. 6, p. 066501, 2016.

[32] XU, M. *et al.* Graphene-like two-dimensional materials. *Chemical reviews*, ACS Publications, v. 113, n. 5, p. 3766–3798, 2013.

[33] MIRÓ, P.; AUDIFFRED, M.; HEINE, T. An atlas of two-dimensional materials. *Chemical Society Reviews*, Royal Society of Chemistry, v. 43, n. 18, p. 6537–6554, 2014.

[34] SCHWIERZ, F.; PEZOLDT, J.; GRANZNER, R. Two-dimensional materials and their prospects in transistor electronics. *Nanoscale*, Royal Society of Chemistry, v. 7, n. 18, p. 8261–8283, 2015.

[35] VELICKỲ, M.; TOTH, P. S. From two-dimensional materials to their heterostructures: An electrochemist's perspective. *Applied Materials Today*, Elsevier, v. 8, p. 68–103, 2017.

[36] KHAN, K. *et al.* Recent developments in emerging two-dimensional materials and their applications. *Journal of Materials Chemistry C*, Royal Society of Chemistry, v. 8, n. 2, p. 387–440, 2020.

[37] HU, N. C.; MACDONALD, A. H. Competing magnetic states in transition metal dichalcogenide moiré materials. *Physical Review B*, APS, v. 104, n. 21, p. 214403, 2021.

[38] WANG, Z. *et al.* Intercalated phases of transition metal dichalcogenides. *SmartMat*, Wiley Online Library, v. 1, n. 1, p. e1013, 2020.

[39] AGHAJANIAN, M.; MOSTOFI, A. A.; LISCHNER, J. Tuning electronic properties of transition-metal dichalcogenides via defect charge. *Scientific Reports*, Nature Publishing Group UK London, v. 8, n. 1, p. 13611, 2018.

[40] JARIWALA, D. *et al.* Emerging device applications for semiconducting two-dimensional transition metal dichalcogenides. *ACS nano*, ACS Publications, v. 8, n. 2, p. 1102–1120, 2014.

[41] KOLEY, S.; MOHANTA, N.; TARAPHDER, A. Charge density wave and superconductivity in transition metal dichalcogenides. *The European Physical Journal B*, Springer, v. 93, p. 1–8, 2020.

[42] GAN, L.-Y. *et al.* Order-disorder phase transitions in the two-dimensional semiconducting transition metal dichalcogenide alloys $Mo_{1-x}W_xX_2$ (x= s, se and te). *Scientific reports*, Nature Publishing Group UK London, v. 4, n. 1, p. 6691, 2014.

[43] PáSZTOR Árpád *et al.* Holographic imaging of the complex charge density wave order parameter. *Physical Review Research*, American Physical Society, v. 1, p. 33114, 11.

[44] TINKHAM, M. *Introduction to Superconductivity*. Second. [S.l.]: Dover, 2004. 480 p. ISBN 0486435032.

[45] ANNETT, J. F. *Superconductivity, Superfluids and Condensates*. [S.l.: s.n.], 2004. 186 p.

[46] LANDAU, L. D.; LIFSHITZ, E. M. *Quantum mechanics*: non-relativistic theory. 1. ed. [S.l.]: Addison Wesley, 1958. 515 p.

[47] SAKURAI, J. J. *Mecânica quântica moderna*. 2. ed. [S.l.]: Bookman, 2013. 548 p. ISBN 978-85-65837-09-5.

[48] FRöHLICH, H. On the theory of superconductivity: the one-dimensional case. *Proceedings of the Royal Society of London. Series A. Mathematical and Physical Sciences*, The Royal Society London, v. 223, p. 296–305, 1954. ISSN 0080-4630.

[49] PEIERLS, R.; PEIERLS, R. E. *Quantum theory of solids*. [S.l.]: Oxford University Press, 1955. ISBN 019850781X.

[50] TRANQUADA, J. M. *et al.* Cooperative ordering of holes and spins in $La_2NiO_{4.125}$. *Physical Review B*, American Physical Society, v. 52, p. 3581–3595, 8.

[51] TRANQUADA, J. M.; ICHIKAWA, N.; UCHIDA, S. Glassy nature of stripe ordering in $La_{1.6-x}Nd_{0.4}Sr_xCuO_4$. *Physical Review B*, American Physical Society, v. 59, p. 14712–14722, 6.

[52] TRANQUADA, J. M. *et al.* Evidence for stripe correlations of spins and holes in copper oxide superconductors. *Nature*, v. 375, p. 561–563. ISSN 1476-4687.

[53] CHEONG, S.-W. *et al.* Incommensurate magnetic fluctuations in $La_{2-x}Sr_xCuO_4$. *Physical Review Letters*, American Physical Society, v. 67, p. 1791–1794, 9.

[54] ECKERN, U.; GEIER, A. Microscopic theory of charge-density wave systems. *Zeitschrift für Physik B Condensed Matter*, v. 65, p. 15–27. ISSN 1431-584X.

[55] ROSSNAGEL, K. On the origin of charge-density waves in select layered transition-metal dichalcogenides. *Journal of Physics: Condensed Matter*, v. 23, p. 213001, 6. ISSN 0953-8984.

[56] ATTANASI, A. Competition between superconductivity and charge density waves: the role of disorder. 6.

[57] CHEN, C. *et al.* Discommensuration-driven superconductivity in the charge density wave phases of transition-metal dichalcogenides. *Physical Review B*, v. 99, 2019. ISSN 24699969.

[58] JANG, H. *et al.* Ideal charge-density-wave order in the high-field state of superconducting ybco. *Proceedings of the National Academy of Sciences*, Proceedings of the National Academy of Sciences, v. 113, p. 14645–14650, 12. Doi: 10.1073/pnas.1612849113.

[59] CHUBOV, P. N.; EREMENKO, V. V.; PILIPENKO, Y. A. Dependence of the critical temperature and energy gap on the thickness of superconducting aluminum films. *Soviet Physics JETP*, Vol. 28, p. p.389, 3 1969.

[60] KOGAN, V. G.; NAKAGAWA, N. Critical-temperature enhancement in thin superconducting films due to field dependence of the coherence length. *Physical Review B*, American Physical Society, v. 35, p. 1700–1707, 2.

[61] TALANTSEV, E. F. *et al.* On the origin of critical temperature enhancement in atomically thin superconductors. *2D Materials*, v. 4, p. 025072, 6. ISSN 2053-1583.

[62] YANG, Y. *et al.* Enhanced superconductivity upon weakening of charge density wave transport in $2H-TaS_2$ in the two-dimensional limit. *Physical Review B*, American Physical Society, v. 98, p. 35203, 7.

[63] YANG, X. *et al.* Pressure induced superconductivity bordering a charge-density-wave state in nbte4 with strong spin-orbit coupling. *Scientific Reports*, v. 8, p. 6298. ISSN 2045-2322.

[64] MONTEVECCHI, E.; INDEKEU, J. O. Increasing the critical temperature of a superconductor by curving its surface. *Europhysics Letters (EPL)*, v. 51, p. 661–666, 9. ISSN 0295-5075.

[65] MITO, M. *et al.* Large enhancement of superconducting transition temperature in single-element superconducting rhenium by shear strain. *Scientific Reports*, v. 6, p. 36337. ISSN 2045-2322.

[66] KRISHNAN, M. *et al.* Pressure assisted enhancement in superconducting properties of fe substituted $NbSe_2$ single crystal. *Scientific reports*, Nature Publishing Group UK, v. 8, p. 1251, 1. ISSN 2045-2322.

[67] KVASHNIN, Y. *et al.* Coexistence of superconductivity and charge density waves in tantalum disulfide: Experiment and theory. *Physical Review Letters*, American Physical Society, v. 125, p. 186401, 10.

[68] GABOVICH, A. M. *et al.* Competition of superconductivity and charge density waves in cuprates: Recent evidence and interpretation. *Advances in Condensed Matter Physics*, v. 2010, p. 1–40, 2010.

[69] DAI, P. Antiferromagnetic order and spin dynamics in iron-based superconductors. *Reviews of Modern Physics*, APS, v. 87, p. 855, 2015.

[70] CHO, K. *et al.* Using controlled disorder to probe the interplay between charge order and superconductivity in nbse2. *Nature Communications*, v. 9, p. 2796. ISSN 2041-1723.

[71] CAI, P. *et al.* Visualizing the microscopic coexistence of spin density wave and superconductivity in underdoped nafe1xcoxas. *Nature Communications*, v. 4, p. 1596. ISSN 2041-1723.

[72] MOOR, A.; VOLKOV, A. F.; EFETOV, K. B. Hidden order as a source of interface superconductivity. *Physical Review B*, American Physical Society, v. 91, p. 64511, 2.

[73] MOOR, A. *et al.* Dynamics of order parameters near stationary states in superconductors with a charge-density wave. *Physical Review B*, American Physical Society, v. 90, p. 24511, 7.

[74] NOSCHESE, S.; PASQUINI, L.; REICHEL, L. Tridiagonal toeplitz matrices: properties and novel applications. *Numerical Linear Algebra with Applications*, v. 20, p. 302–326, 3. ISSN 10705325.

[75] VORONTSOV, A. B.; VAVILOV, M. G.; CHUBUKOV, A. V. Superconductivity and spin-density waves in multiband metals. *Physical Review B*, v. 81, p. 1–21, 2010. ISSN 10980121.

[76] FERNANDES, R. M.; SCHMALIAN, J. Competing order and nature of the pairing state in the iron pnictides. *Physical Review B*, American Physical Society, v. 82, p. 14521, 7.

[77] FERNANDES, R. M. *et al.* Preemptive nematic order, pseudogap, and orbital order in the iron pnictides. *Physical Review B*, American Physical Society, v. 85, p. 24534, 1.

[78] LIAN, C.-S. *et al.* Coexistence of superconductivity with enhanced charge density wave order in the two-dimensional limit of $TaSe_2$. *The Journal of Physical Chemistry Letters*, American Chemical Society, v. 10, p. 4076–4081, 7. Doi: 10.1021/acs.jpclett.9b01480.

[79] LIAN, C.-S.; SI, C.; DUAN, W. Unveiling charge-density wave, superconductivity, and their competitive nature in two-dimensional $NbSe_2$. *Nano Letters*, American Chemical Society, v. 18, p. 2924–2929, 5. ISSN 1530-6984. Doi: 10.1021/acs.nanolett.8b00237.

[80] HARRIS, D. T. *et al.* Charge density wave modulation in superconducting $BaPbO_3/BaBiO_3$ superlattices. *Physical Review B*, American Physical Society, v. 101, p. 64509, 2.

[81] CHIKINA, A. *et al.* Turning charge-density waves into cooper pairs. *npj Quantum Materials*, v. 5, p. 22. ISSN 2397-4648.

[82] DENHOLME, S. J. *et al.* Coexistence of superconductivity and charge-density wave in the quasi-one-dimensional material hfte3. *Scientific Reports*, v. 7, p. 45217. ISSN 2045-2322.

[83] MIAO, H. *et al.* Charge density waves in cuprate superconductors beyond the critical doping. *npj Quantum Materials*, v. 6, p. 31. ISSN 2397-4648.

[84] FERNANDES, R. M.; CHUBUKOV, A. V.; SCHMALIAN, J. Nematic order in iron superconductors - who is in the driver's seat? *Nature Physics*, v. 10. ISSN 1745-2473.

[85] GUPTA, R. *et al.* Coexistence of superconductivity and a charge density wave in $LaPt_2(Si_{1x}Ge_x)_2$ $(0 \leq x \leq 0.5)$. *Journal of Physics: Condensed Matter*, v. 28, p. 195702, 5. ISSN 0953-8984.

[86] GUPTA, R. *et al.* Superconducting and charge density wave transition in single crystalline $LaPt_2Si_2$. *Journal of Physics: Condensed Matter*, v. 29, p. 255601, 6. ISSN 0953-8984.

[87] MOURA, V. N. *et al.* Latent superconductivity at parallel interfaces in a superlattice dominated by another collective quantum phase. *Physical Review B*, American Physical Society, v. 106, p. 14516, 7.

[88] CHIOFALO, M. L.; SUCCI, S.; TOSI, M. P. Ground state of trapped interacting bose-einstein condensates by an explicit imaginary-time algorithm. *Physical Review E*, American Physical Society, v. 62, p. 7438–7444, nov. 2000.

[89] SAVAGE, C. M.; RUOSTEKOSKI, J. Dirac monopoles and dipoles in ferromagnetic spinor bose-einstein condensates. *Physical Review A*, American Physical Society, v. 68, p. 043604, oct. 2003.

[90] PALPACELLI, S.; SUCCI, S.; SPIGLER, R. Ground-state computation of bose-einstein condensates by an imaginary-time quantum lattice boltzmann scheme. *Physical Review E*, American Physical Society, v. 76, p. 036712, sep. 2007.

[91] CHAVES, A. *et al.* The split-operator technique for the study of spinorial wavepacket dynamics. *Communications in Computational Physics*, Cambridge University Press, v. 17, p. 850–866. ISSN 1815-2406.

[92] SUZUKI, M. Fractal decomposition of exponential operators with applications to many-body theories and monte carlo simulations. *Physics Letters A*, v. 146, p. 319–323. ISSN 0375-9601.

[93] GOVERNALE, M.; UNGARELLI, C. Gauge-invariant grid discretization of the schrödinger equation. *Physical Review B*, American Physical Society, v. 58, p. 7816–7821, 9.

[94] YAN, S. *et al.* Influence of domain walls in the incommensurate charge density wave state of cu intercalated $1T - TiSe_2$. *Physical Review Letters*, v. 118, p. 1–5, 2017. ISSN 10797114.

[95] YU, F. *et al.* Unusual competition of superconductivity and charge-density-wave state in a compressed topological kagome metal. *Nature communications*, Nature Publishing Group UK London, v. 12, n. 1, p. 3645, 2021.

[96] MOROSAN, E. *et al.* Superconductivity in cuxtise2. *Nature Physics*, v. 2, p. 544–550. ISSN 1745-2481.

[97] JOE, Y. I. *et al.* Emergence of charge density wave domain walls above the superconducting dome in $1T - TiSe_2$. *Nature Physics*, Nature Publishing Group, v. 10, p. 421, 4.

[98] KUSMARTSEVA, A. F. *et al.* Pressure induced superconductivity in pristine 1 t- tise 2. *Physical Review Letters*, APS, v. 103, n. 23, p. 236401, 2009.

[99] KOGAR, A. *et al.* Observation of a charge density wave incommensuration near the superconducting dome in Cu_xTiSe_2. *Physical Review Letters*, American Physical Society, v. 118, p. 27002, 1.